Thesis
Multi-Compartmental MR Measurements of the Prostate

Nima Gilani

September 2016

Thesis submitted for fulfilment of the degree of Doctorate in Philosophy to Norwich Medical School, University of East Anglia

Abstract

Purpose

A large proportion of the diagnosed prostate cancer patients are suffering from low grade or indolent tumours. Transrectal ultrasound guided biopsy which is conventionally used as the means of diagnosis has a weak correlation with cancer grade or aggressiveness because of its random sampling nature, so that many indolent tumours are treated aggressively with serious side effects. Quantitative magnetic resonance imaging has shown relative success in distinguishing aggressive tumours. It is important to assess the feasibility of different MR modalities such as T_2 or diffusion weighted imaging and to optimise them.

Methods

A variety of biophysical analyses were performed to find correlations between diffusion and T_2 weighted magnetic resonance parameters and the changes in complex compartmental structure of the prostate (consisting of ducts, epithelial and stromal cells, and vascularity) with increasing cancer grade. For this aim, Monte Carlo simulations of a semi-restricted compartment (ductal lumen) and two compartmental exchange model (stromal-epithelial or cellular compartment) were used. Additionally, optimisations were performed for T_2 and diffusion weighted imaging protocols.

Results

The biexponential model for diffusion explicitly explained the biophysical changes in prostate cancer. The fast and slow ADC values respectively varied from 2.36 and 0.9 $\mu m^2 ms^{-1}$ in healthy prostate to around 1 and 0.5 $\mu m^2 ms^{-1}$ in the most aggressive tumours. Biexponential T_2 acquisitions were optimised to distinguish indolent tumours. There was a 10-20% reduction in estimation errors compared to equally distanced acquisitions, if the target values of T_{2slow} and T_{2fast} were respectively 360 and 60 ms. The optimisations were extended to non-Gaussian diffusion weighted imaging protocols.

Conclusion

In order to substantially improve the diagnostic accuracy of prostate cancer MR acquisitions, it is recommended to consider the biophysical model and the optimised protocols introduced here. Also, diffusion time and other acquisition details should be considered prior to the imaging.

Table of Contents

Word count: 29,958

Colour pages: 15, 16, 41, 42, 45, 61, 62, 63, 76, 77, 78

List of Tables

Table 6.2 Equally distanced *b*-value acquisition strategy for N(3-5) *b*-value acquisitions, where (bD)max = 3/K is the maximum allowable acquisition point, CoVK, CoVD and CoVS are the coefficients of variation respectively for K, D and S0. SNR=20

List of Figures

and epithelium. Water exchange between both the vascular space and the ductal lumen and the other compartments is assumed to be negligible. Exchange between stroma and epithelium occurs, but the two are not well mixed.

Fig. 4.2 Flow chart of the method used to determine empirical parameters of the diffusion model.

Fig. 4.3 Plot comparing measured values of measured *ADC* ($D_{measured}$) with values predicted by the model (D_{model}). Measurements made at 1.5T and 3T respectively are in blue and red respectively. Triangles and circles represent Category I (measurements represent a single Gleason score) and II (measurements represent an average Gleason score) papers respectively. The solid line is the line of identity.

Fig. 4.4 Bland-Altman plot of $D_{model} - D_{measured}$, vs. mean, ($D_{model} + D_{measured}$)/2. Measurements made at 1.5T and 3T respectively are in blue and red respectively. Triangles and circles represent Category I and papers respectively. The solid, dotted and dashed lines represent the mean difference, and the mean ± 1.96 standard deviations (i.e., the 95% confidence limits) respectively.

Fig. 4.5 Plot of ductal, epithelial, stromal and cellular (stromal and epithelial combined) *ADC* and cellular kurtosis vs. Gleason sum. A score of 0 corresponds to normal peripheral zone tissue.

Fig. 4.6 Plot of signal vs. *b*-value for normal peripheral zone (PZ) and Gleason sums 5 – 9. Note the discontinuity near b = 0 due to the delta function in Eq. (4.13).

Fig. 5.1 Changes in CoV for estimated biexponential parameters when the parameters are varied from the standard values used for the optimisation. Echo times are 0, 40, 210 and 780 which minimize the error in estimating T_{2f}. (Table 5.2). The blue, yellow, green and red lines represent the CoV of S_s, S_f, T_{2s} and T_{2f} respectively. SNR was 100. a) T_{2s} = 360, T_{2f} =60 and f_f = 0.3-0.9. b) T_{2s} =360, T_{2f} = 40-80 and f_f =0.6. c) T_{2s} = 230-700, T_{2f} =60 and f_f = 0.6.

Fig. 5.2 Changes in CoV for estimated biexponential parameters when the parameters are varied from the standard values used for the optimisation. Echo times are 0, 30, 160 and 670 which minimize the error in estimating T_{2s} (Table 5.3). The blue, yellow, green and red lines represent the *CoV* of S_s, S_f, T_{2s} and T_{2f} respectively. SNR was 100. a) T_{2s} =360, T_{2f} =60 and f_f =0.3-0.9. b) T_{2s} =360, T_{2f} =40-80 and f_f =0.6. c) T_{2s} =230-700, T_{2f} =60 and f_f =0.6. (In Figure a the blue and green lines are very close to each other.)

Fig. 5.3 Changes in CoV for estimated biexponential parameters when the parameters are varied from the standard values used for the optimisation. Echo times are 0, 30, 180 and 740 which minimize CoV of $f_f = S_f/(S_f + S_s)$ (Table 5.4). The blue, yellow, green and red lines represent the *CoV* of S_s, S_f, T_{2s} and T_{2f} respectively. SNR was 100. a) T_{2s} =360, T_{2f} =60 and f_f =0.3-0.9. b) T_{2s} =360, T_{2f} =40-80 and f_f =0.6. c) T_{2s} =230-700, T_{2f} =60 and f_f =0.6.

Fig. 5.4 CoV of estimates of T_{2f}, T_{2s}, S_f and S_s using eight equally spaced echoes where T_{Emax} is the maximum echo time. Blue line, yellow line, green line and red line are respectively for CoV of S_s, S_f, T_{2s} and T_{2f}. SNR=100.

Figure 6.1 Changes in the coefficient of variation in estimating D and K (respectively CoV_D and CoV_K) with varying K for target values of head and neck tumours for 3-5 optimized or equally spaced acquisitions. (a) K varies from 1 to1.5 and CoV_D is measured. (b) K varies from 1 to1.5 and CoVK is measured.

Figure 6.2 Changes in the coefficient of variation in estimating D and K (respectively CoV_D and CoV_K) with varying D for target values of head and neck tumours for 3-5 optimized or equally spaced acquisitions. (a) D varies from 0.3 to 0.85 and CoV_D is measured. (b) D varies from 0.3 to 0.85 and CoV_K is measured.

Abbreviations

ADC-Apparent Diffusion Coefficient

CG- Central Gland

CPMG-Carr Purcell Meiboom Gill

CoV- Coefficient of Variation

DCE- Dynamic Contrast Enhanced

DWI- Diffusion Weighted Imaging

EPI- Echo Planar Imaging

GS-Gleason Score

IVIM- Intra-Voxel Incoherent Motion

MR- Magnetic Resonance

MRI- Magnetic Resonance Imaging

MSE- Mean Square Error

NICE- National Institute for Health and Care Excellence

NMR- Nuclear Magnetic Resonance

PCa- Prostate Cancer

PGSE- Pulsed Gradient Spin Echo

PZ- Peripheral Zone

PSA- Prostate Specific Antigen

RARE- Rapid Imaging with Refocused Echoes

SNR- Signal to Noise Ratio

STD- Standard Deviation

T2W- T_2 Weighted Imaging

TE- Echo Time

TR- Repetition Time

TRUSGB- Transrectal ultrasound guided biopsy

TZ- Transitional Zone

Copyright Licenses

This thesis mostly interpolates material from (Gilani et al. 2015), (Gilani, Malcolm, and Johnson 2016b) and (Gilani, Malcolm, and Johnson 2016a) with respective copyright permission licenses (3898710176396), (3915891478574), and (3915900076709) from John Wiley and Sons to reuse the full articles. Also, one of the chapters is a reproduction of (Gilani, Malcolm, and Johnson 2016c) with permissions from Springer.

Also a figure has been used from (Epstein et al. 2005) with permission license (3940681159379).

Acknowledgments

I would like to thank my supervisor, Professor Glyn Johnson, for his guidance and relentless support without which this work would have not been possible. Also, I would like to thank Professors Colin Cooper and Gareth Barker for examining and reviewing this thesis. Additionally, I am grateful for the comments made by Doctors Paul Malcolm and Donnie Cameron and also Professors Andoni Toms and Lee Shepstone regarding this thesis.

Last but not the least I want to thank my father Asghar Gilani, my mother Mahnaz Farashahi, and my sister Negar Gilani, for the emotional and financial support throughout this PhD.

Declaration

I declare that the research contained in this thesis, unless otherwise formally indicated within the text, is the original work of the author. The thesis **has not been previously submitted** to this or any other university for a degree, and does not incorporate any material already submitted for a degree.

Nima Gilani

Chapter 1: Background

1-1: A Brief History of MRI

Felix Bloch (Bloch 1946) and Edward Mills Purcell (Purcell 1946) simultaneously discovered Nuclear Magnetic Resonance (NMR). Shortly afterwards Hahn (Hahn 1950) showed that the random thermal motion of the spins would reduce the amplitude of the observed NMR signal if a magnetic field inhomogeneity is present, which is currently the basis of diffusion MRI. Currently, diffusion weighted imaging is well known to give insights of cell size and shape, geometric packing and permeability levels for tumours or other diseases (Le Bihan and Johansen-Berg 2012; Koh and Collins 2007).

Non-invasive imaging at high spatial resolution is possible using MRI. Currently, there are two main MR methodologies: one is to extract anatomical or structural information such as in T_1, T_2 or proton density weighted imaging and the other one is to measure functional activity such as movement or diffusion of water molecules in diffusion weighted imaging, blood flow measurements in perfusion MRI, changes in concentration of metabolites in magnetic resonance spectroscopy (MRS) or concentration of contrast agents in dynamic contrast enhanced (DCE) imaging. (McRobbie et al. 2007)

1-2: Quantitative MR Methods

For either anatomical or functional MR, instead of directly reporting image related parameters which make up the medical image, a wide range of quantities could be tested to see if they lie within the normal range or not. With the increasing interest in such quantitative analysis, MRI is going through a “paradigm shift” in which acquiring high quality images might not be the diagnostic goal. The goal of these analyses is to find parameters that have changes at smaller scales than the visible MR scales or might not be demonstrable in MR images in general (Tofts 2005), such as changes in permeability of cell walls, blood vessels, residence times of water molecules inside a diffusion compartment, etc.

In general, all the reported MR parameters whether image producible or not, are called quantitative MR parameters and the methods that produce or make use of these parameters are called quantitative MR methods.

1-3: Proton Density, T_1 and T_2 Weighted MRI

Proton density, T_1, and T_2 weighted MRI are the three main MR methods in which a sequence of RF and gradient pulses are designed to produce images whose contrast mainly depends on differences between the proton density, T_1 (longitudinal or spin-lattice) relaxation, and T_2 (transverse or spin-spin) relaxation characteristic of samples, respectively.

When a magnetic field is applied to a sample its nuclei start to precess around the main magnetic field. In the case of T_1 and T_2 weighted imaging, a 90 degree radiofrequency pulse (. perpendicular to the main MR magnetic field) is applied to rotate the axis of the nuclei away from the main field and towards the transverse plane, where they give a detectable signal. The angle through which the nuclei are rotated relative to the main magnetic field is adjusted by varying its timing. After removal of the pulse, the spins tend to realign with the main magnetic field, reducing the measurable signal (T_1 relaxation). Simultaneously, spins start to get out of phase from their coherent precession following the application and removal of the radiofrequency pulse, again reducing the measured signal. This process of dephasing is depended on the T_2^* characteristics of the sample. T_2^* relaxation rate of a sample is dependent on spin-spin characteristics of the tissue in addition to external factors such as magnetic field inhomogeneity. In order to cancel out external effects, 180 degree pulses are applied to create “spin echoes”; in this case the measured transverse relaxation is called T_2 relaxation and is solely dependent on spin-spin characteristics of the sample. (Mitchell 1999)

1-4: Diffusion Weighted MRI

Diffusion MRI has proven useful in characterizing tumours in a number of different cancers (Padhani et al. 2009; Koh and Collins 2007) such as

breast (Theilmann et al. 2004; Sigmund et al. 2011; Iima et al. 2015), prostate (Rosenkrantz et al. 2012), and brain (Hayashida et al. 2006).

Generally, diffusion weighted imaging is a probe of random Brownian motion of water molecules in the tissue using a pair of diffusion sensitizing gradients (Stejskal and Tanner 1965). The diffusion sensitizing gradients are linear variations of the main MR magnetic field in the directions that diffusion is being measured; The application of these gradients results in decreases in the final acquired signal from the spins that have higher diffusion coefficients (Zubkov et al. 2016). During the application of the first gradient pulse, the spins have different precession speeds depending on their distance from the central point with zero gradient. After the gradient is removed, the spins are allowed to diffuse for a certain amount of time. Finally, a gradient in the opposite direction is applied; if the spins have not moved the phase of their precession is the same as having no gradients. Conversely, fast moving spins are dephased from each other and hence their accumulated signal is decreased (Hall and Alexander 2009).

Diffusion weighted imaging could be considered as a derivative of T_1 imaging (stimulated spin-echo (Tanner 1970)) or T_2 imaging (spin-echo (Stejskal and Tanner 1965)) depending on the combination of radiofrequency pulses used during the acquisition.

1-5: Anatomy of the Prostate

The prostate gland is surround by the bladder base from its superior side and urogenital diaphragm from its inferior side. The prostate capsule contains the prostatic urethra and the ejaculatory ducts. There are five zones associated with the prostate. There four zones with the prostate capsule: the peripheral zone (PZ), the transition zone (TZ), the central gland (CG), and the periurethral glandular tissue; additionally, the prostate is covered by non-glandular anterior fibromuscular stroma. Fig. 1.1 is a depiction of these zones. Benign hyperplasia or proliferation of epithelial and smooth muscle cell occurs in the transition zone of the prostate. Whereas, metastatic prostate tumours are mostly located within the peripheral zone. (McNeal 1988; Villeirs et al. 2005).

The glandular structure of the prostate consists of ductal lumen surrounded by secretary epithelial cells. These glandular structures are surrounded by muscle cells that control urine flow and ejaculation plus the fibrous cells that strengthen the structure of the gland (Shier, Butler, and Lewis 2006). The latter two are called (fibro-muscular) stromal cells throughout this thesis. Fig. 1.2 shows the three main compartments of the prostate (i.e. ducts, epithelial cells, and stromal cells).

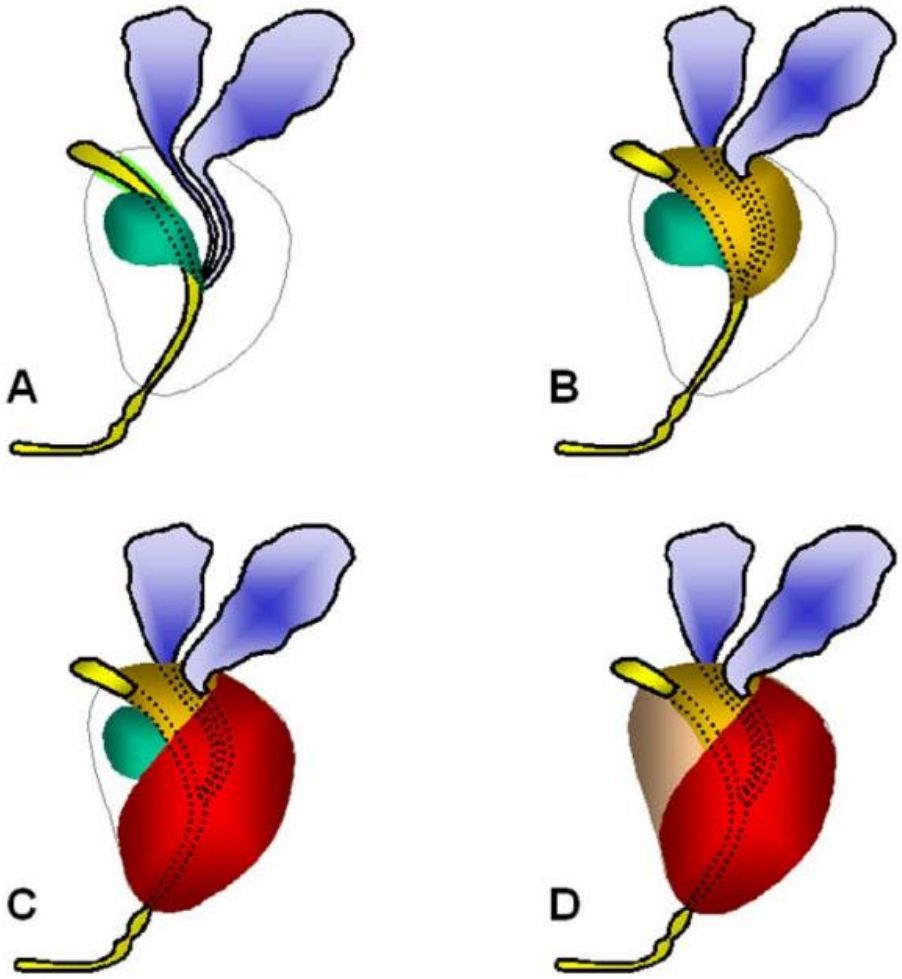

Figure 1.1 Prostate Zones: (A) The urethra (blue), the seminal vesicles and ejaculatory (yellow), the periurethral glands (pale green stripe), and the transition zone (dark green). (B) The central zone (orange) bounding the posterior surface of the transition zone and urethra and enclosing the ejaculatory ducts. (C) The peripheral zone (red); the ratio of peripheral zone to central gland increases downward from base to apex. (D) The prostate is covered by non-glandular fibromuscular stroma (brown) on its anterior side. The figure is copied from (Villeirs et al. 2005) with permission from the journal of Radiotherapy and Oncology.

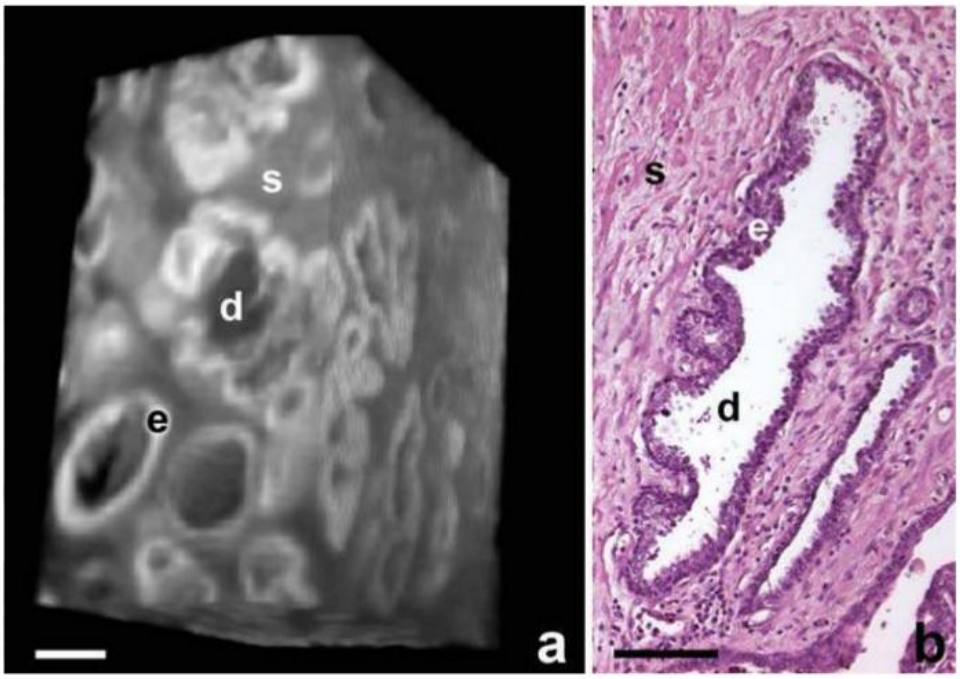

Figure 1.2 (a) MR and (b) histology images of normal prostate tissue containing the ducts (d), epithelial cells (e), and stromal cells (s). The figure is copied from (Bourne et al. 2011), with permission from Magnetic Resonance in Medicine.

1-6: Diagnosis and Grading of Prostate Cancer

Prostate cancer is the fourth most common cancer with 1.1 million diagnosed cases worldwide in 2012 after lung(1.82 million), breast(1.67 million) and colorectal(1.36 million) and is the second most common cancer in men after lung cancer. Prostate cancer accounts for 15% of the cancers diagnosed in men with about 70% of them occurring in more developed countries making it the most common cancer in men in these countries. It is the fifth cause of death from cancer in men worldwide with estimated 307000 deaths representing 6.6% of the total male cancer mortality. (Ferlay et al. 2015)

These statistics indicate high occurrence of prostate cancer, however most prostate tumours are relatively indolent and could be left untreated but monitored regularly (active surveillance).

Prostate specific antigen (PSA) is an enzyme that is secreted from the epithelial cells into the glandular ducts and later seminal flow (Stenman et al. 1999). PSA secretion levels are increased in prostate cancer; as a result

PSA is a sensitive marker for prostate cancer. However, specificity of PSA is low because of high frequency of elevated values in benign prostate hyperplasia (Stenman et al. 1999). Thus, due its high sensitivity, PSA test is necessary but not enough to diagnose prostate cancer. Hence, additional tests are required to verify the cancer.

Conventionally, prostate of patients with elevated PSA levels are assessed using transrectal ultrasound guided biopsy (TRUSGB). Due to its random sampling nature this test might miss cancer, overestimate low grade tumours or underestimate clinically significant tumours (Kim et al. 2015; Singh et al. 2004; Scattoni et al. 2007). Because of this inability to reliably detect intermediate or high risk prostate cancer, urologists tend to act conservatively and choose aggressive treatment (Kim et al. 2015) instead of active surveillance. With this conservative approach, 37 men undergo prostatectomy to avoid one cancer-related death (Schröder et al. 2012). The aggressive treatment is associated with common side effects such as sexual and urinary dysfunction (Pardo et al. 2010).

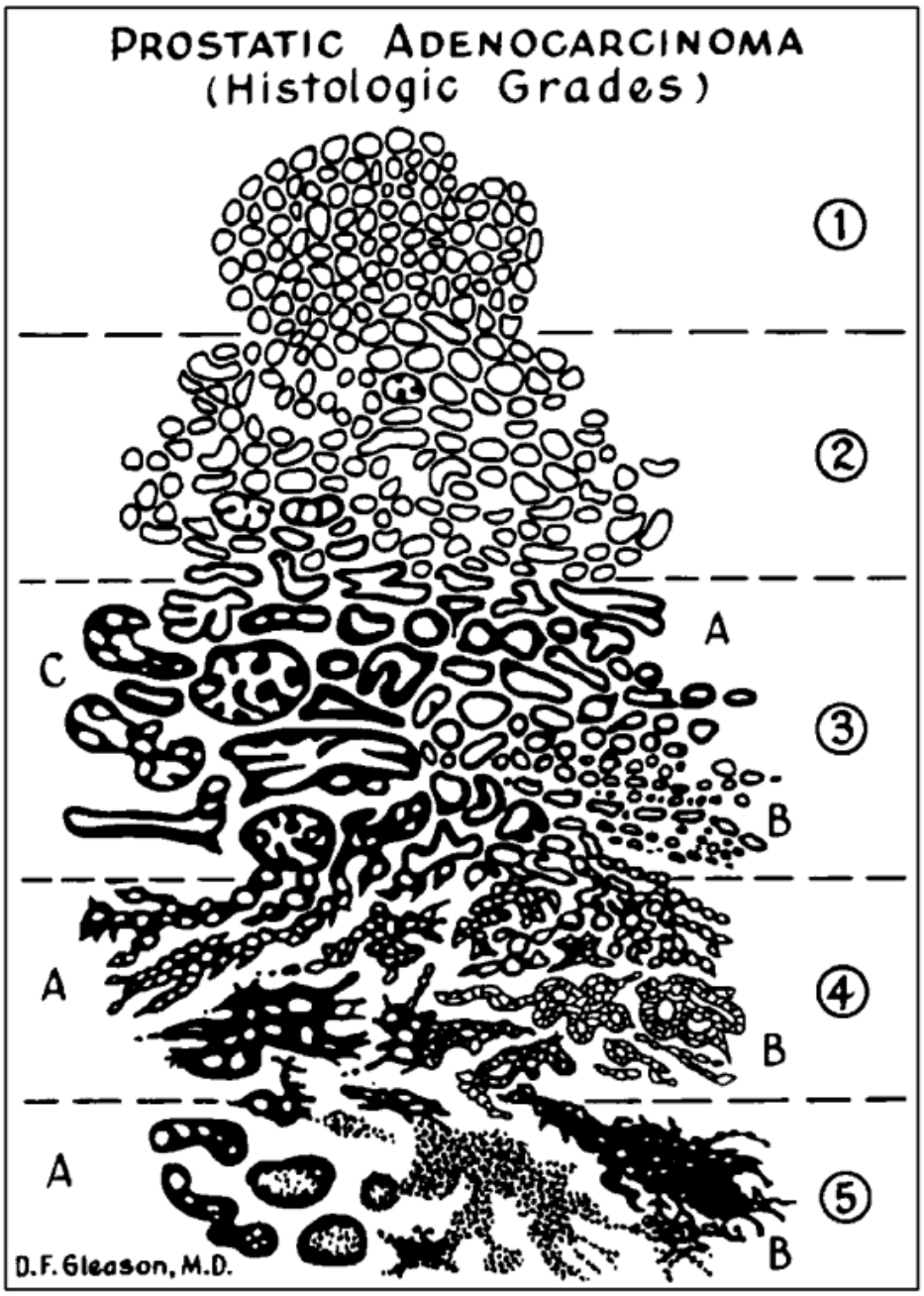

Fig. 1.3 Gleason grading system. Figure reproduced with permission from (Epstein et al. 2005; Gleason 1992).

The current grading system for TRUSGB samples is the Gleason grading system which was originally developed between 1966 and 1974 (Gleason, Mellinger, and Group 2002). Samples are graded based on their aggressiveness pattern from 1 to 5 (known as the Gleason Score) and the sum of the two most common patterns, which ranges between 2 to 10, is referred to throughout the remainder of this thesis as the Gleason Sum. Grades of 3 and below are for poorly differentiated (non-aggressive)

cancer, whereas grades of 4 and 5 are for well differentiated (aggressive) cancer. For example a Gleason score of 3+4 is for higher percentage of poorly differentiated and smaller percentages of well differentiated cancer and a Gleason score of 4+3 is for higher percentage of well differentiated and smaller percentages of poorly differentiated cancer (Epstein, Zelefsky, et al. 2016). This grading system has gone through substantial revisions in 2005 (Epstein et al. 2005) and 2014 (Epstein, Egevad, et al. 2016). There have been a wide range of proposed revisions such as inclusion of new categories and exceptions, and also efforts to make the Gleason grading system more quantitative. However, there are still some deficiencies associated with Gleason scoring system as a marker of prostate cancer aggressiveness. As a result, introducing new prostate cancer (PCa) grading systems is the subject of recent studies (Epstein, Zelefsky, et al. 2016). Specifically, there is a considerably higher rate of biochemical recurrence and mortality associated with Gleason score 4+3 compared to Gleason score 3+4 (Rasiah et al. 2003; Rosenkrantz et al. 2015); hence it has been recommended by (Rosenkrantz et al. 2015; Reese et al. 2012) to report the percentage of the more aggressive component in the Gleason sum.

Additionally, it is important to stage prostate cancer. For this aim, a numbering system consisting of three letters TNM (Tumour, node, and Metastasis) exists to characterise the levels of extension of tumours inside or outside the prostate capsule, lymph node invasion and also metastasis to other organs. Three letter are used to stage prostate cancer. T1, T2, T3 and T4 are respectively for small microscopic tumours that could not be felt during digital exam, tumours within the prostate capsule that could be felt during digital rectal exam, tumours spreading outside the prostate capsule but not beyond, and fixed tumours spreading to nearby structures such as seminal vesicles. N0 means there is no lymph node invasion and N1 means that cancer has invaded nearby lymph node(s). M0 means that cancer has not spread to other organs such as bones or lungs but M1 means that cancer has spread into other organs. (Parker et al. 2015)

Usefulness of quantitative MRI in characterising tumours in a number of different cancers, including prostate cancer has been shown in several

previous studies (Gibbs et al. 2009; Rosenkrantz et al. 2012; Tamada et al. 2008; Vargas et al. 2011; Verma et al. 2011; Yoshimitsu et al. 2008). Hence, it has been recommended by National Institute for Health and Care Excellence (NICE) that patients with elevated PSA levels should have MRI scans prior to having biopsies (Streeter and Brewster 2015) in order to better diagnose prostate cancer.

This characterisation of prostate tissue can be based on proton density and T_1 and T_2 relaxometry, diffusive behaviour of water molecules inside the prostate gland (diffusion weighted imaging), investigating microvascular structure and function by use of pharmacokinetic modelling parameters (dynamic contrast enhanced imaging), or a combination of some or all of these methods (Kozlowski et al. 2006).

Interpretation of prostate MR measurements is complicated by prostate diffusion micro-environment which consists of four distinct compartments: vascular compartment, fibromuscular stromal cells, epithelial cells and ductal lumen (Gorelick et al. 2013; Zynger and Parwani 2014; Doyle et al. 2012). Random flow of blood in the first gives a pseudo-diffusion signal called the intra-voxel incoherent motion (IVIM) effect (Le Bihan et al. 1988; Le Bihan et al. 1986). Diffusion of water molecules inside the other three compartments gives the main diffusion or the so called self-diffusion signal. (Bourne et al. 2011) and (Bourne, Kurniawan, Cowin, Stait-Gardner, Sved, Watson, Chowdhury, et al. 2012) have characterised these compartments *ex vivo* by both histology and diffusion weighted imaging at 16T. For healthy prostate the composition is glandular ducts (diameter~300 μm (Gilani, Malcolm, and Johnson 2016b)), stromal cells and epithelial layers (thickness ~10-20 μm) that separate the first two. Because of the large diameters of the ducts compared with typical diffusion distances (~40μm) (Le Bihan and Johansen-Berg 2012) and the fact that these ducts are filled with fluid instead of having cellular structure, they have long T_2's and considerably higher diffusion coefficients. Additionally, such ductal sizes result in negligible exchange between the ductal lumen and the other two compartments which means that biexponential diffusion MR and biexponential T_2 might yield

important information on tissue state. However, current approaches ignore this compartmentalisation so that estimated parameters represent a weighted average of the properties of the individual compartments. Since some of properties of these compartments such as their volume fraction, average size, cellularity, etc. change for different grades of cancer, separate estimation of the properties of each compartment and correlating them with one or more MR parameter may help in assessing tumour malignancy.

The overall purpose of this PhD project was therefore to develop, optimise and assess methods of measuring the properties of different tissue types in the prostate. The specific aims were to:

1. Better characterize changes in cell size and density, and ductal volume occurring with increasing tumour grade and to correlate them with MR parameters.
2. Use Monte Carlo simulations of random walks of water molecules inside the prostate compartments to explore diffusion in the prostate.
3. Introduce a new model for diffusion weighted imaging of the prostate and compare it with the results from patient studies
4. Perform covariance matrix calculations to measure parameter estimation errors and determine the echo times that provide the greatest precision in measurements of bi-exponential T_2 values in the prostate.

1-7: Monte Carlo Simulation of Diffusion MR

In recent decades, random walk simulations have found applications in many fields of medicine, science and engineering involving transport of particles or waves (Shibata, Tominaga, and Tanaka 2014; Flamm, Diamond, and Sinno 2009; Zhu and Liu 2013; Davis and Dunn 2015; Ansari-Rad, Abdi, and Arzi 2012; Pesch et al. 2015; Dreyer et al. 2014; Tian et al. 2014; Novikov et al. 2011; Jabbari and Monadi 2015; Zhang et al. 2014; Gilani, Malcolm, and Johnson 2016b; Fieremans et al. 2010; Stamatakis and Vlachos 2012; Liu et al. 2015; Mascali and Romano 2014). Some examples are random walks of photons, electrons or other particles

in radiotherapy or brachytherapy to calculate absorbed doses (Jabbari and Monadi 2015; Zhang et al. 2014), restricted random walk (Novikov et al. 2011) of water molecules or gases with applications in diffusion weighted magnetic resonance imaging for either medical purposes (Gilani, Malcolm, and Johnson 2016b; Fieremans et al. 2010) or determining pore structures (Kärger, Ruthven, and Theodorou 2012), catalytic reactions using kinetic Monte Carlo methods (Stamatakis and Vlachos 2012; Liu et al. 2015), transport of electrons or ions in semiconductors (Ansari-Rad, Abdi, and Arzi 2012) and many more.

These applications are quite different from each other in nature such as being relativistic (Zhu and Liu 2013; Davis and Dunn 2015) or non-relativistic (Stamatakis and Vlachos 2012; Novikov et al. 2011) or needing quantum (Bouchard and Bielajew 2015) or classical non-quantum (Stamatakis and Vlachos 2012; Novikov et al. 2011) considerations; as a result each requires different types of differential equation for transport. However, for any type of transport particle or wave such as ions, molecules, charge, photons, spins, etc., the Boltzmann transport equation (Harris 2004) gives a comprehensive understanding of the parameters or interactions affecting the transport. Practically, for diffusion weighted imaging applications, this comprehensive formalism is reduced to simplified equations such as Fick's law for diffusion (Fick 1855) to minimize the number of simulation parameters.

Generally, reductionism in science (Gallagher, Appenzeller, and Normile 1999) is known as the attempt to minimize the number of physical parameters involved to measure, explain, formulate or simulate an entity. In the case of diffusion weighted imaging, the phases of precession of ^{1}H spins (from the complete multi-dimensional phase space of the particles (Penrose and Jorgensen 2006)) are made dependent on their location using a combination of magnetic gradients and electromagnetic pulses. Using this reductionism approach the random diffusive walks of water molecules in different diffusion environments and diffusion times that give the final MR signal are simulated.

If diffusion is not restricted, the probability density function describing diffusion at any arbitrary time is Gaussian. For MR application, usually a Gaussian estimate of diffusion is used (i.e. a Gaussian probability density function is used to describe diffusion); in this case the estimated diffusion coefficients are called apparent diffusion coefficient (ADC). However, this assumption is not always valid; for this case the non-Gaussian behaviour of diffusion is better modelled by additional parameter kurtosis which will be explained in chapter two. (Jensen et al. 2005; Jensen and Helpern 2010)

Additionally, diffusion could be characterized by its dependency on measurement direction. Diffusion is either isotropic (independent of measurement direction) or anisotropic (direction dependent). In the case of isotropic diffusion, measurements could be made in one direction or averaged in more than one direction. Whereas, for anisotropic diffusion, measurements should be performed separately in each direction to characterize the direction dependency of diffusion (diffusion tensor imaging). (Westin et al. 2002)

The trend in the 1990's was to solve diffusion related equations by using deterministic methods and hence to derive a diffusion coefficient for every geometry (Callaghan 1995, 1997; Codd and Callaghan 1999) such as cylinders, planes, spheres and etc. While there was a relative success in giving estimates of diffusion using this methodology, it did not expand further in the twenty first century for two main reasons. First, it is not generally accurate to assume a Gaussian probability function describing random walk of water molecules (Jensen et al. 2005). Second, extension of these solutions to patterns consisting many randomly oriented or shaped geometries requires solving complex and calculation intensive formalisms.

So far, there have been many diffusion-related application of Monte Carlo methods: (Regan and Kuchel 2000, 2003; Fieremans et al. 2010) used Monte Carlo methods to establish relations between permeability levels of membranes and the residence times of the corresponding compartments. Similarly, (Novikov et al. 2011) used Monte Carlo simulations to assess restricted diffusion for different barrier structures. (Xing et al. 2013)

showed how the choice of elastic or non-elastic scattering for Monte Carlo simulations would not significantly affect the results. (White and Dale 2014) used Monte Carlo methods to simulate intra and extra cellular diffusion. (Sukstanskii and Yablonskiy 2008; Grebenkov, Guillot, and Sapoval 2007) simulated diffusion of gases in lungs for diffusion NMR applications. (Grebenkov, Nguyen, and Li 2013) simulated diffusion NMR of porous media using random walk methods. Finally, here Monte Carlo simulations were used to simulate hindered or semi-restricted diffusion in prostate ducts (Gilani, Malcolm, and Johnson 2016b).

Chapter 2: MR Related Histological Changes in PCa

2-1: Introduction

Histopathology is a field science dedicated to microscopic assessment and characterization of different types of disease from biopsies or surgically resected specimen. Samples are fixed by freezing or using chemical methods and later examined under electron microscopes. Tumours are commonly characterized by their gross descriptions such as site, size, appearance and edge, histological type, differentiation or aggressiveness grade, tumour stage or extent of spread, lymphovascular invasion, etc. (Allen 2000)

In order to assess aggressiveness of PCa histology samples, the Gleason grading systems is used (Gleason 1992; Gleason, Mellinger, and Group 2002; Epstein et al. 2005; Fine and Epstein 2008; Epstein, Zelefsky, et al. 2016; Epstein, Egevad, et al. 2016; Sauter et al. 2016; Gleason 1977). While morphological changes in the cells occur with increasing Gleason grade, they are not used to calculate the Gleason grade. Hence, Gleason grading system is solely a measure of the extent of abnormalities in glandular architecture (Sauter et al. 2016). Grades of 3 and below are for poorly differentiated (non-aggressive) cancer, whereas grades of 4 and 5 are for well differentiated (aggressive) cancer. For needle biopsies two or three samples with the most and worst Gleason pattern are used to calculate the score (such as 3+4, 5+4 or 5+4+3), whereas for radical prostatectomy specimens and transurethral resections the first two or three most frequent patterns give the score. Obviously, the scores for needle biopsies are not as accurate as whole mount prostate specimens due to sampling error (Sauter et al. 2016; Corcoran et al. 2012). This is because prostate tumours are highly multifocal and heterogeneous compared to other tumours and hence small volumes of high grade tumours might be missed during the biopsies (Corcoran et al. 2012). The most important deficiency of Gleason grading is being qualitative; consequently better quantification of its components or introducing alternative grading systems

has been the subject of recent studies (Sauter et al. 2016; Epstein, Zelefsky, et al. 2016).

There have been several studies, such as (Bourne, Kurniawan, Cowin, Stait-Gardner, Sved, Watson, and Price 2012; Bourne et al. 2011; Bourne et al. 2013; Bourne, Kurniawan, Cowin, Stait-Gardner, Sved, Watson, Chowdhury, et al. 2012; Chatterjee et al. 2015) investigating histological changes observed in cancerous samples and their effect on high field diffusion MR *ex vivo*. Since there are not any biological concerns for examining *ex vivo* samples using very high magnetic fields (generally greater than 7 Tesla) and very long scan times, considerably high resolution T_2 or diffusion images could be acquired for *ex vivo* specimens such as in (Bourne et al. 2011; Bourne et al. 2014; Chatterjee et al. 2015). While some of the diffusion-related parameters extracted from these studies show the extent of such correlations, care should be taken if the aim is to apply the results to *in vivo* MRI analysis. The extracted parameters from *in vivo* and *ex vivo* MR are considerably different because of a variety of fixation effects (Bourne et al. 2013), temperature differences (Bourne et al. 2013) and also diffusion time differences (Hall et al. 2015; Gilani, Malcolm, and Johnson 2016b).

For example, using micro-diffusion MRI methods *ex vivo*, the diffusion coefficients of pure ducts, stromal cells and epithelial cells have been respectively estimated to be around 2-2.2, 0.7-0.9, and 0.3-0.5 $\mu m^2 ms^{-1}$ (Bourne, Kurniawan, Cowin, Stait-Gardner, Sved, Watson, and Price 2012; Bourne et al. 2011). These results imply relatively free diffusion in the ductal lumen and restricted diffusion in the stroma and epithelial compartments. However, these values are substantially less than the diffusion measurements from *in vivo* diffusion MRI of the prostate. Additionally, microscopic volume measurements of fixated prostate tissue are usually an underestimate of the actual volume by a factor of 1.22 to 1.5 (Schned et al. 1996; Noguchi et al. 2000; Tran et al. 2015). While so far it is not known which of the three compartments accounts for most of this tissue shrinkage, the ducts as empty spaces are the primary candidates for this volume shrinkage. This alters the diffusion-related parameters in

addition to significant effects of temperature and other fixation effects. The *ex vivo* samples are usually scanned at room temperatures, and hence the measured diffusion coefficients are considerably lower than *in vivo* MR scans. Additionally, there are other fixation effects which result in differences for *ex vivo* and *in vivo* measurements. Moreover, the scanning protocols are different such as most importantly having different diffusion pulses or diffusion times *ex vivo* (Bourne et al. 2013; Thelwall et al. 2006; Kim et al. 2007).

Although the changes seen in cellular parameters are qualitatively well understood, few MR related quantitative measurements exist, such as measurements of compartmental volume fractions in (Chatterjee et al. 2015). Here, measurements of ductal radius (Gilani, Malcolm, and Johnson 2016b), cell size and cellular density were therefore performed.

Changes in Volume Fraction of the Compartments in PCa

It has been shown in (Chatterjee et al. 2015) that increases in cell density with increasing cancer grade does not directly lead to decreases in apparent diffusion coefficient (ADC) values for prostate cancer, unlike other cancers. Rather, it is the replacement of stromal cells and ductal spaces by epithelial cells that leads to increases in cellularity and hence indirectly results in reductions in ADC's seen in prostate cancer. Table 2.1 shows the volume fraction of each of the three self-diffusion compartments for different grades of cancer from (Chatterjee et al. 2015).

Table 2.1: Volume percentage of ducts, epithelial, and stromal cells for different grades of cancer from (Chatterjee et al. 2015). TZ is the transitional zone, PZ is the peripheral zone and CG is the central gland. The values were extracted with permission from the journal of Radiology.

	Stroma	***Epithelium***	***Lumen***
PZ (n=198)	*39.4*	*31.4*	*29.3*
TZ (n=102)	*48.9*	*26.6*	*24.6*
CG (n=75)	*38.0*	*35.9*	*26.1*
Gleason Grade 3 (n=94)	*34.2*	*48.9*	*16.8*
Gleason Grade 4 (n=23)	*28.6*	*58.5*	*12.8*
Gleason Grade 5 (n=14)	*24.3*	*68.6*	*7.2*

Changes in the Ductal Sizes

The radius of the ductal lumen seen in histological sections of the normal prostate is around ~300 μm (Gorelick et al. 2013; Zynger and Parwani 2014) which is at least an order of magnitude greater than three dimensional Einstein diffusion distance of ~45 μm (assuming a diffusion time of 80 ms, typical of clinical scanners, and diffusion coefficient of 3 $\mu m^2 ms^{-1}$, similar to that of water (Mills 1973; Harris and Woolf 1980) at body temperatures). Therefore, the residence time of a water molecule within ducts in normal prostate is likely to be long compared with the diffusion time. Consequently, the ductal and cellular (i.e., epithelial plus stromal) spins will effectively reside in separate compartments and generate separate signals each with its own characteristic parameters. Although there are no direct experimental demonstrations of separate ductal and cellular compartments, the hypothesis is consistent with the observation of biexponential diffusion (Mulkern et al. 2006; Shinmoto et al. 2009) and T_2 relaxation (Storås et al. 2008) . The ADC of the fast diffusing (2-3 $\mu m^2 mm^{-1}$) (Mulkern et al. 2006; Shinmoto et al. 2009) and long T_2 (~500ms) (Storås et al. 2008) components in the prostate are typical of fluids and are much greater than values found in cellular tissue (ADC ~ 0.7 $\mu m^2 mm^{-1}$ (Papanikolaou et al. 2002) and T_2 ~80ms (Steens et al. 2004) in the brain, for example). Therefore it was hypothesised that the biexponential signal components seen in DWI (and T_2 relaxometry) of the prostate arise primarily from the distinctly different diffusion and T_2 glandular fluid and the cellular compartments within the prostate.

Changes in Cell sizes

It has been observed in (Montironi et al. 2000) that the average nuclear area of the columnar epithelial cells surrounding the ducts increases with increasing Gleason grade. They measured average nuclear area of the epithelial cells to be around 36, 56, and 61 μm^2 for normal prostate and Gleason Scores 6 and 7, respectively. This corresponds to average radii of respectively around 3.4, 4.2 and 4.4 μm for each, if the cells are assumed to

be perfectly spherical. Consequently, there might be increases in the total ADC with increasing cancer grade but the effects is negligible.

Changes in Cell Density

With increasing cancer grade, cellular density (nuclear density) of the epithelial compartment increases (Langer et al. 2010; Gibbs et al. 2009). (Langer et al. 2010) measured percentage area of cells (with total area including ducts, stroma and epithelium) in histology samples to be 14.5%, 22.4%, and 25.4%, respectively, for healthy PZ and Gleason scores of 6 and 7 in 22 patients. In another study, Gibbs et al. (Gibbs et al. 2009) have measured this parameter to be 9% and 19.2% for healthy PZ and unknown grades of cancer in 65 patients, respectively.

It should be noted that the measured densities above are interdependent on the volume fractions measured in (Chatterjee et al. 2015). To nullify this, here cellular densities of cellular and stromal compartments were estimated separately from histology images (Zynger and Parwani 2014; Gorelick et al. 2013; Epstein, Egevad, et al. 2016; Epstein et al. 2005) using ImageJ (Schneider, Rasband, and Eliceiri 2012) as shown in table 2.3.

Changes in the Vascular Compartment

With increasing cancer grade the vascular compartment increases in size. Schlemmer at al.(Schlemmer et al. 2004) measured vascular volumes of 2% in normal peripheral zone, rising to 4% in prostate cancer.

2-2: Methods

Ductal Radii Measurements

Here, average radii of the ducts for different grades of PCa were measured using two different references (Zynger and Parwani 2014; Gorelick et al. 2013). The histology sections were scanned and loaded in to ImageJ V1.48 (Schneider, Rasband, and Eliceiri 2012). The lumen of individual ducts were segmented and the area measured precisely. Later, in order to

estimate the Radii from the measured areas, circular lumen assumption was made (i.e., $r = \sqrt{A/\pi}$, where A is the lumenal area). A minimum of 20 different measurements were obtained for each figure from each source and the minimum, maximum and mean radii recorded. The process was performed on sections of normal peripheral zone, Gleason grades 3, 4 and 5, and a section with Gleason score 3+4.

Cell Radii and Density Measurements

Here, the radii of epithelial and stromal cells for healthy and different grades of cancer were estimated from histology images of references (Zynger and Parwani 2014; Gorelick et al. 2013; Epstein, Egevad, et al. 2016; Epstein et al. 2005). Images were scanned and cell area measured using ImageJ (Schneider, Rasband, and Eliceiri 2012). Individual cells were segmented and the precise area measured. Later, radii were calculated assuming circular cells (i.e., $r = \sqrt{A/\pi}$ where A is the cellular area). A minimum of 10 - 20 different measurements were obtained for each figure from each source and the mean radii recorded. The process was performed on sections of normal peripheral zone, Gleason grades 3, 4 and 5.

Additionally, the cellular density of stromal and epithelial cells were measured separately for each of the above samples. The stromal cell density (Den_s) was defined as percentage of intracellular area to the total area in a pure stromal section. Similarly, epithelial cell densities (Den_e) were measured for pure epithelial sections.

Epithelial Thickness Measurements

Additionally, to obtain an estimate of stromal/epithelial exchange times, the average thickness of epithelial cells was estimated by making measurements from histology images of normal and cancerous prostate (Gorelick et al. 2013) using ImageJ (Schneider, Rasband, and Eliceiri 2012).

.

2-3: Results

Ductal Radii Measurements

Radius measurements obtained on data from the two different sources (Zynger and Parwani 2014; Gorelick et al. 2013) did not appear to differ substantially, so they were combined. Consistent reductions in diameter with increasing tumour grade were observed. The results are given in table 2.2.

Table 2.2 Ductal radius for different Gleason grades and Gleason Score of 3+4 from (Gilani, Malcolm, and Johnson 2016b)

	Ductal Radius ***Mean ± SD (range) / µm***
Healthy PZ	300 ± 120 (50 - 500)
Grade 3	65 ± 36 (15 - 110)
Score 3+4	45 ± 24 (5 -110)
Grade 4	30 ± 13 (5 - 50)
Grade 5	20 ± 8 (3 - 40)

Cell Radii Measurements

The cell radii and density measurements for sections of normal peripheral zone, Gleason grades 3, 4 and 5 are shown in table 2.3. There were consistent increases in the epithelial cell sizes and densities with increasing cancer grade.

Table 2.3 The measured radii and cell density of stromal and epithelial cells for normal and different grades of prostate cancer. r_s, r_e, Den_s and Den_e are respectively the average radii of stromal and epithelial cells and average cell density of stromal and epithelial cells. Std is for standard deviation.

	Healthy (mean ±std)	***G3 (mean ±std)***	***G4 (mean ±std)***	***G5 (mean ±std)***
r_s / µm	3.7 ± 0.35	3.7 ± 0.35	3.7 ± 0.35	3.7 ± 0.35
Den_s (%)	13 ± 3	13 ± 3	13 ± 3	13 ± 3
r_e / µm	3.4 ± 0.15	4.25 ± 0.13	4.55 ± 0.15	4.75 ± 0.2
Den_e (%)	45 ± 5	60 ± 6	65 ± 7	70 ± 8

Epithelial Thickness Measurements

Average epithelial thickness measured to be 8.2±1.3 µm (12 measurements) and 18.3±5.4 µm (7 measurements) for healthy prostate and Gleason score 7, respectively.

Chapter 3: Monte Carlo Simulation of Ducts

The material in this chapter is mostly derived from (Gilani, Malcolm, and Johnson 2016b) with copyright permission license (3915891478574) from John Wiley and Sons to use the full article.

3-1: Introduction

In order to consider diffusion within the complex tissue structure of prostate, it is better to consider each compartment separately. This is possible only if the residence times within each compartment are long compared to the diffusion times. Accordingly, the main purpose of this chapter is to test whether ducts give an independent diffusion signal and, if yes, to simulate their corresponding signal.

Hyperpolarized ^{3}He studies in the lungs (Fain et al. 2010) and studies in porous media (Shemesh et al. 2010; Sen 2004; Latour et al. 1995) have demonstrated that ADC depends on the size of the cavity in which the studied molecule resides as well as diffusion times. Additionally, (Jensen et al. 2005; Jensen and Helpern 2010) have shown how hindrance, compartmentalisation and restriction result in non-Gaussian diffusion. References (Codd and Callaghan 1999; Callaghan 1997, 1995; Price 2009) presented analytical formulations for restricted diffusion inside cylindrical, spherical and planar cavities. The non-Gaussian nature of restricted diffusion was recognised in these studies but the diffusion decays were assumed to be simple exponentials for simplicity. Presenting analytical solutions that include the effects of non-Gaussian behaviour of diffusion might be possible but is mathematically complex even for simple geometries. Monte Carlo simulation is an alternative to analytical methods that is both easily extensible to non-Gaussian distributions and also to complex geometries. Monte Carlo simulations of restricted diffusion in two compartments (Fieremans et al. 2010) and in-depth analysis of restricted diffusion (Novikov et al. 2011) have already been published; however Monte Carlo simulation of non-Gaussian diffusion in single compartments has not been published previously.

It has been shown in the previous chapter that the average radius of ducts decreases with increasing cancer grade. The purpose of this chapter was therefore to use Monte Carlo simulations of permeable cavities to determine the relationship between permeability, cavity size, and residence times; and to establish plausible limits to residence times. Consequently if the residence times were long enough, to use Monte Carlo simulattions of impermeable cavities to investigate the effect of increasing cancer grade (reductions in ductal sizes) on diffusion. Approximating permeable cavities with long residence times by impermeable cavities greatly simplifies the simulations and has been adopted in previous studies (Li, Calhoun, et al. 2014).

3-2: Residence Times

Permeability, residence time and MC methods

Residence time of water molecules within the ductal compartment is determined by size of ducts and the permeability of their boundaries, which is described in units of μms^{-1} for MR applications. (Regan and Kuchel 2002, 2000) and (Lee, Bennett, and Debbins 2013) calculated the equivalent probability, *p*, of crossing upon hitting a barrier in random walk simulations:

$$p = k\sqrt{\frac{6Dt}{D_{free}}} \tag{3.1}$$

where κ is permeability, D_{free} is the diffusion coefficient in the absence of barriers, and Δt is the time step of the random walks.

Here, the residence time calculations were performed in MATLAB Release 2013b (MathWorks, Natick, MA, United States). Residence times were estimated from simulations similar to those of (Regan and Kuchel 2000) and (Fieremans et al. 2010). Spins were placed randomly within spherical cavities and random walks were simulated as follows. At each time step, the spin was moved a fixed distance $\Delta\mathbf{r}$ in a random direction. The length of $\Delta\mathbf{r}$ was determined by the unrestricted diffusion coefficient of the fluid,

$$|\Delta \mathbf{r}| = \sqrt{6 D_{free} \Delta t} \tag{3.2}$$

where Δt, the step time, is T_D divided by N_s, the number of steps in the simulation. Here it has been assumed that D_{free} was that of free water at 37°C (3.08 $\mu m^2 ms^{-1}$) (Mills 1973; Harris and Woolf 1980). A Δt of 25μs was used giving $|\Delta \mathbf{r}| \approx 0.65 \mu m$.

If the step $\Delta \mathbf{r}$ took the spin beyond the boundary of the cavity a random number was drawn from a uniform distribution with minimum zero and maximum one. If this value was less than the assigned probability of crossing (3.1), the spin was assumed to have exited and the total time to that point recorded. Otherwise, the spin was placed back at its previous position and randomly moved in a different direction at the next step. This approach has previously been shown to give similar results to the alternative of elastic reflection (Xing et al. 2013). This procedure was repeated for 1,000,000 spins and the mean of all times recorded as the mean residence time.

The ductal lumen is surrounded by a layer of epithelial cells with thickness of ~10-20 μm measured from histologic samples of (Gorelick et al. 2013; Zynger and Parwani 2014). As it was shown in the previous chapter, the thickness of the epithelial layer increases with cancer grade and hence makes ducts relatively less permeable to the cellular compartments. The permeability of cells walls has been estimated to be anywhere between 6 and 200 μms^{-1} (Finkelstein 1987; Regan and Kuchel 2003; Benga et al. 2000; Haines and Liebovitch 1995). Therefore, the simulations were performed with somewhat conservative overestimates of permeability for the ductal walls, twice the maximum value found in cell walls, 400 μms^{-1}. With this permeability, the probability of a spin crossing the cavity wall on hitting it is 8.8% from Eq. (3.1).

Residence times of the ducts

Table 3.1 gives the estimates of residence times for ducts in tissues of different Gleason grades, conservatively assuming a high permeability

value of 400 μms^{-1}. These times are at least comparable with typical *in vivo* diffusion times at least up to Gleason score 3+4. The times are also somewhat greater than intracellular residence times measured for glioma cells (50 ms (Pfeuffer et al. 1998)), bovine optic nerve (62 ms (Stanisz et al. 1997)), and red blood cells (10-14 ms (Herbst and Goldstein 1989)). Also it should be noted that for high grades of cancer the ducts are covered by fully packed epithelial cells (i.e. the epithelial thickness measurements in the previous chapter) which means that the permeability levels are lower than the pessimistic value of 400 μms^{-1} and are in orders of cell walls. As a result, their corresponding residence times might be substantially longer that the values in table 3.1.

Table 3.1: Residence time of water molecules in the ducts for different Gleason grades and Gleason Score of 3+4 assuming constant pessimistic permeability of 400 μms^{-1}

	Residence Time / ms
Healthy PZ	2100
Grade 3	130
Score 3+4	70
Grade 4	35
Grade 5	21

3-3: DWI Simulations

The average distance moved by a freely diffusing spin in three dimensions is given by the Einstein diffusion equation (Einstein 1905):

$$\langle r \rangle = \sqrt{6 D_{free} T_{TD}} \tag{3.3}$$

where D_{free} is the unrestricted diffusion coefficient or diffusion coefficient in very small times compared to the boundaries and T_{TD} is the total diffusion time or the time over which diffusion measurement occurs. Note the distinction between the total diffusion time, T_{TD}, and diffusion time, T_D, as normally defined in the MRI literature; T_{TD} (Lori, Conturo, and Le

Bihan 2003) is the total period over which diffusion affects the outcome of the experiment

$$T_{TD} = \Delta + \delta \tag{3.4}$$

where δ is the length of the diffusion gradients, and Δ is the interval between their centers, T_D is a convenient constant that arises when calculating gradient *b*-values

$$T_D = \Delta - \frac{\delta}{3} \tag{3.5}$$

When the spin is constrained within a small cavity the apparent diffusion coefficient, *D*, will be reduced. From Eq. (3.3) it is clear that *D* is a function of the ratio, α:

$$\alpha = \frac{r_d^2}{T_{TD}} \tag{3.6}$$

where r_d is the radius of the cavity. In other words, when diffusion times are long, spins diffuse further and reach the walls of relatively large cavities. Conversely, spins reach the walls of small cavities in short diffusion times.

The following asymptotic behavior of *D* is expected:

$$\begin{aligned} \lim_{\alpha \to 0} D &= \frac{\alpha}{6} \\ \lim_{\alpha \to \infty} D &= D_{free} \end{aligned} \tag{3.7}$$

i.e., for very small α, all spins traverse the cavity many times and the measured diffusion coefficient is dependent on $\langle r \rangle = r_d$; for very large α, most spins never reach the walls of the cavity and diffusion is effectively free.

When diffusion is restricted or the diffusion signal arises from more than one compartment, the probability density function, P(*r*), describing diffusional displacement becomes non-Gaussian. The excess kurtosis, *K*, is

the normalized the fourth moment of P (Jensen et al. 2005; Jensen and Helpern 2010):

$$K = \frac{\int r^4 P(r) dr}{(\int r^2 P(r) dr)^2} - 3 \tag{3.8}$$

where r is displacement and the subtraction of 3 is conventionally applied to ensure that the kurtosis of a Gaussian is zero. For non-Gaussian P, K becomes non-zero. Kurtosis is a complex function that depends on tissue complexity and microgeometry, the disparity in diffusion coefficients between different tissue components and the degree of restriction (Jensen et al. 2005). In this chapter, kurtosis is only a function of the degree of restriction in the simulated component. When α is large, P is nearly Gaussian and K is close to zero. Conversely, when α is small, each molecule traverses the cavity many times, P becomes increasingly platykurtic (boxy) as it approaches a boxcar function for which it is simple to show that K = -1.2. Accordingly the following asymptotic behavior of K is expected:

$$\begin{aligned} \lim_{\alpha \to 0} K &= -1.2 \\ \lim_{\alpha \to \infty} K &= 0.0 \end{aligned} \tag{3.9}$$

If residence times are long compared to diffusion times, then semi-permeable cavities can be approximated by impermeable cavities. This approach has been used previously and greatly simplifies simulations (Li, Calhoun, et al. 2014). Moreover, the probability that a spin crosses the boundary at a single collision is less than 10% even with a high permeability value of 400 μms^{-1}. Hence, even with permeable barriers diffusion is substantially impeded. Therefore the approximation is reasonable.

Six different radii (r_d = 10, 20, 30, 40, 50, and 60μm) and 12 values of T_D (40, 50, 60, 64, 70, 80, 90, 100, 133, 150, 180 and 200 ms) were simulated to give a total of 27 different values of α for spherical cavities. This range of values gives a range of α such that predicted values of D range between zero and D_{free}. Five different radii (r_d = 10, 20, 30, 50 and 90μm) and 3

values of T_D (50, 80 and 100 ms) were simulated to give a total of 12 different values of cylindrical α. Cylinder height, z, was either two or four times the radius. Some values of α were simulated multiple times with different combinations of r_d and T_D.

Spins were placed randomly in these cavities and 40,000 random walks generated as above for each cavity.

Phase shifts caused by Stejskal-Tanner (Stejskal and Tanner 1965) PGSE gradients and hence the signal were calculated using the method of (Hall and Alexander 2009). At each step, i, each spin accumulates a phase $\delta\phi_i$ relative to spins at the zero point of the gradients

$$\delta\varphi_i = \gamma \mathbf{G}.\mathbf{r}\Delta t \tag{3.10}$$

where γ is the gyromagnetic ratio, $\mathbf{r}$ is the position of the spin, $\mathbf{G}$ is the applied gradient and Δt is the time of each step. The signal from each spin is equal to the cosine of the final phase

$$s = \cos\left(\sum_{i=1}^{N_s} \delta\varphi_i\right) \tag{3.11}$$

and total signal is the sum of the signals from all spins. This calculation was performed separately for x, y and z diffusion weighting gradients using the same trajectories.

It is required to average the signal in at least 6 non-perpendicular or 3 perpendicular acquisition directions to derive the weighted ADC values if the Gaussian estimate of diffusion is used (Westin et al. 2002). However, for non-Gaussian diffusion kurtosis imaging, the averaging should be performed in at least 15 directions (Jensen et al. 2005). Diffusion is direction dependent in cylinders and diffusion coefficients are different in the direction parallel to the axis of the cylinders compared to the perpendicular directions. As a result, these calculations were performed in 15 different directions and averaged to cancel directionality effects.

Estimates of apparent diffusion coefficient and apparent diffusion kurtosis were obtained from the simulated signals. The following expression (Jensen et al. 2005) was fitted to the signals

$$S(b) = S(0)e^{-bD+\frac{KD^2b^2}{6}} \tag{3.12}$$

where D and K are the apparent diffusion coefficient and apparent diffusion kurtosis respectively, $S(0)$ is the signal at b-value of zero, and b or b-value is the diffusion encoding parameter which for the Stejskal-Tanner diffusion pulse sequence is given by (Stejskal and Tanner 1965)

$$b = g^2\delta^2\gamma^2\left(\Delta - \frac{\delta}{3}\right) \tag{3.13}$$

where γ is the gyromagnetic ratio, δ is the length of the diffusion weighting gradient pulses, Δ is the time interval between the pulses, and g is the amplitude of the gradients.

Signals were simulated for 50 equally distanced b values using the same spin trajectories. The maximum b-value was dependent on α and ranged from around 500 s.mm^{-2} for very high α values to around 15000 s.mm^{-2} for very low α values. The values of D and K were obtained by averaging the signal in all directions.

3-4: Results

Estimated values of D and K derived from the sphere and cylinder simulations are plotted against α in Fig. 3.1. Asymptotic values of D (3.7) are also plotted for the sphere as α approaches zero.

The simulation results agree very well with the expected asymptotes. At large radii and shorter diffusion times, D approaches the free diffusion coefficient and kurtosis approaches zero. Conversely at small radii and long diffusion times, D approaches zero and kurtosis approaches a value of -1.2, equal to that of a uniform distribution.

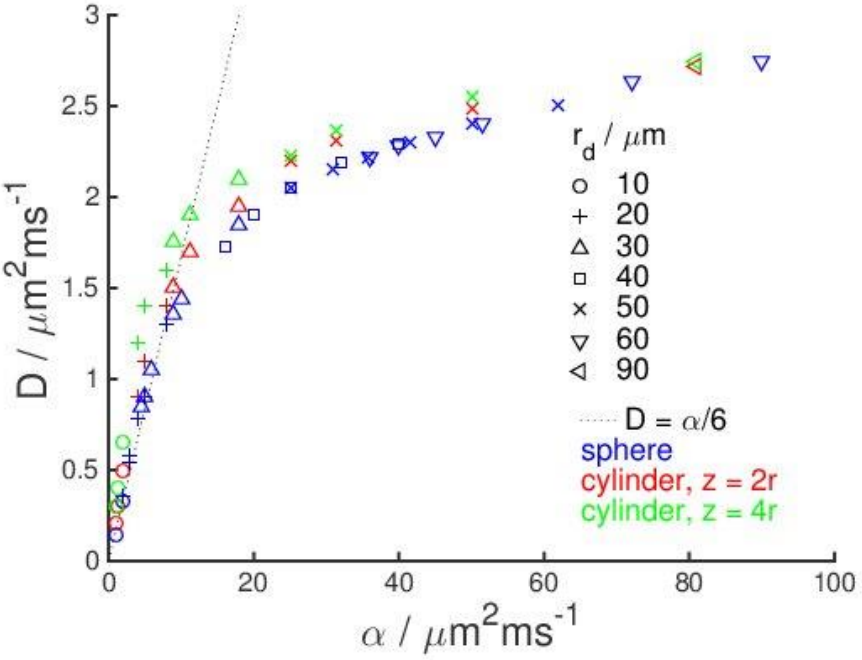

(a)

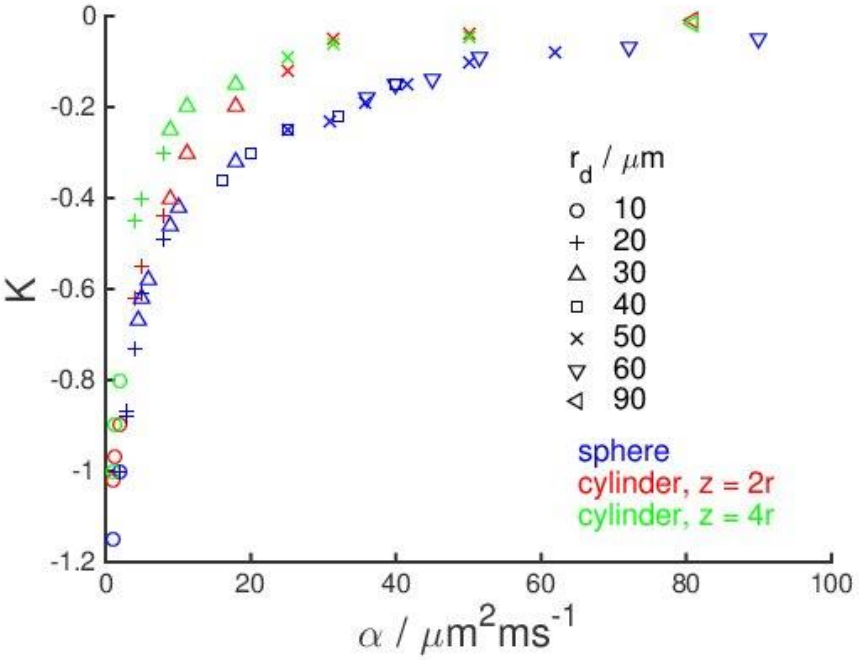

(b)

Fig. 3.1 Diffusion parameters derived by fitting Eq. (3.12) *to simulated signals, plotted as a function of α. Simulations were performed at six different radii with T_{TD} adjusted to provide the required value of α. (a) D versus α. The dotted line denotes the asymptote for (α/6) from Einstein's formula. (b) K versus α.*

Fig. 3.2 is a plot of D/D_{free} and K for different Gleason sums using the measured radii of table 2.2. Other parameters were T_D = 80 ms and D_{free} = 3.08 mm^2ms^{-1}.

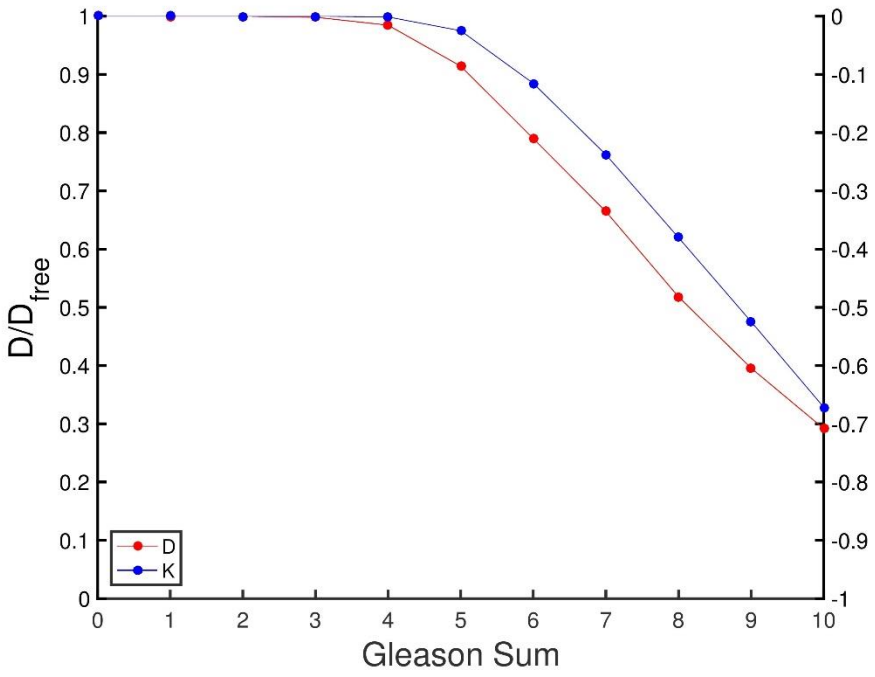

Fig. 3.2 D/D_{free} and K of lumenal fluid predicted for different Gleason sums (normal peripheral zone = 0). T_D = 80 ms and D_{free} = 3.08 mm^2ms^{-1}.

To illustrate the effect of negative kurtosis, $\ln(S/S_0)$ was plotted against the dimensionless product bD, for three different values of α in Fig. 3.3 (bD was chosen as the abscissa to emphasize the increase in relative size of the kurtosis effect at low α.) As α approaches zero, diffusion becomes increasing platykurtic and the signal drops relative to Gaussian diffusion.

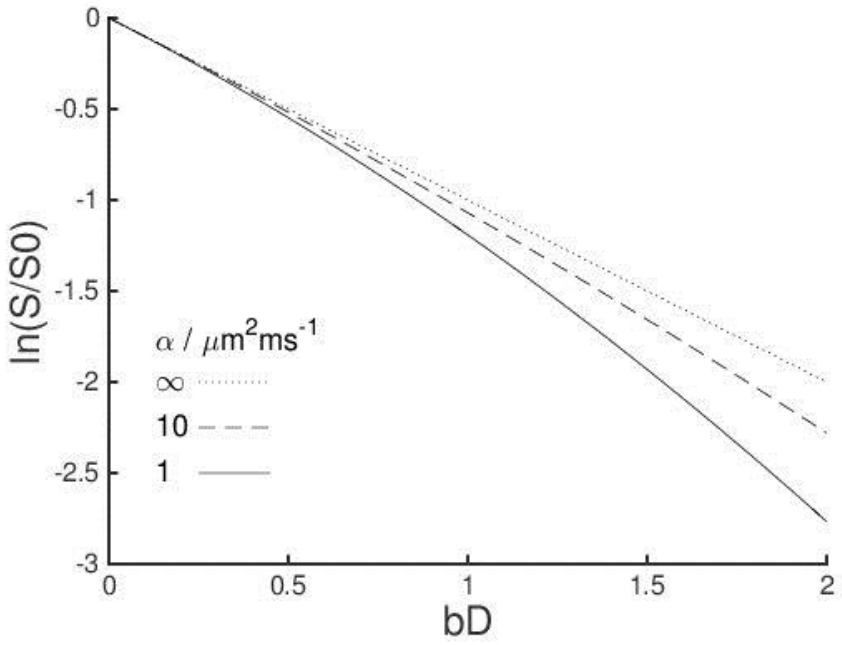

Fig. 3.3 Plot of ln(S/S0) versus dimensionless parameter bD for α = 1, 10, and 1 (ie, free diffusion), corresponding to D = 0.15, 1.44, and 3.08 mm^2mm^{-1} and K =-1.1, -0.42, and 0.

3-5: Discussion

The existence of biexponential diffusion signal for the prostate could only be explained by having at least two separate compartments with long spin residence times. It highly seems likely that the two compartments correspond to spins within the ductal fluid and the surrounding cellular tissue (stroma plus epithelium). This is consistent with two observations. First, the fast diffusion coefficient and long T_2 are typical of fluids and much greater than seen in cellular tissues. Second, simple biophysical arguments show that spin residence times in ductal fluid are long in normal prostate because ductal diameter is much greater than diffusion distances. Panagiotaki et al. (Panagiotaki et al. 2015) have attributed biexponential behavior to slow exchange between intra- and extra-cellular water. However, biexponential T_2 values observed in other tissues are ~10 and ~80 ms (Steens et al. 2004) both much shorter than the long T_2 seen in the prostate (~500 ms). Moreover, the residence times estimated for ductal lumen are rather greater that those observed for intracellular water (Pfeuffer et al. 1998; Stanisz et al. 1997; Fieremans et al. 2010). It therefore seems probable that at least some (if not most) of the observed

biexponential behavior should be attributed to separate ductal and cellular compartments.

(Jensen et al. 2005) suggested platykurtic diffusion may occur for restricted diffusion in pores but most previous reports (e.g., (Lu et al. 2006; Trampel et al. 2006; Raab et al. 2010; Fieremans, Jensen, and Helpern 2011; Anderson et al. 2014; Pentang et al. 2014)) have suggested that leptokurtic diffusion is the norm; Fig. 3.4 denotes the difference between Gaussian, platykurtic, and leptokurtic probability density functions. However, these studies considered the net diffusion properties of tissues consisting of multiple tissue components with a variety of different water exchange rates. The results here, are therefore consistent with Jensen et al.'s (Jensen et al. 2005; Jensen and Helpern 2010) finding of overall leptokurtic diffusion in tissues consisting of two exchanging Gaussian compartments. Similarly, (Rosenkrantz et al. 2012) found apparent leptokurtic diffusion for all the three compartments of the prostate as a whole but did not consider the possibility of biexponential diffusion which will mimic monoexponential diffusion with positive kurtosis over the range of *b*-values used (maximum 2000 smm^{-2}). The possibility of restricted, platykurtic diffusion may need to be taken into account in investigations of the net diffusion properties of tissues with different slowly exchanging compartments, e.g., between intra- and extra-cellular water fractions.

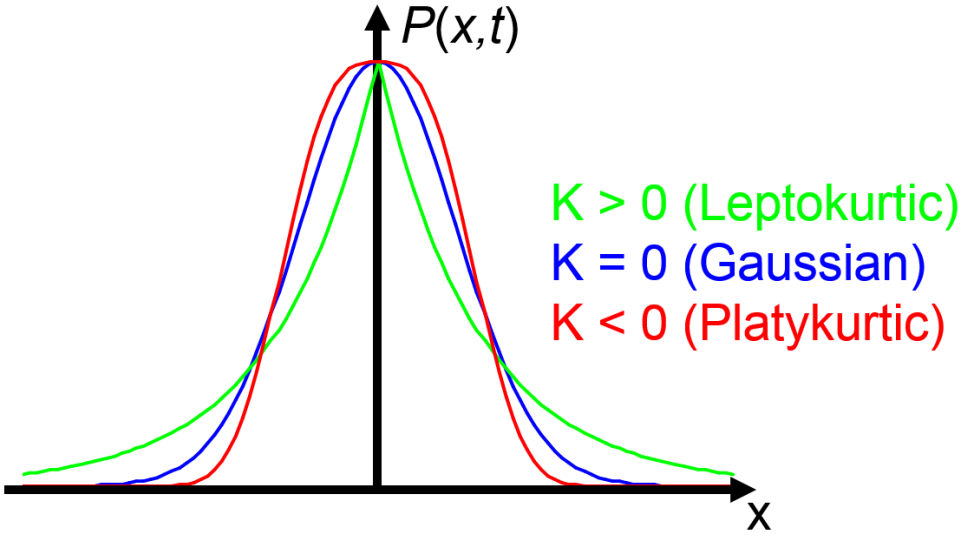

Fig. 3.4 Leptokurtic (green), Gaussian (blue), and platykurtic (red) probability density functions for diffusion in an arbitrary time t.

The effect of compartment size on measured diffusion coefficient is recognized in hyperpolarized gas imaging of the lungs (Fain et al. 2010) where alveolar enlargement in emphysema explains increases in measured diffusion coefficient. The phenomenon is also well known in diffusion measurements in porous media (Shemesh et al. 2010; Sen 2004; Latour et al. 1995) where cavity size is often explored using diffusion measurements at multiple values of T_D. Here Monte Carlo simulations were used to show that lumenal size may influence the measured diffusion coefficients of ductal fluid in the prostate. This finding is consistent with several recent studies of the prostate both *in vivo* and *in vitro.*

First, (Shinmoto et al. 2009) observed biexponential diffusion in prostate tissue and found fast ADCs of 2.9 and 1.7 $\mu m^2 ms^{-1}$ in healthy prostate and prostate cancer respectively. Their diffusion time is not given but T_E was 91ms, so T_D would be around 80ms. With this T_D an ADC of 1.7 $\mu m^2 ms^{-1}$ corresponds to r_d = 35μm (Fig. 1a). This is similar to the ductal radii measured in tissues with Gleason scores between 7 and 8 (Table 2.2).

Second, measured fast diffusion coefficients have been shown to depend on diffusion time in *ex vivo* prostate samples (Hall et al. 2015) using either Gaussian or non-Gaussian biexponential fits. This time dependency and the

dependency on cavity size are essentially the same phenomena viewed from different perspectives as could be observed in Eq. (3.6).

Finally, Chatterjee et al. (Chatterjee et al. 2015) recently showed that the relative volumes of the different prostate compartments is a determining factor in ADC measurements and, furthermore, that correlations between ADC and relative volumes were stronger than with changes in cellularity.

An association between lumenal radius and diffusion within the ductal fluid, if confirmed, would have a number of interesting implications. First, if D, K and the ductal signal fraction, f_d are all well-defined functions of r_d then an estimate of any one would allow estimation of the others, minimising the number of b values required for measurement. Furthermore, f_d could be estimated from biexponential T_2 measurements, thus further simplifying measurement. Second, as recently discussed in (Bourne 2015; Lemberskiy et al. 2015), given the diffusion time dependency of measurements, it is important that future diffusion studies of the prostate should include this parameter and consequently that scanner manufacturers should include it in sequence specifications. Finally, since the ducts have smaller sizes for higher grades of cancer, by measuring ADC as a function of diffusion time it might be possible to estimate ductal radius. Hence, at least for MR applications, the ductal sizes could more quantitatively determine Gleason grade rather than the abnormalities in ductal patterns. Although this could be challenging, Shinmoto et al. (Shinmoto et al. 2009) have previously measured reductions in the ADC of the fast diffusing component in cancer.

There are a number of limitations to these simulations. First, simulations of restricted diffusion assumed impermeable spheres. This is an unrealistic approximation that, at first sight, invalidates the assumption that restricted diffusion occurs in the prostate ducts. However, even with high permeability assumed here, the probability of a spin crossing the barrier at an individual collision is less than 10%. Consequently, although diffusion is not strictly *restricted*, it is heavily hindered and ADC will be reduced as a result. However, the estimates of ADC and K presented here must be

regarded as lower limits. Second, cylinders or spheres might not be realistic models for lumenal ducts. However, the main objective was to demonstrate that diffusion within structures of size similar to that of the ductal lumen can demonstrate restricted diffusion and thus can determine measured D_d. Finally, the free diffusion coefficient of ductal fluid may be somewhat less than that of water as assumed here because of protein concentrations (Bourne et al. 2013). This would reduce the effect of changes in ductal radius on diffusion. Conversely, the ducts may have larger sizes *in vivo* than *ex vivo*. Usually a factor of 1.15-1.5 is considered for shrinkage in size of prostate tissue *ex vivo* compared to *in vivo* (Schned et al. 1996; Noguchi et al. 2000; Tran et al. 2015). The ductal structure of prostate tissue is possibly the most suitable explanation for this shrinkage. This means that possibly most of the shrinkage happens in ducts and hence the results here might be an underestimate of ADC values in the ducts.

In conclusion, hindered or semi-restricted diffusion in cavities of similar sizes to prostate ducts may reduce ductal ADCs. This may contribute to reductions in total ADC seen in prostate cancer. Since the ADC's of the ducts are considerably greater than the cellular tissue, their effect is more dominant at lower *b*-values. Jensen et al.(Jensen et al. 2005; Jensen and Helpern 2010) have calculated the maximum *b*-values for the validity of equation (3.12) to be $3/DK$. Knowing that the maximum K is 0.5 for highest grade, its effect is significant on *b*-values of greater than 2,000 smm^{-2} which are not practical in clinical applications; this is because of the low signal to noise ratios of the scanners at such high *b*-values. Hence, it would be quite realistic to use Gaussian fits on diffusion signal arising from the ducts as one of the three diffusion compartments in the prostate.

Chapter 4: A Model for Prostate DWI

The material in this chapter is mostly derived from (Gilani, Malcolm, and Johnson 2016b) with copyright permission license (3915900076709) from John Wiley and Sons to use the full article.

4-1: Introduction

To date, the heterogeneity of prostate tissue has not been considered and diffusion MR parameters represent a weighted average of the contributions of the different compartments. Here a model of prostate tissue that takes tissue compartmentalisation of diffusion into account is introduced. As a result, the ambiguities in previous measurements are resolved and also estimation of some of the diffusion-related characteristics of ducts, stroma and epithelium might be possible. Since changes in ductal radii and the volume fractions of the three compartments are affected by cancer aggressiveness, this approach could provide an equivalent MRI score capable of distinguishing aggressive and indolent tumours. Furthermore, DWI can cover the whole prostate and hence avoids sampling error and will provide greatly improved pre-operative assessment.

4-2: Tissue Model

The model is based on measured or estimated values for the different tissue volumes and diffusion coefficients in normal prostate and cancer. The net signal arising from the tissue will depend on these parameters and on the exchange of water between different compartments. If exchange is slow relative to the time over which the signal is acquired (typically 50–100 ms), then each water molecule will effectively be confined to a single compartment and will contribute a signal characteristic of that compartment alone. Conversely, if water exchange is very fast between two compartments they are well mixed and cannot be distinguished. At intermediate exchange rates, water molecules will spend time in both compartments and will contribute a signal that represents an average between them. In normal prostate the ductal lumen is 300μm in radius (Gilani, Malcolm, and Johnson 2016b) compared with typical 2D water

diffusion distances of ~20 μm (assuming a total diffusion time of 80ms, typical of clinical scanners, and diffusion coefficient of 3.08 $\mu m^2 ms^{-1}$, similar to that of water at body temperatures (Mills 1973; Harris and Woolf 1980). Thus exchange of water between the lumen and the cellular (i.e., epithelial plus stromal) compartments is expected to be small. With increasing Gleason grade the lumenal volume decreases. Nonetheless, as it was shown in the previous chapter exchange of water molecules between the two is likely to remain slow. Similarly, the observation of an IVIM signal in most tissues suggests that exchange between the intra- and extra-vascular compartments is also slow (Koh, Collins, and Orton 2011). Stromal and epithelial layers are relatively thin, so exchange will be significant but the two cannot be considered well mixed. The validity of these assumptions is confirmed by the finding of biexponential, but not triexponential T_2 values in the prostate (Storås et al. 2008). The model (Fig. 4.1) is based on these assumptions, i.e., slow exchange between intra- and extravascular compartments; slow exchange between ductal and cellular compartments; and moderate exchange between stroma and epithelium.

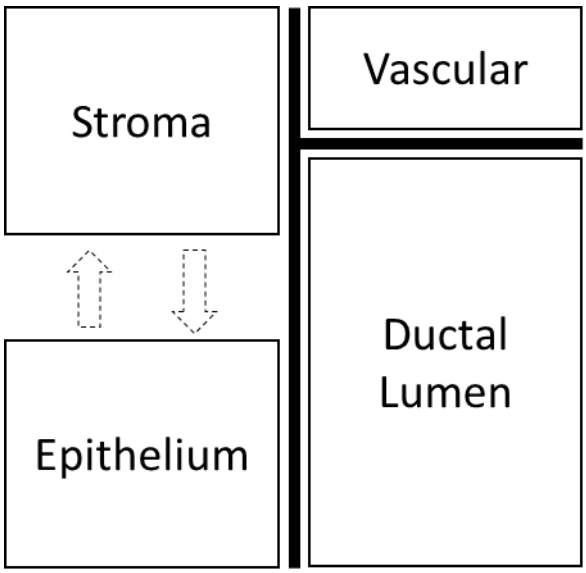

Fig. 4.1 Block diagram of the model for prostate diffusion. The model consists of four compartments: vascular, fluid-filled ductal lumen, stroma, and epithelium. Water exchange between both the vascular space and the ductal lumen and the other compartments is assumed to be negligible. Exchange between stroma and epithelium occurs, but the two are not well mixed.

With this model, the total signal, *S*, is the sum of the signals from each slow-exchanging compartment, i.e.:

$$S = S_v + S_d + S_c \tag{4.1}$$

where S_i is the signal from compartment *i* and the subscripts *v*, *d* and *c* indicate the vascular, ductal lumen and cellular compartments respectively.

Vascular Signal

The vascular fraction is small (less than 5%, see section 2-7) and becomes rapidly dephased at even low b values due to the relatively rapid capillary flow (Iima et al. 2015). S_v can thus be approximated by a delta function at $b = 0$.

Ductal Signal

It was shown in chapter 3 that the reductions in lumenal diameter found in prostate cancer will reduce D_d. The ducts were approximated as impermeable spherical cavities with different radii at different diffusion times and hence differing values of dimensionless parameter β:

$$\beta = \frac{r_d^2}{T_{TD} D_d^{free}} = \frac{\alpha}{D_d^{free}} \tag{4.2}$$

r_d is the lumenal radius (μm), T_{TD} is the total diffusion time and D_d^{free} is the diffusion coefficient in the absence of barriers. (See below for a discussion of the distinction between total diffusion time and diffusion time.) The two parameters *D* and *K* describing Ductal diffusion can be approximated by the following biexponential function:

$$D = D^{free}\left\{1 - 0.46e^{-0.0459\beta} - 0.54e^{-0.4024\beta}\right\} \tag{4.3}$$

$$K = -0.44e^{-0.0787\beta} - 0.76e^{-0.6108\beta} \tag{4.4}$$

Functions (4.3) and (4.4) were derived by fitting on figures 3.1 (a) and (b) respectively, scaling them to dimensionless parameters D/D^{free} and β. It

should be noted that the fits are precise only for routine MR diffusion times and cavity sizes in orders of prostatic ducts.

Cellular Signal

The cellular compartment consists of the stroma and epithelial sub-compartments. Exchange between these sub-compartments is intermediate between fast and slow. In such circumstances diffusion behaviour is complex. Jensen et al. (Jensen and Helpern 2010) have shown that the behaviour can be approximated by monoexponential diffusion with a kurtosis term. The cellular diffusion and kurtosis are then (Kärger 1985; Kärger, Pfeifer, and Heink 1988; Jensen and Helpern 2010)

$$D_c = D_c^{nox} \tag{4.5}$$

$$K_c = K_c^{nox} \frac{2\tau}{T_D}\left\{1-\frac{\tau}{T_D}(1-e^{-T_D/\tau})\right\} \tag{4.6}$$

where D_c^{nox} and K_c^{nox} are the diffusion coefficient and kurtosis with no exchange, T_D is the diffusion time, and τ is the exchange time between stromal and epithelial sub-compartments.

D_c^{nox} and K_c^{nox} are the given by

$$D_c^{nox} = \frac{v_s D_s + v_e D_e}{v_s + v_e} \tag{4.7}$$

$$K_c^{nox} = 3\frac{v_s (D_s - D_c^{nox})^2 + v_e (D_e - D_c^{nox})^2}{(v_s + v_e)(D_c^{nox})^2} \tag{4.8}$$

where v_i is the water volume fraction of compartment *i* and subscripts *s* and *e* refer to the stromal and epithelial sub-compartments respectively. The exchange time, τ, is given by

$$\tau = \frac{v_e \tau_s}{v_s + v_e} = \frac{v_s \tau_e}{v_s + v_e} \tag{4.9}$$

where τ_s and τ_e are the stromal and epithelial residence times respectively.

Thus, the diffusion coefficient of the cellular compartment is the average of the individual stromal and epithelial diffusion coefficients weighted by

the relative amounts of water in each; the kurtosis is similarly a weighted measure of the variance of the diffusion coefficients. When $T_D >> \tau$, the compartments are effectively in fast exchange, are well mixed and behave as a single monoexponential compartment with K_c close to zero.

Diffusion Time

Note the distinction between the total diffusion time, T_{TD}, and diffusion time, T_D, as normally defined in the MRI literature. T_{TD} is the total period over which diffusion affects the outcome of the experiment

$$T_{TD} = \Delta + \delta \tag{4.10}$$

where δ is the length of the diffusion gradients and Δ is the interval between their centres. T_D is a convenient constant that arises when calculating gradient b values

$$T_D = \Delta - \frac{\delta}{3} \tag{4.11}$$

Diffusion time also occurs in other MRI diffusion equations. However, these expressions often only strictly apply when $\delta << \Delta$. In most *in vivo* imaging sequences the diffusion gradients are applied for as long as possible to maximize *b* for a given echo time. It has recently been suggested (Lori, Conturo, and Le Bihan 2003) that in these circumstances it is better to use T_{TD} as the diffusion time.

Diffusion time is not in any case generally available (and is usually unknown to all but the sequence designers). In developing the model therefore the same approximation was used for T_{TD}.

$$T_{TD} \approx T_E - 25\text{ms} \tag{4.12}$$

This is based on the assumption that echo times have been minimized to improve SNR and a few milliseconds are required for the EPI readout gradients following diffusion weighting.

Total Signal

Both cellular and ductal compartments display non-Gaussian diffusion (i.e., the probability density function describing diffusional motion is non-Gaussian) and so should include a kurtosis term in the signal equation. However, the difference in ductal signal with and without the kurtosis term is typically less than 1%. Hence, the total signal is therefore given by

$$S = S_0 \left\{ f_v \delta(b) + f_d e^{-bD_d} + f_c e^{-bD_c + \frac{b^2 D_c^2 K_c}{6}} \right\} \tag{4.13}$$

where S_0 is the signal without diffusion weighting, f_v, f_d and f_c are the signal fractions of the vascular, ductal and cellular compartments, respectively (so that $f_v + f_g + f_c = 1$), δ is the Dirac delta function, b is the diffusion weighting constant and D_d and D_c are the ductal and cellular diffusion coefficients and K_c is the cellular diffusional kurtosis.

Model Parameters

The parameters that define the model are of two types. First, there are *a priori* parameters that are derived from literature values. Second are parameters for which no reliable estimates can be found. These are optimized by minimization of the mean square error (MSE) between model predictions and measured values.

The vascular, stromal, epithelial and ductal fractional volumes, and ductal radius of benign and cancerous prostate tissue were defined *a priori* using literature values (Chatterjee et al. 2015; Gilani, Malcolm, and Johnson 2016b) (Table 4.1). Vascular volumes are based on the measurements of Schlemmer at al. (Schlemmer et al. 2004) who found vascular volumes of 2% in normal peripheral zone, rising to 4% in prostate cancer. Gleason score was not specified so the value of 4% was assumed to correspond to Gleason 7 and other values derived using linear interpolation and extrapolation.

Table 4.1 Tissue fractional volumes, vi, signals, fi, and ductal radii, rd, used in the model for benign peripheral zone and different Gleason sums. Fractional volumes were extracted from histology measurements of (Chatterjee et al. 2015), fractional signals were calculated using Eq.(4.14)*, and ductal radii were calculated in the previous chapter.*

Tissue	Fractional Volumes (Signals)				Ductal radius, r_d / μm
	Vascular	Ductal lumen	Stroma	Epithelium	
Normal PZ	0.020 (0.031)	0.284 (0.614)	0.382 (0.195)	0.314 (0.160)	300
Gleason sum 4	0.031 (0.055)	0.203 (0.500)	0.333 (0.194)	0.433 (0.252)	135
Gleason sum 5	0.034 (0.062)	0.183 (0.467)	0.325 (0.196)	0.457 (0.275)	95
Gleason sum 6	0.037 (0.070)	0.164 (0.432)	0.318 (0.198)	0.481 (0.300)	65
Gleason sum 7	0.040 (0.079)	0.144 (0.394)	0.298 (0.193)	0.518 (0.335)	45
Gleason sum 8	0.043 (0.088)	0.124 (0.353)	0.278 (0.187)	0.555 (0.373)	32
Gleason sum 9	0.046 (0.099)	0.100 (0.299)	0.253 (0.179)	0.601 (0.424)	25
Gleason sum 10	0.049 (0.111)	0.076 (0.239)	0.228 (0.169)	0.647 (0.481)	20

The difference in water density between the vascular, ductal and cellular compartments and differences in transverse relaxation time must also be taken into account when calculating signal fractions from volume fractions. In the absence of diffusion weighting, the signal from compartment *i*, is

$$S_{i0} = k\rho_i v_i e^{-T_E/T_{2i}} \tag{4.14}$$

where k is a constant describing system gain, ρ_i is water spin density (water hydrogen atoms per unit volume), v_i is the volume fraction, T_E is the echo time of the diffusion sequence and T_{2i} is the transverse relaxation time. The fractional signal from compartment i, f_i, is therefore the ratio of S_{i0} to the sum of the signals from all compartments, i.e.,

$$f_i = \frac{\rho_i v_i e^{-T_E/T_{2i}}}{\sum_{i=v,d,s,e} \rho_i v_i e^{-T_E/T_{2i}}} \tag{4.15}$$

The ductal fluid contains few solids so that water content is ~100% whereas most soft tissues have a water content of about 75% (Reinoso, Telfer, and Rowland 1997; Kiricuta and Simplaceanu 1975) and blood is about 80% water (Beilin et al. 1966). Long and short T_2s, which supposedly correspond to the ductal and cellular (i.e., stromal plus epithelial) fractions respectively, have been measured to be about 450 ms and 60 ms (Storås et al. 2008). The T_2 of blood is about 280ms and largely independent of field strength (Stanisz et al. 2005). Signal fractions calculated from Eq. (4.15) using the above figures are given in Table 4.1.

It is not simple to obtain independent estimates of ductal, stromal and epithelial diffusion coefficients *in vivo*. *Ex vivo* MRI measurements in formalin fixed tissue at 22°C give diffusion coefficients of 2.0-2.2, 0.7-0.9 and 0.3-0.5 $\mu m^2 ms^{-1}$ for ducts, stroma and epithelium respectively (Bourne et al. 2011; Bourne, Kurniawan, Cowin, Stait-Gardner, Sved, Watson, and Price 2012). However, changes in diffusion characteristics due to cell death, fixation and temperature differences make these measurements difficult to interpret (Bourne et al. 2013; Thelwall et al. 2006; Kim et al. 2007). Several studies have reported biexponential diffusion measurements in normal PZ (Döpfert et al. 2011; Mulkern et al. 2006; Shinmoto et al. 2009). However, the fast and slow diffusion coefficients (presumably corresponding to glandular and cellular diffusion respectively) covered very large ranges: 2.5 – 8.8 and 0.2 – 1.2 $\mu m^2 ms^{-1}$ respectively. The fast diffusion coefficient is difficult to interpret because it includes perfusion signals (the IVIM effect) and variations in this measurement will also affect the slow diffusion estimate. The values of D_s and D_e that gave the best agreement between the model and experimental results were therefore found empirically in this chapter.

Cellular kurtosis depends on the ratio of diffusion time to the exchange time between stroma and epithelium. Exchange time is also unknown but can be estimated from the average diffusion distance (Einstein 1905):

$$\langle x \rangle = \sqrt{2D_c T_{TD}} \tag{4.16}$$

If it is assumed that τ is approximately the time it takes to diffuse from the centre of the stromal or epithelial layer to its edge, then

$$\tau \sim \frac{r_c^2}{2D_c} \tag{4.17}$$

where r_c is half the thickness of either the epithelial or stromal layer.

Diffusion coefficients are inversely correlated with cell density (Hayashida et al. 2006; Ellingson et al. 2010) and consequently reduced in tumours. The precise relationship between ADC and cancer grade is unknown but ADC values typically decrease with increasing grade, dropping to about 50% of normal values in high-grade tumors (Schmainda 2012; Svolos et al. 2014; Kim et al. 1999). Therefore it was assumed that the epithelial diffusion coefficient D_e drops linearly with Gleason score from a value D_e^{norm} at Gleason 0 (i.e., normal) to $0.5D_e^{norm}$ at Gleason 10, i.e.,

$$D_e = D_e^{norm}\left(1 - 0.05g\right) \tag{4.18}$$

where g is the Gleason score.

Finally, as only diffusion characteristics of epithelial cells are variable for different grades of cancer, it was assumed that the stromal diffusion coefficient is independent of grade,

$$D_s = D_s^{norm} \tag{4.19}$$

where D_s^{norm} is the diffusion coefficient of normal stroma.

The model is thus Eq. (4.13) with D_d given by Eq.(4.3), D_c by Eq. (4.7), and K_c by Eq. (4.8), with signal fractions given by Eq. (4.15).

4-3: Methods

All algorithms were implemented in MATLAB (MathWorks, Natick, MA, USA). Only published patient data were used for this study so no ethical consent was sought.

Optimum Compartmental Diffusion Coefficients, D_i

Forty-three papers were identified that presented diffusion measurements with associated Gleason scores (Anwar et al. 2014; Boesen et al. 2014; Caivano et al. 2013; De Cobelli et al. 2015; deSouza et al. 2008; Doo et al. 2012; Esen et al. 2013; Gibbs et al. 2009; Hambrock et al. 2011; Hosseinzadeh and Schwarz 2004; Ibrahiem et al. 2012; Issa 2002; Jambor et al. 2016; Kagebayashi et al. 2012; Kozlowski et al. 2006; Langer et al. 2010; Li, Margolis, et al. 2014; Luczynska et al. 2014; Manenti et al. 2007; Mazaheri et al. 2012; Nagarajan et al. 2012; Nguyen et al. 2016; Panagiotaki et al. 2015; Park et al. 2016; Pickles et al. 2006; Reinsberg et al. 2007; Rosenkrantz et al. 2012; Rosenkrantz et al. 2015; Sato et al. 2005; Shinmoto et al. 2009; Suo et al. 2014; Tamada et al. 2008; Tamura et al. 2014; Tanimoto et al. 2007; Turkbey et al. 2011; Ueda et al. 2016; van As et al. 2009; Vargas et al. 2011; Verma et al. 2011; Wang et al. 2015; Woodfield et al. 2010; Xu et al. 2009; Yoshimitsu et al. 2008) and included b values. (No attempt was made to perform an exhaustive search and this does not represent a complete list of prostate diffusion studies.) In three studies, field strength was not reported (Anwar et al. 2014; Woodfield et al. 2010; De Cobelli et al. 2015). Studies were divided into two categories according to the precision with which Gleason score was specified:

I ADC recorded for individual Gleason scores.

II ADCs recorded for groups with an average (mean or median) Gleason score.

If separate ADC estimates were made for different Gleason scores with the same Gleason sum in a study, each measurement was included separately with the same Gleason sum. If measurements of multiple readers were reported for the same Gleason sum in a study, each was treated as a separate measurement. Additionally, in one case (Hambrock et al. 2011) tertiary Gleason scores were given but were ignored.

In all studies, measurements were made at two or more *b* values and ADCs were estimated assuming a single compartment displaying Gaussian diffusion so that signals were assumed to be given by

$$S = S_0 e^{-bD} \tag{4.20}$$

These data were used to find the compartmental diffusion related parameters (i.e., D_d^{free}, D_e^{norm}, D_s^{norm}) that maximise agreement with the model predictions. Fig. 4.2 gives a flow chart outlining the process. The initial data were derived from the published data. Gleason score and b values were passed to the model and used to generate a set of signals, $S(b)$ using Eq. (4.13), with trial values of D_i. Eq. (4.20) is then fitted to the model signal to obtain model estimates of ADC, D_{model}. Non-linear least squares fitting (MATLAB function lsqcurvefit) is then used to find the set of D_i that minimize mean-square error, MSE,

$$\text{MSE} = \frac{\sum_{i=1}^{N} (\Delta D_i)^2}{N} \tag{4.21}$$

where ΔD is the difference between measured and model ADC and the sum is over each measurement in the published data sets.

The above procedure was initially performed using ADC measurements reported in all 43 papers to find an initial set of optimum model parameters D_i. The difference between model estimates and measured values of ADC, Δ, was then calculated for all measurement using these initial optimum values. The mean and standard deviation of the differences, Δ, were then calculated. Any measurement where Δ was greater than 1.96 standard deviations away from the mean difference were considered an outlier. Any paper reporting more than a single outlier was removed from the analysis set since this suggested the possibility of a systematic error such as incorrectly calibrated b values. The optimization procedure was then repeated with the reduced set to generate the final set of optimum model parameters.

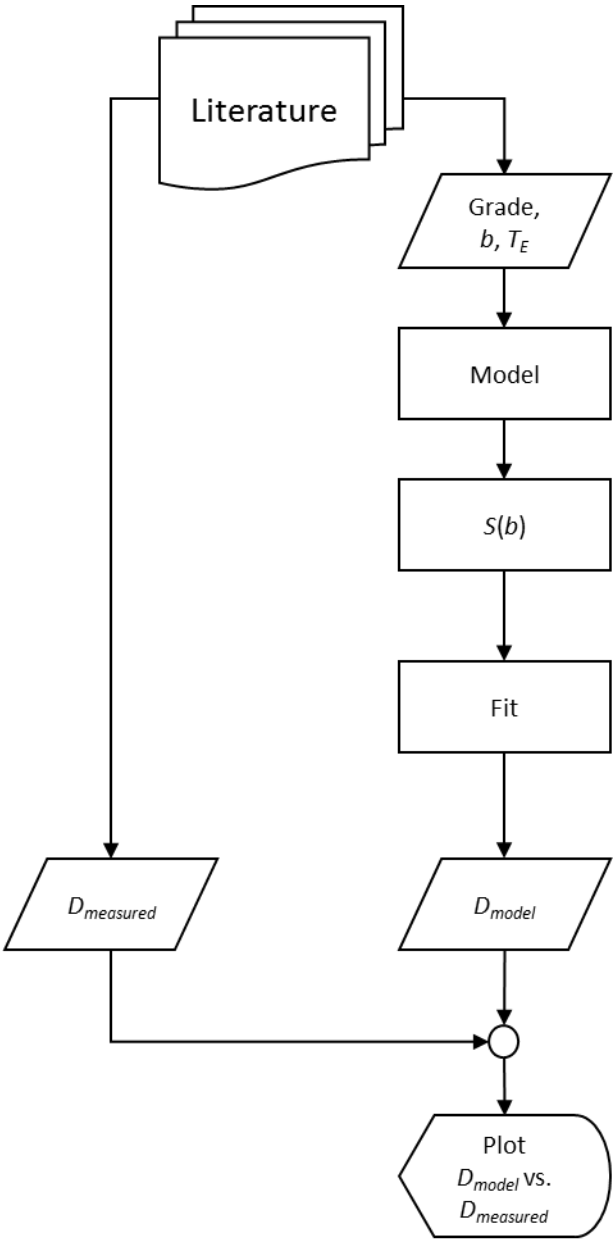

Fig. 4.2 Flow chart of the method used to determine empirical parameters of the diffusion model.

Cross-validation

Cross-validation was performed using 10-fold cross-validation (Arlot and Celisse 2010). Briefly, all tissue measurements from the 43 studies were collected into a single set of N measurements. This set was split into 10 folds, each with a group of ~N/10 test points used for testing with the remaining points used for training. Each training group is used to find a set of optimum D_i. The differences between $D_{measured}$ and D_{model} were then

found for all points in the test group using these parameters. The process was repeated for each fold and the MSE found over all test points in all folds. This method provides a moderately conservative estimate of the true MSE.

4-4: Results

Epithelial/Stromal mixing times

Using the estimates of epithelial thickness from section 2-6 and using Eq. (4.17) assuming r_c (half thickness of the epithelial layer) is ~10μm and the cellular diffusion coefficient is ~1 $\mu m^2 ms^{-1}$, the cellular mixing time (τ) estimated to be around 50ms using Eq. (4.17).

Compartmental Diffusion Coefficients

Two of the 43 papers produced more than one outlier each and were removed leaving 41 papers and a total of 140 different diffusion measurements. Optimum compartmental diffusion coefficient values of D_d^{free}, D_s^{norm} and D_e^{norm} for this reduced set were 2.368, 1.222 and 0.571 $\mu m^2 ms^{-1}$ respectively.

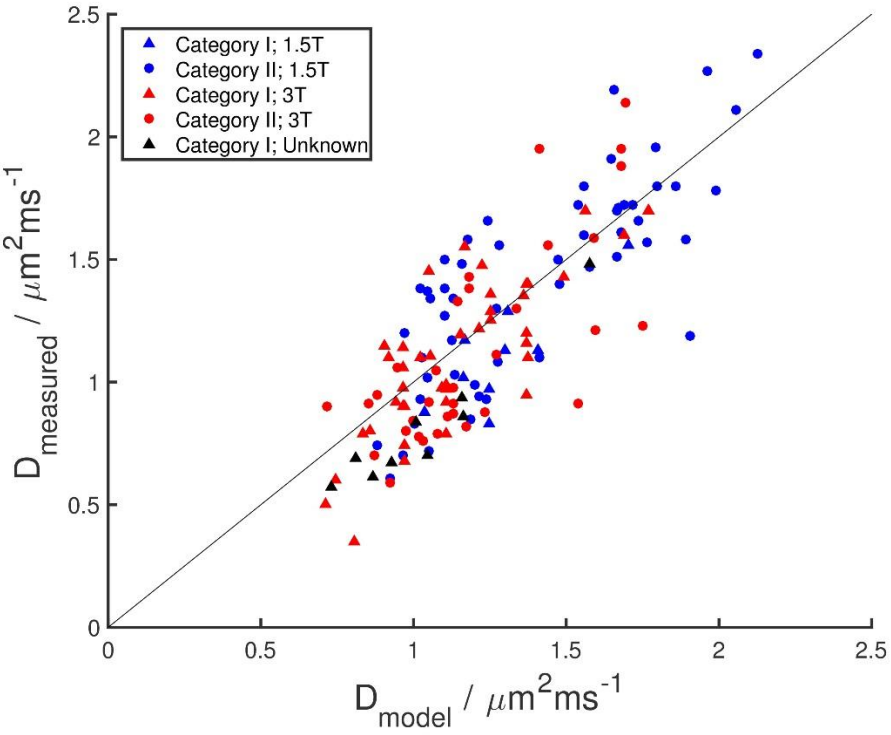

Fig 4.3 Plot comparing measured values of measured ADC ($D_{measured}$) with values predicted by the model (D_{model}). Measurements made at 1.5 T and 3 T respectively are in blue and red respectively; measurements for which the field strength is not known are indicated in black. Triangles and circles represent Category I (measurements represent a single Gleason score) and II (measurements represent an average Gleason score) papers respectively. The solid line is the line of identity.

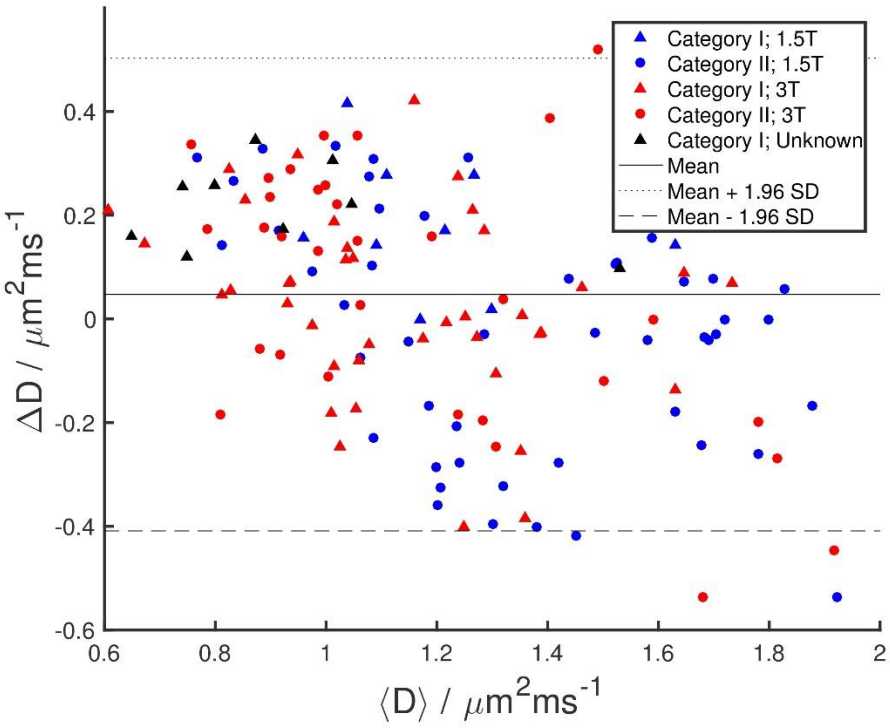

Fig. 4.4 Bland-Altman plot of $D_{model} - D_{measured}$, vs. mean, $(D_{model} + D_{measured})/2$. Measurements made at 1.5T and 3T respectively are in blue and red respectively; measurements for which the field strength is not known are indicated in black. Triangles and circles represent Category I and II papers respectively. The solid, dotted and dashed lines represent the mean difference, and the mean ± 1.96 standard deviations (i.e., the 95% limits of agreement) respectively.

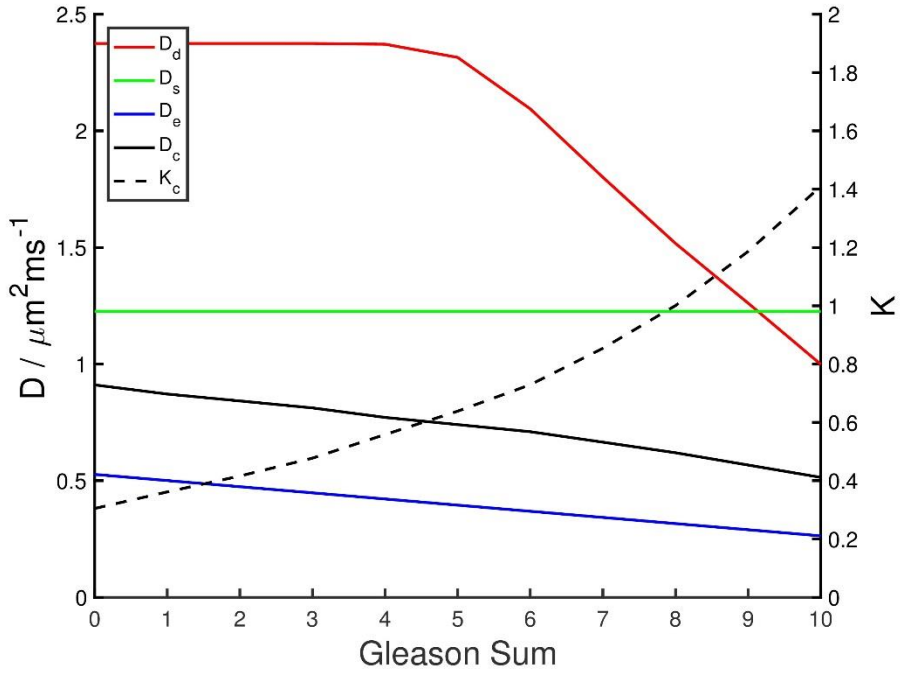

Fig. 4.5 Plot of ductal, epithelial, stromal and cellular (stromal and epithelial combined) ADC and cellular kurtosis vs. Gleason score. A score of 0 corresponds to normal peripheral zone tissue.

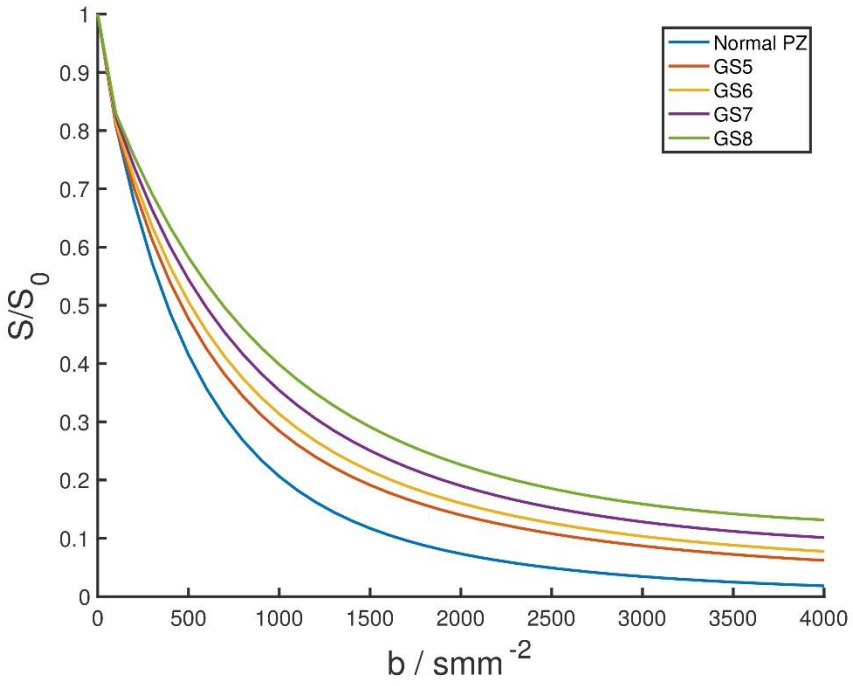

Fig. 4.6 Plot of signal vs. b value for normal peripheral zone (PZ) and Gleason scores 5 – 9. Note the discontinuity near b = 0 due to the delta function in Eq. (4.13).

Figs. 4.3 and 4.4 gives plots comparing measured values of diffusion coefficient with values predicted by the model. Fig. 4.3 is plot of $D_{measured}$ vs. D_{model}; Fig. 4.4 is a Bland-Altman plot of ADC difference vs. mean ADC. As might be expected field strength shows little or no influence on the measurements. There appears to be a slight suggestion that the scatter is greater for Category II than Category I as might be expected. Overall agreement is very good and the 10-fold cross-validation gave an MSE of 0.046 equivalent to a root MSE of 0.21 $\mu m^2 ms^{-1}$

Fig. 4.5 gives plots of D_d, D_s, D_e, D_c and K_c vs. Gleason score. (Diagnostically the most important distinction is between scores of less than and greater than six.)

Fig. 4.6 gives a plot of signal intensity predicated by the model vs. b value for normal prostate and Gleason scores 5 – 9.

4-5: Discussion

The value of an accurate model of tissue diffusion is threefold. First, it allows association of diffusion measurements with specific cellular changes, which may have valuable diagnostic implications. In this case, diffusion changes are direct consequences of changes in the relative volumes of glandular lumen, stroma and epithelium. These volumes are a key aspect of histopathological analysis and largely determine Gleason score. Hence estimates from diffusion measurements may allow calculation of an "MR Gleason Score" that predicts tumour aggressiveness. Second, knowing how changes in individual tissue compartments influence signal changes allows optimization of acquisitions (specifically choice of *b* values) to minimize errors in tissue estimates. For example, the effect of ductal size reductions is more dominant in low *b*-value ranges because the ducts have faster diffusion coefficients, the fractional value of compartments affects the signal in mid *b*-value ranges such as 700-1000 $s.mm^{-2}$, and the effect of cellular diffusion is observable at higher *b*-values. Finally, the model explains the contradictions and ambiguities found in the literature. For example, a number of studies have described the b value dependence of measured ADCs (Mazaheri et al. 2012; Esen et al. 2013;

deSouza et al. 2008; van As et al. 2009). However, this is entirely to be expected as a linear relationship between ln(*S*) and *b* will only be found for diffusion in a single Gaussian compartment. In any more complex system, the ln(*S*) vs. *b* is non-linear and cannot be described by a single ADC (i.e., a single value for the slope). The problem is particularly acute in the prostate since the two main compartments, glandular and cellular, have markedly different diffusion coefficients. The optimum prostate diffusion protocol is not then a simple matter of finding a single optimum *b* value (Metens et al. 2012) but of acquiring images at a sufficient large number of *b* values to fully describe the data. Similarly, the model explains the finding of a lowered IVIM "perfusion fraction" in tumours (Döpfert et al. 2011; Pang et al. 2013). This finding is not only counterintuitive since tumour angiogenesis generally increase blood volume, it is also contradictory to DCE perfusion measurements (Pang et al. 2013). However, the rapidly diffusing signal is not simply flowing blood displaying pseudo-diffusion, but also includes signal from the rapidly diffusing glandular compartment which shrinks in cancer.

Others have previously investigated multiexponential diffusion in the prostate. The Mulkern group observed bi-exponential diffusion behaviour in both normal prostate (Mulkern et al. 2006) and cancer (Shinmoto et al. 2009) but offered no explanation of its origin. Hall and colleagues (Hall et al. 2015) also observed bi-exponential diffusion in fixed samples. Panagiotaki et al. (Panagiotaki et al. 2015) observed tri-exponential prostate diffusion which they interpreted as arising from separate vascular (i.e., IVIM), intracellular and extracellular compartments. However, previous attributions of non-monoexponential behaviour to intra- and extracelluar compartments in the brain has been questioned for a number of reasons. First, it is simply unnecessary since non-Gaussian diffusion will always occur in the presence of hindered diffusion (Jensen and Helpern 2010). Second the signal fractions do not agree with known intra- and extra-cellar volumes (Mulkern et al. 1999; Niendorf et al. 1996). Third, magnetization transfer rates are similar for both components, which would not be expected for intra- and extracellular water (Mulkern et al. 2005).

Furthermore, if the two non-vascular diffusion components are assigned to intra- and extracellular spaces in the prostate then the cellular and glandular signals must be well mixed. This seems less likely glandular/cellular compartmentalization is a more plausible explanation of bi-exponential diffusion behaviour.

Several groups have also used non-Gaussian fits, either with a kurtosis term or using a "stretched exponential model" to describe diffusion in the prostate (Rosenkrantz et al. 2012; Hall et al. 2015; Suo et al. 2014). These methods will naturally provide better fits than more simple models. However, without including the multi-compartment nature of the prostate, these models provide little biophysical insight into the relationship between diffusion measurements and the changes that occur in cancer.

The IVIM signal in this model is described by a delta function at $b = 0$; namely, it is assumed that any diffusion weighting would effectively eliminate the perfusion signal. This is a simplification and it might be possible to develop a more accurate model with a pseudo-diffusion term that would help in diagnosis. However, there are a number of problems with this approach. First, the perfusion signal is very sensitive to low b values. However, the "$b = 0$" signal does have a small amount of diffusion weighting due to the imaging gradients. This is especially true with the large, repeated gradient pulses that are used in the EPI sequences. This introduces errors into estimates of the pseudo-diffusion parameters. Second, although blood volume is increased with tumour angiogenesis, it is not certain that blood *flow* is also increased since increased interstitial pressure caused by hyperpermeable vessels can retard flow decreasing the IVIM signal. Given the difficulty in interpretation. It is preferable to use a low, non-zero b ~150smm^{-2} for the "$b = 0$" signal.

The results primarily show that the diffusion properties of benign and cancerous prostate tissue can be described by a simple model. Most model parameters were defined *a priori* using non-MRI data. The rest were obtained by fitting the model to empirical data. The estimated values seem reasonable. D_d^{free} is somewhat lower than that of free water at 37°C (3.08

$\mu m^2 ms^{-1}$) (Mills 1973; Harris and Woolf 1980) and is similar to the *ex vivo* estimate of Bourne et al. (Bourne, Kurniawan, Cowin, Stait-Gardner, Sved, Watson, and Price 2012). D_s^{norm} and D_e^{norm} are both of the same order as the slow ADCs found by Shinmoto et al. (Shinmoto et al. 2009). Furthermore, the relative sizes are similar to those found by Bourne et al. (Bourne et al. 2011) in fixed tissue and are consistent with histological observations of greater cell density in epithelium than in stroma (Gibbs et al. 2009). All the *a priori* parameters are subject to noise and could undoubtedly be improved with further experiment.

One interesting implication of this study is that diffusion values are a product of the diffusion coefficients of the individual tissue types and Gleason score alone. Assuming the former are known, Gleason grade can, in principle, be determined via a diffusion measurement using only two *b* values. However, as is well known, noise in these measurements is relatively large. Furthermore changes in Gleason score affect the shape of the signal curve, not just the overall decay rate, so multiple *b* values will help in accurately determining Gleason score.

There are a number of limitations of this study. First, and most importantly, the data used to construct and test the model were obtained from the literature. Although this does have the advantage of explaining the variation found between measurements reported in different studies, it would be better to construct the model from measurements specifically designed for the purpose (i.e., to characterize both D_g and D_c). Such experiments are currently underway. Second, the histological diagnoses reported were derived from either biopsy samples or post-surgical whole-mount histology. It is well known that the former are much less reliable than the latter due to sampling error (Fine and Epstein 2008; Mufarrij et al. 2010; Boccon-Gibod et al. 2005; Anast et al. 2004). Similarly association between diffusion measurements and the corresponding histopathological assessments was made through a variety of different methods (quadrant by quadrant, MRI visible abnormality vs. overall Gleason score, etc.). Optimally, however, comparisons should be made between co-registered histological and MRI images. Finally, several model parameter estimates

were obtained by linear interpolation between actual measurements at particular Gleason scores. However, this is likely to be a relatively minor effect. Moreover, more accurate estimates are only likely to improve the fit of the model.

Chapter 5: Optimization of Biexponential T_2 Acquisitions

This chapter mostly draws on material from (Gilani et al. 2015) co-authored with Dr.'s Andrew Rosenkrantz, Paul Malcolm and Glyn Johnson with copyright permission license (3898710176396) from John Wiley and Sons to use the full article.

5-1: Introduction

It was shown in the previous chapters that exchange of spins between the ductal lumen and epithelium/stroma is slow. Hence the fluids in the ductal compartment demonstrate a characteristic long T_2 and the cellular tissue has a T_2 similar to that of other tissue types in the body (Storås et al. 2008). Accurate assessment of these two T_2 relaxations could help in distinguishing low and high grade tumours.

Biexponential T_2 measurements are made by acquiring signal in at least four different echo times and finding the parameters with a variety of fitting methods such as non-linear least squares, two segmented algorithms or combinations of the two. Errors in these measurements will depend on acquisition SNR's and the choice of echo times (Anastasiou and Hall 2004). Fleysher et al. (Fleysher, Fleysher, and Gonen 2008) previously determined the acquisition strategy that minimised noise in monoexponential T_2 measurements. Here, their method was extended to biexponential T_2 measurements.

Parameter estimation errors in non-linear least square fitting could be assessed either deterministically (covariance matrix) (Huang, Feng, and Phelps 1986) or by using probabilistic methods (Monte Carlo noise simulation). Here, first the covariance matrix calculations were used to minimise parameter estimation errors and then these results were tested by comparison with Monte Carlo simulations. Since it is not possible to derive general results that are applicable to any combination of T_2s, only values that were typical of the healthy and low grade tumours were studied. Furthermore, since the cellular signal fraction (1- ductal signal fraction)

was likely to be the most diagnostically useful parameter (Sabouri, Chang, et al. 2016; Sabouri, Fazli, et al. 2016), echo times that minimise errors in estimation of these parameters in particular were derived.

5-2: The covariance matrix

In general a function relating a set of measured signals, y_i (i=1, 2, …, m), to a set of measurement parameters, x_i (e.g., echo times in T_2W or b-values in DWI) is given by:

$$y_i = f(x_i; a_1, a_2, ...a_n) \tag{5.1}$$

where a_j (j=1,2,…,n) are the parameters to be estimated (e.g., T_2, D, K, etc.).

The co-variance matrix, **Q**, equals $(\mathbf{A}^T.\mathbf{A})^{-1}$ where **A** is an $m \times n$ matrix:

$$A_{ij} = \frac{1}{\sigma_0}\begin{pmatrix} \frac{\partial f}{\partial a_1}|_{a,x_1} & \cdots & \frac{\partial f}{\partial a_n}|_{a,x_1} \\ \vdots & \ddots & \vdots \\ \frac{\partial f}{\partial a_1}|_{a,x_m} & \cdots & \frac{\partial f}{\partial a_n}|_{a,x_m} \end{pmatrix} \tag{5.2}$$

where σ_0 is the acquisition noise which is assumed to be Gaussian and equal for all acquisition points. This is a reasonable assumption provided SNR is greater than about five, below which the Rician nature of noise will become apparent in the low SNR signals (Gudbjartsson and Patz 1995). Each row of **A** corresponds to a single measurement and each column to one of the estimated parameters. Thus m must be greater than or equal to n and the co-variance matrix, **Q**, is an $n \times n$ matrix. Each diagonal element,

$\mathbf{Q}_{ii}$, is the variance in corresponding parameter a_i (Huang, Feng, and Phelps 1986) and the coefficient of variation (CoV), V_i, is therefore given by:

$$V_i = \sqrt{\mathbf{Q}_{ii}} / a_i \tag{5.3}$$

The error in the i^{th} parameter may thus be minimized by minimizing V_i. In principle it might be possible to derive **Q** analytically. However, this is not generally possible so that the calculations must be performed numerically over a discrete *n*-dimensional grid of a_i values in limited ranges.

5-3: Methods

All programs and numerical simulations were performed in MATLAB Release 2013b (The MathWorks, Inc., Natick, Massachusetts, US).

Prostate T_2 values

This study was approved by the Institutional Review Board. Twenty-five men (age 45 to 80) with biopsy-proven prostate cancer were studied. A study of diffusion kurtosis imaging based on this cohort has previously been published (Rosenkrantz et al. 2012). Scanning was performed on a 3T MRI scanner (Siemens Magnetom Trio, Erlangen, Germany). Each subject underwent a standard, multi parametric clinical MRI examination including multi planar T_2-weighted, diffusion-weighted and dynamic contrast-enhanced imaging. T_2 measurements were obtained with a multi echo turbo-spin echo T2-mapping sequence (TR 8000, 16 echoes at 18-msec intervals, TE 18 to 290 msec, slice thickness 5 mm, no interslice gap; field of view [FOV] 160 × 160 mm^2; matrix 128 × 129; parallel imaging factor of 2; 1 signal average). Signal measurements were made by a radiologist (A.B.R.) with 3 years of experience in prostate MRI. Regions of interest (ROIs) were placed in areas that appeared benign in all sequences. Both mono- and biexponential expressions were fitted to the data and adjusted R^2 calculated to determine whether biexponential fits were statistically justified.

Covariance Matrix Calculations

The equation describing biexponential T_2 decay is:

$$S(T_E) = S_f e^{-\frac{T_E}{T_{2f}}} + S_s e^{-\frac{T_E}{T_{2s}}} = S_0(f_f e^{-\frac{T_E}{T_{2f}}} + (1-f_f)e^{-\frac{T_E}{T_{2s}}}) \qquad (5.4)$$

where S_0 is the total signal at zero T_E; T_E is the echo-time; S_f and S_s are signal amplitudes of the fast and slow decay components, respectively; T_{2f} and T_{2s} are the T_2 values of the fast and slow decay components, respectively; and f_f is the fractional signal of the fast component, i.e., S_f / (S_f + S_s).

Each row of the matrix **A** is then:

$$\mathbf{A}_i = \frac{1}{\sigma_0}(e^{-T_{Ei}/T_{2f}} \quad T_{Ei}(\frac{1}{T_{2f}^2})S_f e^{-T_{Ei}/T_{2f}} \quad e^{-T_{Ei}/T_{2s}} \quad T_{Ei}(\frac{1}{T_{2s}^2})S_s e^{-T_{Ei}/T_{2s}}) \qquad (5.5)$$

Each row $(i = 1, 2, ..., m)$ corresponds to one of the measured signals. Total error can be minimized by choosing echo times that minimize the mean square error (MSE) given by the trace of the covariance matrix in the fits. Errors in individual parameters (T_{2f}, T_{2s}, etc.) can be minimized by choosing the echo times that minimize their corresponding CoV. Errors in f_f can be minimized by choosing echo times that minimize V_2 and V_4 (Eq. (5.3)).

Echo times that minimise errors in measurements of the normal prostate parameters were found. The number of *TE*s was between four and eight, either freely variable (i.e., separate acquisitions for each echo) or at equally spaced intervals (i.e., a standard Carr-Purcell-Meiboom-Gill (CPMG) acquisition (Meiboom and Gill 1958)). Optimum *TE*s were searched over uniform *n*-dimensional *TE* grids of 10 ms from 0 to 1000 ms.

To investigate the sensitivity of optima to the precise values of T_2 and f_f, CoVs were calculated using the optimum echo times and varying T_2s and f_f around normal values. CoVs were found with T_{2s} varied from 230 to 700 with T_{2f} and f_f normal, T_{2f} varied from 40 to 80 with T_{2s} and f_f normal and f_f varied from 0.3 to 0.9 with T_{2s} and T_{2f} normal.

Monte-Carlo Simulation

Monte Carlo simulation of noise was used to confirm the selected covariance matrix variations. Biexponential signal decays were simulated, and Gaussian noise (variance 1% of peak signal) was added. The biexponential was then fitted to the noisy signals using MATLAB's non-linear least squares curve fitting algorithm, 'lsqcurvefit'. The procedure was repeated with 100,000 different sets of noise (noise realisations) and the CoV of each parameter estimate calculated. These calculations were then repeated over the same *n*-dimensional grids of T_E values and the combination of T_E values that minimize CoV found.

5-4: Results

Prostate T_2 values

T_2 measurements were obtained in twenty-five subjects. Biexponentials were found to give statistically better fits in all but one subject (96%). This result was similar to that of (Storås et al. 2008) who found better fits in 86% of subjects. Table 5.1 gives measured values of f_f, T_{2f} and T_{2s} along with values found in two previous studies. The measured values were similar to those of (Storås et al. 2008) and somewhat different from those of (Kjaer et al. 1987). However, the latter measurements were based on twice log linear fitting method which has been replaced by non-linear least squares fitting in recent years due to its fitting inaccuracy. Based on these measurements normal and low grade tumour prostate were averaged for the optimisations: T_{2s} (prostate glandular lumen) 360 ms; T_{2f} (epithelium/stroma) 60 ms; f_f 0.58.

Table 5.1 Prostate T_2 parameters found in this and previous studies

Source	**N**	**Field**	f_f **Mean (Range)**	T_{2f} **/ ms Mean (Range)**	T_{2s} **/ ms Mean (Range)**
This thesis	22	3.0	0.58 (0.18-0.87)	60 (22-196)	360 (123-1150)
(Kjaer et al. 1987)*	5	1.5	-	86 (67-102)	111 (96-137)
(Storås et al. 2008)	16	1.5	0.7 (0.2-0.97)	64 (43-92)	546 (161-1319)

*T_2s estimated from log-linear fitting of first and last echoes.

Covariance Matrix Calculations

Tables 5.2 to 5.5 show the echo times that minimize variance in T_{2f}, T_{2s}, f_f and mean square error (MSE), respectively. Optimum echo times to measure the fast T_2 component tend to favour signal averaging at shorter echo times; conversely optima for measurement of the slow T_2 component favour signal averaging at long echo times. That is echo times that maximise dS/dT_E are favoured. Optimum echo times for measurement of f_f favour signal averaging at long and intermediate echo times. Echo times that minimize total error are distributed across the range that minimizes errors in each of the parameters separately. Overall optimum echo times are similar regardless of which parameter is measured.

Table 5.2 Echo times that minimize T_{2f} estimation errors for N (4 – 8) echo acquisitions.

N	T_{E1}	T_{E2}	T_{E3}	T_{E4}	T_{E5}	T_{E6}	T_{E7}	T_{E8}
4	0	40	210	780				
5	0	40	40	200	770			
6	0	40	40	200	200	730		
7	0	40	40	220	220	780	780	
8	0	40	40	40	210	210	780	780

Table 5.3 Echo times that minimize T_{2s} estimation errors for N (4 – 8) echo acquisitions.

N	T_{E1}	T_{E2}	T_{E3}	T_{E4}	T_{E5}	T_{E6}	T_{E7}	T_{E8}
4	0	30	160	670				
5	0	30	170	710	710			
6	0	30	180	740	740	740		
7	0	30	190	760	760	760	760	
8	0	30	190	780	780	780	780	780

Table 5.4 Echo times that minimize f_f estimation errors for N (4 – 8) echo acquisitions.

N	T_{E1}	T_{E2}	T_{E3}	T_{E4}	T_{E5}	T_{E6}	T_{E7}	T_{E8}
4	0	30	180	740				
5	0	30	190	800	800			
6	0	30	190	190	750	750		
7	0	30	200	200	780	780	780	
8	0	40	200	200	200	750	750	750

Table 5.5 Echo times that minimize mean square error (i.e., the sum of all coefficients of variation or the trace of the covariance matrix) for N (4 – 8) echo acquisitions.

N	T_{E1}	T_{E2}	T_{E3}	T_{E4}	T_{E5}	T_{E6}	T_{E7}	T_{E8}
4	0	30	170	670				
5	0	30	180	710	710			
6	0	30	190	740	740	740		
7	0	40	190	760	770	770	770	
8	0	40	190	190	720	720	720	720

Figures 5.1 to 5.3 show the changes in CoV for the four echo acquisition when one of the measured parameters (f_f, T_{2f} , T_{2s}) is varied around the normal value. CoV values are generally reasonable if these two conditions are met: First, T_{2f} and T_{2s} are significantly different. Second, none of the compartments is very small.

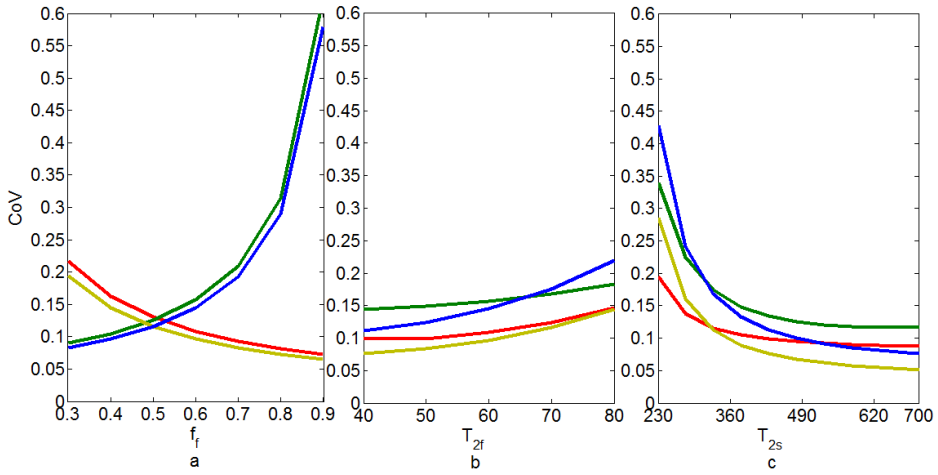

Figure 5.1 Changes in CoV for estimated biexponential parameters when the parameters are varied from the standard values used for the optimization. Echo times are 0, 40, 210 and 780 which minimize the error in estimating T_{2f}. (Table 5.2). The blue, yellow, green and red lines represent the CoV of S_s, S_f, T_{2s} and T_{2f} respectively. SNR was 100. a) T_{2s} = 360, T_{2f} =60 and f_f = 0.3-0.9. b) T_{2s} =360, T_{2f} = 40-80 and f_f =0.6. c) T_{2s} = 230-700, T_{2f} =60 and f_f = 0.6.

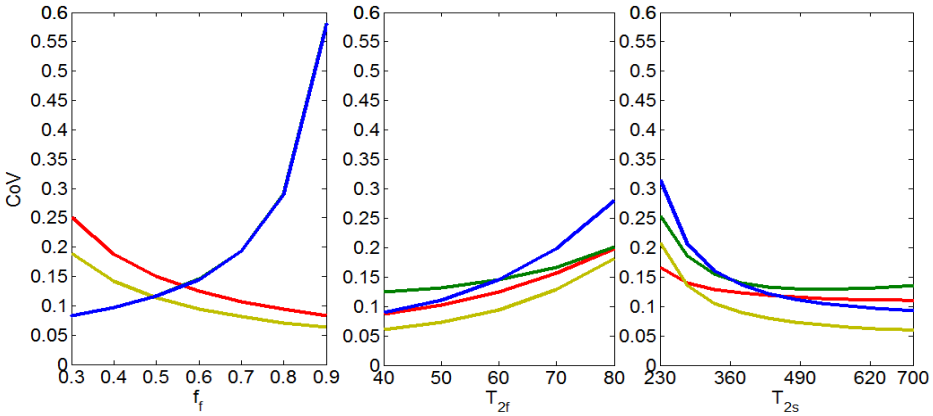

Figure 5.2 Changes in CoV for estimated biexponential parameters when the parameters are varied from the standard values used for the optimization. Echo times are 0, 30, 160 and 670 which minimize the error in estimating T_{2s} (Table 5.3). The blue, yellow, green and red lines represent the CoV of S_s, S_f, T_{2s} and T_{2f} respectively. SNR was 100. a) T_{2s} =360, T_{2f} =60 and f_f =0.3-0.9. b) T_{2s} =360, T_{2f} =40-80 and f_f =0.6. c) T_{2s} =230-700, T_{2f} =60 and f_f =0.6.(In Figure a the blue and green lines are very close to each other.)

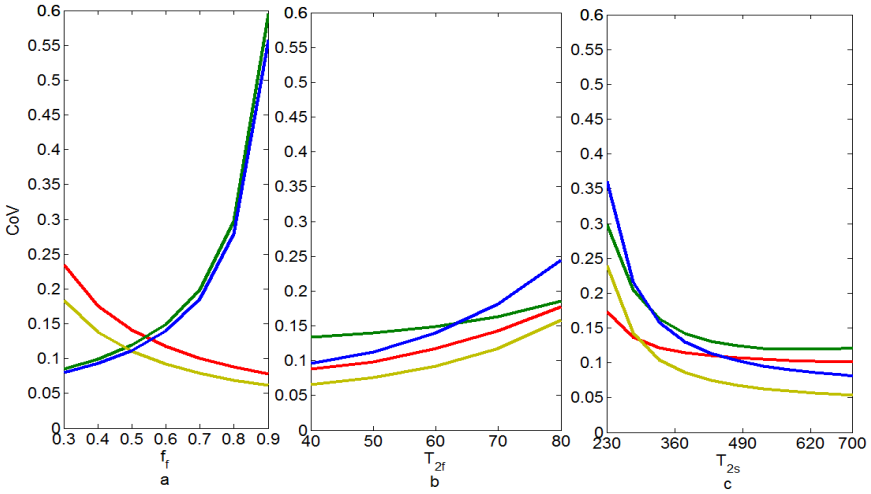

Figure 5.3 Changes in CoV for estimated biexponential parameters when the parameters are varied from the standard values used for the optimization. Echo times are 0, 30, 180 and 740 which minimize CoV of $f_f = S_f/(S_f + S_s)$ (Table 5.4). The blue, yellow, green and red lines represent the COV of S_s, S_f, T_{2s} and T_{2f} respectively. SNR was 100. a) T_{2s} =360, T_{2f} =60 and f_f =0.3-0.9. b) T_{2s} =360, T_{2f} =40-80 and f_f =0.6. c) T_{2s} =230-700, T_{2f} =60 and f_f =0.6.

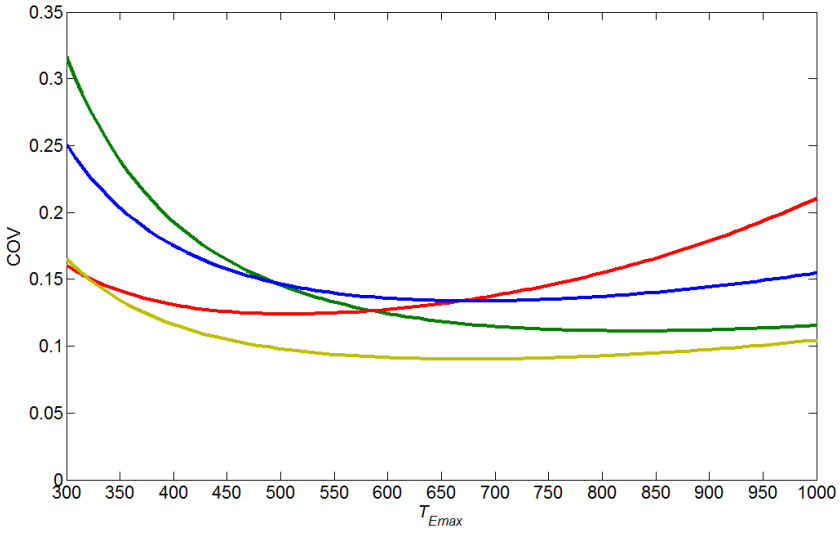

Figure 5.4 CoV of estimates of T_{2f}, T_{2f}, S_f and S_s using eight equally spaced echoes where T_{Emax} is the maximum echo time. Blue line, yellow line, green line and red line are respectively for CoV of S_s, S_f, T_{2s} and T_{2f}. SNR=100.

Monte-Carlo Confirmation

Monte-Carlo confirmations were found for normal prostate parameters and three different optima: five echoes from Table 5.2; six from Table 5.3; and eight from Table 5.4. In all cases Monte-Carlo and covariance matrix optima were identical within 10ms (i.e. the grid spacing over which the search was performed).

5-5: Discussion

The results are generally compatible with Fleysher et al.'s (Fleysher, Fleysher, and Gonen 2008) study of monoexponential decays. First, repeated signal averaging at the minimum number of echo times (two for monoexponential; four for biexponential) gives better results than measurements at multiple different echo times. Second, averaging of late, low SNR, echoes is preferable to distributing averages over all echoes equally.

SNR in these calculations was assumed to be 100. Although this is quite high for pixel based measurements it is realistic for ROI measurements

where many pixels might be averaged. Furthermore, CoV values scale as 1/SNR; as a result it is simple to calculate CoVs for any other SNR as long as noise profile could be approximated as Gaussian.

There are a number of limitations of this study. First, optimisation is not for any combination of T_2 parameters. This would require inversion of Eq. (5.1) to provide a function, f^{-1}, such that

$$y_i = f(x_i; a_1, a_2, ...a_n) \tag{5.6}$$

Considering the complexity of formulation and the multiple number of acquisitions this inversion is almost impractical.

Second, the main purpose of this chapter was to find echo times that maximize the ability to differentiate normal and cancerous tissue. These echo times will also provide nearly optimal measurements of marginally abnormal tissue but are likely to be suboptimal where T_2 parameters are very different from normal tissue. For example, echo times that minimize noise in measurements of tissues with T_2 = 100 ms will also produce good results when T_2 = 110 ms but much poorer results when T_2 = 500ms. However, since the T_2 parameter differences are also much greater this is unlikely to hinder the ability to discriminate between the two tissues. That is, if echo times that maximise the ability to identify only marginally abnormal T_2 parameters are used, grossly abnormal parameters should be relatively simple to identify. Luckily, optimising for any value of f_f between 0.3 and 0.8 was found to give identical echo times.

Third, ideally, measurements of normal prostate parameters would been acquired from healthy volunteers than prostate cancer patients. However, measurements were made in areas that appeared normal on multiparameteric MRI, which have over 90% negative prediction value for clinically significant prostate cancer (Abd-Alazeez et al. 2014; Grey et al. 2015).

Finally, it was found that the optima for protocols in which measurements at different echo times are obtained in separate acquisitions (e.g. a variety of spin echo sequences such as conventional, RARE, spin-echo EPI, etc.)

perform better that those such as CPMG, where all echoes are acquired following a single excitation. Depending on gradient strength, specific absorption rate (SAR) considerations, and the ability to deal with improperly refocused magnetization, it may be possible to decrease noise in CPMG measurements by acquisition of a large number of echoes. Also, uneven echo distributions could be used. Both these factors may increase the efficiency of CPMG sequences.

Chapter 6: Optimization of non-Gaussian DWI Acquisitions

This chapter mostly draws on material from (Gilani, Malcolm, and Johnson 2016c).

6-1: Introduction

Although the purpose of thesis was to optimize prostate MR acquisitions, the covariance matrix optimization methodology discussed in the previous chapter could be extended to non-Gaussian kurtosis model which could describe diffusion in some organs such as liver (Anderson et al. 2014), breast (Sun et al. 2015), and head and neck (Lu et al. 2012; Yuan et al. 2014).

Non-Gaussian diffusion kurtosis measurements are made by acquiring images at multiple different *b*-values and fitting the model of Eq. (3.12) to these signals with a variety of non-linear least squares algorithms. Errors in measuring both *D* and *K* will depend both on noise in the signal and in the choice of *b*-values. Previously, Fleysher et al. (Fleysher, Fleysher, and Gonen 2008) determined the acquisitions that minimized noises in mono-exponential measurements with their results being applicable to selection of echo-times in monoexponential T_2 relaxometry and selection of *b*-values in monoexponential apparent diffusion coefficient (ADC) measurements. In the previous chapter, the noise in estimation of bi-exponential T_2 measurements of the prostate cancer were minimized. In this chapter, the method is extended to optimization of mono-exponential kurtosis measurements.

6-2: Methods

All programs and numerical simulations were performed in MATLAB Release 2013b (The MathWorks, Inc., Natick, Massachusetts, US).

Covariance Matrix in General

The signal is measured for multiple *b*-values and the model is fitted using a variety of non-linear, least squares fitting methods. The co-variance matrix could be used to calculate the sensitivity of parameter estimates to each independent variable (i.e., *b*-values in here) (Huang, Feng, and Phelps 1986; Gilani et al. 2015). Here co-variance matrix calculations were used to minimize parameter errors for a mono-exponential kurtosis model.

In general a function relating a set of measured signals, y_i (i=1, 2, …, m), to a set of measurement parameters, x_i (e.g., the *b*-values) is given by

$$y_i = f(x_i; a_1, a_2, ...a_n) \tag{6.1}$$

where a_j (j=1,2,…,n) are the parameters to be estimated (e.g., *D*, *K*, etc.).

The co-variance matrix, **Q**, could be calculated in a manner similar to the previous chapter.

For diffusion weighted imaging SNR is usually defined as mean of signal divided by its standard deviation at *b*-value of 0. Each column of **A** corresponds to one of the estimated parameters and each row corresponds to a single measurement. Thus m must therefore be greater than or equal to n. **Q**, is an $n \times n$ matrix and each diagonal element, $\mathbf{Q}_{ii}$, is the variance of the corresponding parameter a_i (Huang, Feng, and Phelps 1986). The coefficient of variation (CoV_i), is therefore given by

$$CoV_i = \frac{\sqrt{\mathbf{Q}_{ii}}}{a_i} \tag{6.2}$$

The error in the i^{th} parameter may be minimized by minimizing CoV_i. Overall error is minimized by minimizing the mean square error (MSE), the trace of **Q**.

Covariance Matrix of Kurtosis Model

The mono-exponential kurtosis equation could be rewritten with a style similar to equation (6.1) as

$$S_i = f(b_i; S_0, D, K) \tag{6.3}$$

where b_i (i=1,2,…m) are the b-values, S_i(i=1,2,…m) are the measured signal at these b-values and S_0, D and K are the three parameters to be estimated. Since there are three parameters to be estimated at least three (b_i , S_i) acquisitions are needed.

The $m\times 3$ matrix **A** for equation (6.3) is:

$$\boldsymbol{A} = \frac{1}{\sigma_0}\begin{pmatrix} e^{-b_1 D+\frac{b_1^2 D^2 K}{6}} & S_0(-b_1+2\frac{b_1^2 DK}{6})e^{-b_1 D+\frac{b_1^2 D^2 K}{6}} & S_0(\frac{b_1^2 D^2}{6})e^{-b_1 D+\frac{b_1^2 D^2 K}{6}} \\ \vdots & \vdots & \vdots \\ e^{-b_m D+\frac{b_m^2 D^2 K}{6}} & S_0(-b_m+2\frac{b_m^2 DK}{6})e^{-b_m D+\frac{b_m^2 D^2 K}{6}} & S_0(\frac{b_m^2 D^2}{6})e^{-b_m D+\frac{b_m^2 D^2 K}{6}} \end{pmatrix} \tag{6.4}$$

And finally Q equals $(\mathbf{A}^T.\mathbf{A})^{-1}$. In principle it might be possible to derive **Q** analytically. However, this is not generally possible so that the calculations must be performed numerically over a discrete grid of b-values. It was possible to organize the results based on encoding parameter bD meaning that the results are not dependent on D values. For example D and K have been respectively measured to be around 0.86±0.37 $\mu m^2 ms^{-1}$ and 1.5±0.43 for head and neck tumours (Yuan et al. 2014).

The optimization can be done to minimize errors in D alone, K alone or both of these parameters. This would require minimizing the i'th corresponding diagonal element of the covariance matrix, so that the coefficient of variation in estimating that parameter ($CoV_i = \frac{\sqrt{\boldsymbol{Q}_{ii}}}{a_i}$) is minimized. If covariance matrix is derived from matrix of equation (6.4) then the second diagonal element of the covariance matrix corresponds to the variance in estimating parameter D and the third corresponds to the variance in estimating parameter K. Here to optimize both parameters K and D, the sum of CoV_2+CoV_3 was minimized.

Monte Carlo Verification

Monte Carlo simulations were used to confirm selected covariance matrix variations. Mono-exponential kurtosis models was simulated, and either Rician or Gaussian noise (standard deviation 5% of peak signal) were added separately. Obviously, for the case of Gaussian noise, at each *b*-value a random value should be drawn from a Gaussian distribution with mean of zero and standard deviation derived from S_0/SNR. However, for the case of Rician noise signal at each *b*-value is dependent on the acquired signal (Gudbjartsson and Patz 1995; Rice 1944):

$$P(S_n(b)) = \frac{S_n(b)}{\sigma^2} e^{-(S_n^2(b)+S^2(b))/2\sigma^2} I_0\left(\frac{S(b).S_n(b)}{\sigma^2}\right) \quad (6.5)$$

where $S(b)$ is the signal without noise and $S_n(b)$ is the noisy signal at each *b*-value. Accordingly, the Rician noise was constructed using MATLAB's makedist program at each *b*-value.

For both cases, after construction of noisy signal, a new mono-exponential kurtosis model was then fitted to the noisy signals using MATLAB's non-linear least squares curve fitting, lsqcurvefit. The procedure was repeated with 100,000 different sets of noise and the CoV of each parameter estimate calculated. These calculations were then repeated over the same n-dimensional grids of *b*-values and optimized *b*-values were found. 100,000 different values of *D*, *K* were stored and were used to calculate CoV_D and CoV_K.

Maximum b-Values

It is obvious that greater *b*-values tend to minimize the error in estimating kurtosis parameter because the second term in the exponential ($Kb^2D^2/6$) which contains the kurtosis parameter is multiplied by b^2.

However there are two maximum *b*-value criteria. The first maximum *b*-value limit is imposed by the scanner noise considerations. The second maximum limit is related to the fitting model. Jensen et al.(Jensen and

Helpern 2010) calculated the maximum allowable *b*-value for the mono-exponential kurtosis model to be 3/*DK*.

6-3: Results

Table 6.1 summarizes the optimization results. The optimization is based on the encoding parameter *bD*. As observed in the table, at least one maximum *b*-value is present in the optimized acquisitions.

In order to show the difference between the optimized results, the case of equally distanced b-values between 0 to maximum was also tested as shown in table 6.2. Comparing tables 6.1 and 6.2 it is clear that optimized *b*-values considerably reduce the estimation errors for *D* and *K*.

To show a more tangible presentation of the optimization results, the values of *D* and *K* were selected to be 0.86±0.37 $\mu m^2 ms^{-1}$ and 1.5±0.43 similar to values measured in head and neck tumours in (Yuan et al. 2014). The optimization was performed using these target values, and estimation errors were compared with equally-distanced acquisitions in figure 6.1 and 6.2 with varying *D* and *K*. In figures 6.1(a) and (b) *D* was assumed to be constant and *K* varied from 1 to 1.5. In figures 6.2(a) and (b) *K* was assumed to be constant and *D* varied from 0.35 to 0.85.

As observed in the four figures with increasing the number of *b*-values above 5, it is always better to optimize the acquisitions than to use equally distanced *b*-value acquisitions.

Table 6.1: Optimum b-value acquisition strategy to minimize estimation error of D and K for N(3-5) b-value acquisitions, where $(bD)_{max}$ = 3/K is the maximum allowable acquisition point, CoV_K, CoV_D and CoV_S are the coefficients of variation respectively for K, D and S0. SNR=20

N	$(bD)_1$	$(bD)_2$	$(bD)_3$	$(bD)_4$	$(bD)_5$	$(bD)_{max}$	*K*	CoV_K	CoV_D	CoV_S
3	0	0.75	2			2	1.5	0.145	0.220	0.05
3	0	0.9	3			3	1	0.153	0.188	0.05
3	0	1	3.75			3.75	0.8	0.176	0.177	0.05
3	0	1	5			5	0.6	0.245	0.168	0.05
3	0	1.05	6			6	0.5	0.335	0.164	0.05
3	0	0.9	10			10	0.3	1.48	0.173	0.05
4	0	0.8	0.8	2		2	1.5	0.145	0.171	0.05
4	0	0.95	0.95	3		3	1	0.153	0.144	0.05
4	0	1	3.75	3.75		3.75	0.8	0.126	0.176	0.05
4	0	1.05	5	5		5	0.6	0.173	0.166	0.05
4	0	1.05	6	6		6	0.5	0.237	0.163	0.05
4	0	0.95	10	10		10	0.3	1.04	0.164	0.05
5	0	0.8	0.8	2	2	2	1.5	0.108	0.168	0.05
5	0	1	1	3	3	3	1	0.118	0.142	0.05
5	0	1.05	1.05	3.75	3.75	3.75	0.8	0.122	0.133	0.05
5	0	1.1	1.1	5	5	5	0.6	0.173	0.125	0.05
5	0	1.05	6	6	6	6	0.5	0.194	0.1618	0.05
5	0	1	10	10	10	10	0.3	0.857	0.161	0.05

Table 6.2: Equally distanced b-value acquisition strategy for N(3-5) b-value acquisitions, where $(bD)_{max} = 3/K$ is the maximum allowable acquisition point, CoV_K, CoV_D and CoV_S are the coefficients of variation respectively for K, D and S0. SNR=20

N	$(bD)_1$	$(bD)_2$	$(bD)_3$	$(bD)_4$	$(bD)_5$	$(bD)_{max}$	K	CoV_K	CoV_D	CoV_S
3	0	1	2			2	1.5	0.145	0.223	0.05
3	0	1.5	3			3	1	0.15	0.22	0.05
3	0	1.88	3.75			3.75	0.8	0.18	0.24	0.05
3	0	2.5	5			5	0.6	0.24	0.29	0.05
3	0	3	6			6	0.5	0.34	0.36	0.05
3	0	5	10			10	0.3	1.48	1.13	0.05
4	0	0.66	1.33	2		2	1.5	0.14	0.19	0.05
4	0	1	2	3		3	1	0.14	0.17	0.05
4	0	1.25	2.5	3.75		3.75	0.8	0.16	0.17	0.05
4	0	1.66	3.33	5		5	0.6	0.22	0.19	0.05
4	0	2	4	6		6	0.5	0.30	0.22	0.05
4	0	3.33	6.66	10		10	0.3	1.29	0.50	0.05
5	0	0.5	1	1.5	2	2	1.5	0.13	0.18	0.05
5	0	0.75	1.5	2.25	3	3	1	0.14	0.16	0.05
5	0	0.94	1.86	2.81	3.75	3.75	0.8	0.15	0.15	0.05
5	0	1.25	2.5	3.75	5	5	0.6	0.21	0.16	0.05
5	0	1.5	3	4.5	6	6	0.5	0.28	0.17	0.05
5	0	2.5	5	7.5	10	10	0.3	1.11	0.31	0.05

(a)

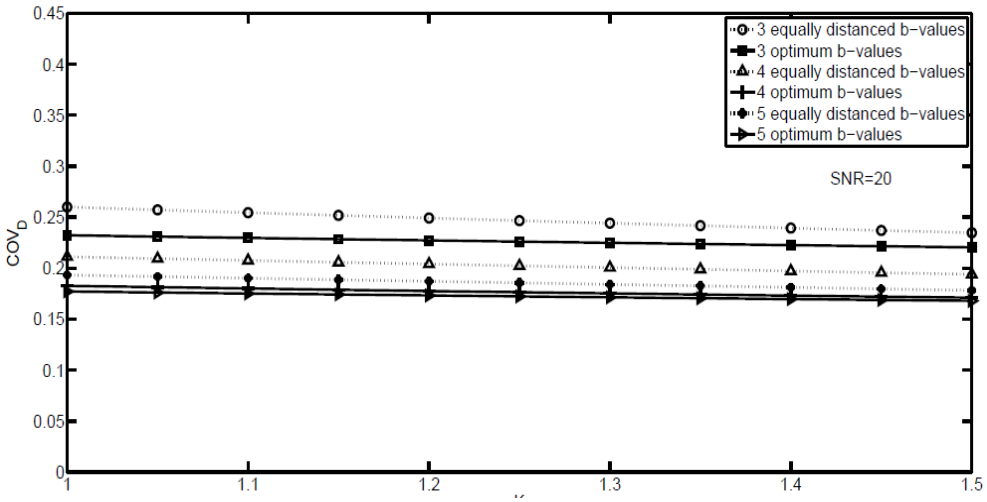

(b)

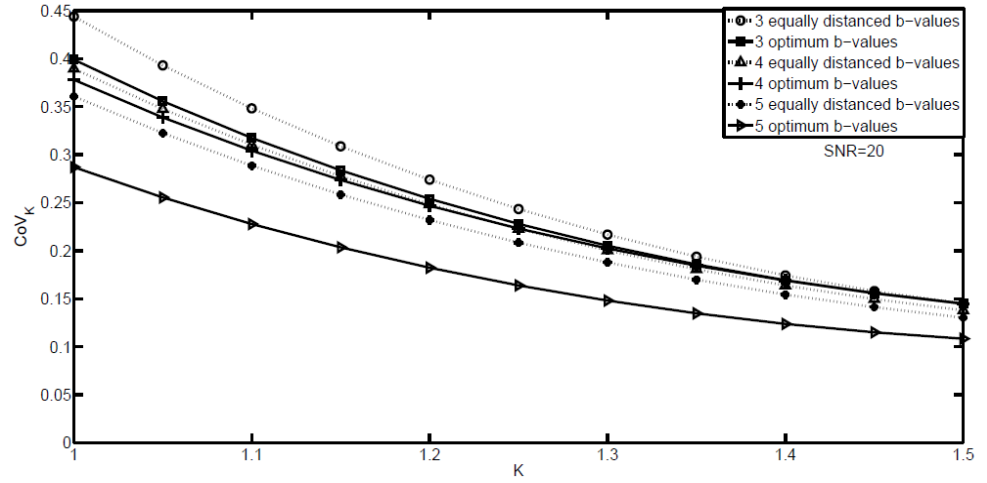

Figure 6.1: Changes in the coefficient of variation in estimating D and K (respectively CoV_D and CoV_K) with varying K for target values of head and neck tumours for 3-5 optimized or equally spaced acquisitions. (a) K varies from 1 to1.5 and CoV_D is measured. (b) K varies from 1 to1.5 and CoV_K is measured.

(a)

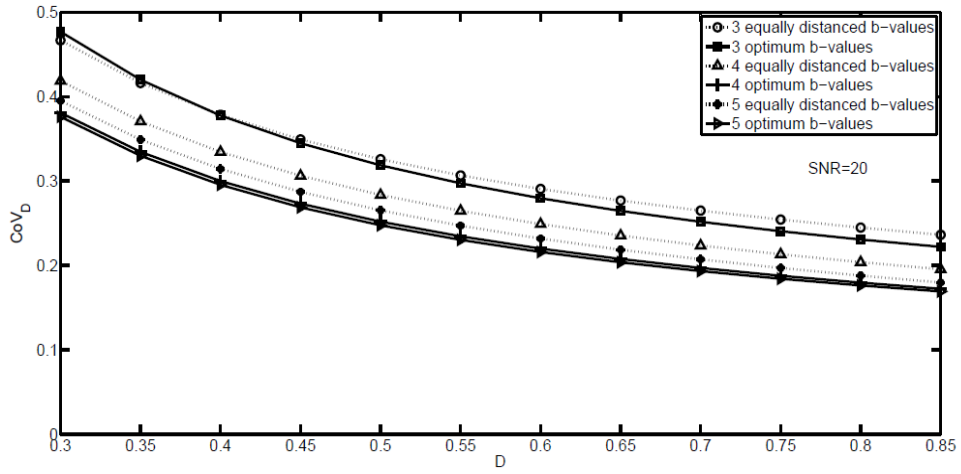

(b)

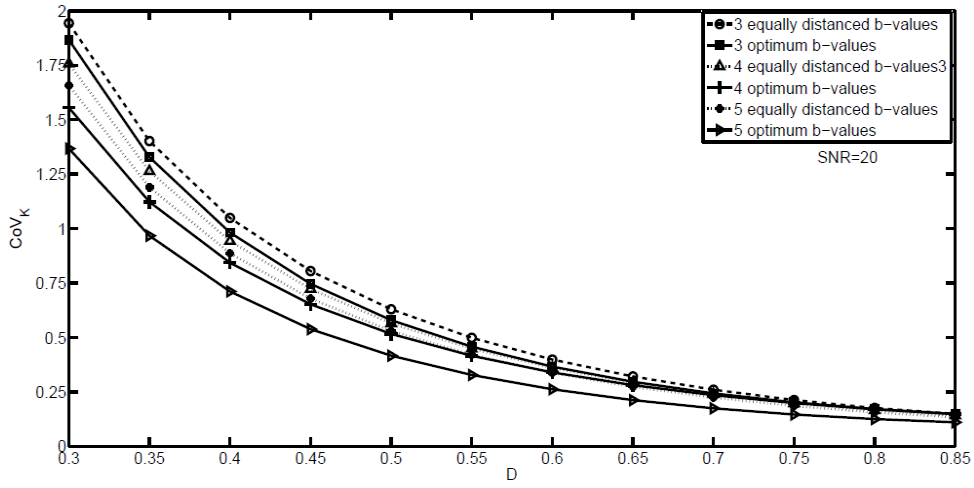

Figure 6.2: Changes in the coefficient of variation in estimating D and K (respectively CoV_D and CoV_K) with varying D for target values of head and neck tumours for 3-5 optimized or equally spaced acquisitions. (a) D varies from 0.3 to 0.85 and CoV_D is measured. (b) D varies from 0.3 to 0.85 and CoV_K is measured.

Monte Carlo Verification

This procedure was repeated for all the target values of D and K in table 6.1. CoV_D and CoV_K were found if Rician noises was present. Since here only SNR's of 20 were considered, there was a good agreement between the Rician Monte Carlo simulations of noise and the results from covariance matrix calculations.

6-4: Discussion

It was shown that as the number of *b*-value acquisitions increases, optimization significantly reduces errors in measuring both diffusion coefficient and kurtosis. Although the optimizations are dependent on both parameters D and K for the example of head and neck tumours, it was shown that the optimization works well for a wide range of variations for these parameters. However, in addition to the maximum *b*-value consideration regarding the kurtosis modelling, one should consider that if the both parameter D and K are small, then the maximum *b*-value criteria is imposed by the maximum practical *b*-values of the MR scanner. This means that since in many routine applications the maximum *b*-values that are used are smaller than the maximums of tables 6.1 or 6.2, there might be significant errors in estimating non-Gaussian parameters. For a clinical diffusion kurtosis imaging example where D is 1 $\mu m^2 ms^{-1}$ and K is 0.6, if 5 values of 0, 1000,1500, 2000 and 2500 s mm^{-2} are used, CoV_D and COV_K are respectively about 0.21 and 0.75 assuming SNR = 20.

There is an inverse relation between CoV's derived in this study and *SNR* ($CoV \propto \frac{1}{SNR}$). For example if SNR is 30 instead of 20 then CoV's derived here should be multiplied by 0.66. Parameter estimations are also dependent on diffusion echo time (T_E) or signal fading due to T_2 relaxation, similarly this can be accounted for by considering $CoV \propto \frac{1}{e^{-T_E/T_2}}$.

Optimization and noise considerations of MR relaxometry acquisitions from a statistical point of view is not something new (Tang et al. 2007; Zhang et al. 2012; Merisaari et al. 2015; Saupe et al. 2009; Jambor et al.

2014; Reiter et al. 2009). Jambor et el.(Jambor et al. 2014) have optimized biexponential diffusion measurements of the prostate. Merisaari et al.(Merisaari et al. 2015) have optimized monoexponential, biexponential and kurtosis measurements of the prostate, however only for some random selections of *b*-values instead of searching over a grid of *b*-values. In this chapter the optimization was performed for a long range of kurtosis values applicable to diffusion kurtosis of many organs and also the whole allowable grid of *b*-values was searched. Additionally, diffusion kurtosis acquisitions have already been optimised in (Poot et al. 2010) calculating Cramér–Rao lower bound. However the methodology here is more straightforward and simplified which could be routinely used.

In most of these studies the Monte Carlo method is used. The Monte Carlo method could directly assess the inherent fitting errors of any algorithm and is relatively more accurate because the simulated noise could have exact profile of the acquisitions. For example for diffusion weighted imaging for SNR's of less than five the Rician nature noise is more dominant that the Gaussian (Gudbjartsson and Patz 1995), however even in Monte Carlo optimizations of diffusion usually a Gaussian approximate of noise profile is used. This issue is not important for bigger region of interest (ROI) analysis because of significantly larger SNR's, as a result it is valid to assume the noises are Gaussian.

Also, the covariance matrix method for estimating errors is fast. For example if the number of *b*-values is greater than 10, the processing time would be around 1 or 2 hours for this method using one core of an Intel(R) Core(TM) i5-4690 CPU @ 3.50 GHz, whereas a similar Monte Carlo optimization could be significantly much more time consuming and hence is not feasible.

The results in this chapter prove that using *b*-values of as high as possible would significantly improve diffusion kurtosis imaging. However there are two constraint that impose limitations on this, first it is the interference from higher terms of diffusion and the second one is the noise limitations for the scanners at high *b*-values.

Both covariance matrix calculations and Monte Carlo assessments of noise, predict the accuracy of diffusion parameter estimations and this could be used to optimize acquisitions. These might help in near optimal selection of *b*-values if target values of diffusion parameters are known *a priori*.

Chapter 7: Discussion, Conclusions and Future Research

There is a rising interest in multi parametric MR imaging of prostate cancer. The main advantage of multi parametric MR is the integration of anatomical and functional characteristics of the tissue which results in more accurate risk stratification of the disease (Yuan et al. 2016). So far, most of the attention has gone to qualitative and semi-quantitative methods such as PIRADS (Weinreb et al. 2016) and Likert scores (Costa et al. 2016) rather than in depth quantitative methods as discussed in (Yuan et al. 2016; Shen et al. 2016). This is because quantitative methods require more complex analysis. However as shown in (Yuan et al. 2016; Shen et al. 2016), inclusion of quantitative methods in multi-parametric clinical scans further increases sensitivity and specificity of diagnosis. This is because similar to prostate biopsies, qualitative image analysis are prone to inter- and intra-observer variability, whereas this is not the case for the quantitative methods (Yuan et al. 2016).

Both quantitative diffusion and T_2 weighted methods have been included in multi-parametric studies of prostate cancer (Bratan et al. 2013; Chung et al. 2015) in addition to other modalities such as DCE. Two of the main shortcomings of the multi parametric MR protocols are the considerably longer scan times and the requirement for very advanced image post-processing methods in the clinics (Yuan et al. 2016). Hence, future studies should concentrate on further optimisation of each modality separately and also better integration of multi-parametric methods. Optimisation of the DWI protocols requires incorporation of the model introduced in chapter 4 to the image analysis. This results in additional complexities in diffusion MR analysis such as consideration of the effect of diffusion times; however this seems necessary to avoid ambiguities in interpreting diffusion parameters. In the case of T2W, although the biexponential model gives a more biophysically plausible explanation of prostate tissue, so far the concentration has been on finding faster acquisition protocols by using the monoexponential model (Dregely et al. 2016). Further application of the

biexponential model for T2W to routine scans is the subject of ongoing study, however the preliminary results confirm the reliability of this model.

In addition, quantitative MR methods could directly or indirectly correlate with many of pathological changes in prostate cancer, many of which could not be measureable from histopathology because a number of fixation effects that prevent precise extraction of biophysical parameters from biopsies. Most importantly, as discussed in chapter three, a variable shrinkage factor of 1.15 to 1.5 is considered for microscopic measurements of histologic specimens (Schned et al. 1996; Noguchi et al. 2000; Tran et al. 2015), this results in uncertainties in the ductal or tumour size measurements. As a result, quantitative (biexponential) diffusion and T_2 analysis might be able to predict some biophysical parameters as more precise alternatives to biopsies.

Here, it was shown that the signal fraction of the long T_2 component in T2W and the fast diffusion coefficient in DWI correlate with the ductal volume fractions (Gilani, Malcolm, and Johnson 2016a; Gilani et al. 2015). Also it was shown in (Gilani, Malcolm, and Johnson 2016b) that shrinkage in the size of ducts leads to decreases in the ADC of the component with faster diffusion coefficient. Such correlations might even lead to proposal of more accurate MR grading platforms.

Also, time dependency of the measured diffusion parameters is the focus of recent studies about prostate cancer. While more studies are needed to introduce time-dependent quantitative diffusion analysis, it has already been agreed on that inclusion of diffusion time related parameters (Bourne 2015) in reports is a necessity. Although, this thesis mostly concentrated on the effect of having different diffusion times on only the ductal diffusion, it is obvious that diffusion inside the cellular compartment also requires consideration of time dependency.

Chapter four of the thesis has mostly concentrated on the biophysics of diffusion than optimising the clinical acquisitions. The optimisation concept for biexponential diffusion acquisitions might be considerably different than T2W optimisation mostly because of non-Gaussian nature of

diffusion in tissue and involvement of the parameter kurtosis. A variety of biexponential fitting algorithms exist such as non-linear least squares fitting or segmented methods that are recommended to be combined for diffusion weighted imaging. Hence, optimization of prostate diffusion weighted imaging is not as easy and straightforward as the T_2 weighted imaging. Further optimisation of *b*-value acquisitions is the subject of ongoing study. Preliminary results suggest that in order to optimise the diffusion weighted signal of the prostate vs. *b*-values, four different *b*-value regions should be considered. *b*-values of 0-200 s.mm^{-2}, where the signal is mainly affected by the IVIM effect; *b*-values of 200-800 s.mm^{-2}, where the signal is mostly affected by ductal sizes; *b*-values of 700-1200 s.mm^{-2}, where the signal is shaped by the compartmental volume fraction; and finally higher *b*-values which are dependent on cellular diffusion and kurtosis. Also, care should be taken not to exceed 0-2000 *b*-value ranges because higher terms of diffusion might play a very significant role (Jensen et al. 2005; Jensen and Helpern 2010) which results in parameter estimation errors in addition to having very low SNR values in very high *b*-values. Also, the choice of fitting model (i.e. using monoexponential, kurtosis, biexponential) is highly dependent on the acquisition *b*-values used for the scan.

Additionally, the model for diffusion in the prostate does not limit the radiologists to any certain acquisition protocols; the model explicitly explains the correlations between the diffusion MR signal and biophysical changes in prostate cancer. The model parameters could be flexibly updated for different *b*-value acquisitions, diffusion times, echo times, etc. However, in order to perform biexponential analysis of diffusion, it is recommended that diffusion acquisitions are performed using at least 6 different *b*-values ranging from 0 to 1000 s.mm^{-2} instead of having limited number (i.e. less than 6) of *b*-values; additionally it is recommended to have at least four of these *b*-values are greater than 200 s.mm^{-2} to cancel out any IVIM effect.

Acquiring MRI scans prior to biopsies has already been recommended by NICE (Streeter and Brewster 2015). It is preferable if such

recommendations include clearer optimum MR acquisition guidelines. Since the topic keeps getting updated with a fast pace, it is better if such recommendations are not too detailed. However, certain concepts are recommended to be discussed explicitly such as to using a wide range of *b*-values to than limited numbers to measure diffusion related parameters *D* or *K*. Also, it is very important to distinguish between the IVIM effect and the high apparent diffusion coefficient of the ducts if biexponential are used; this requires shifting the minimum b-values to higher than 150-200 $s.mm^{-2}$.

The sensitivity and specificity of MRI of the prostate cancer is variable from study to study depending on the methodology used. While the sensitivity is around 70 - 90% or higher in most studies (Harvey et al. 2014; Mertan et al. 2016), the reported specificity values are considerably and controversially different. These high false positive rates are a result of non-cancerous lesions not being different from tumors in MR images, if the acquisitions are not biophysically optimised. While, better modellings and acquisitions similar to this thesis help in better and more quantitatively distinguish these lesions, it is advised to use guided biopsies of suspicious lesions to increase specificity (such as 82% in (Tewes et al. 2015)) of prostate cancer exams (Schoots et al. 2015; Tewes et al. 2015).

Monte Carlo random walk methods have the potential to better characterize diffusion signal for many other organs than the prostate or brain. Extension of random walk simulations to other organs requires careful consideration of a wide range of parameters such as the shape and size of the biophysical tissue, free diffusion of water in them which is dependent on the protein concentration levels, etc.

The diffusion concepts developed here such as negative kurtosis for prostate ducts and the modified two compartmental models are highly likely to be applicable to diffusion measurements of other organs such as brain. Although extension of these to pore NMR studies might not directly introduce parameters that are of interest, could help in better characterisation of time-dependent pore structures using NMR. For

example in (Luo et al. 2015) the non-Gaussian behaviour of diffusion for higher *q*-values and longer diffusion times has been modelled by considering two diffusion peaks. Whereas this could be modified by considering the maximum *q*-value limits for Gaussian estimates of diffusion similar to that of (Jensen et al. 2005) for *b*-value analysis.

The collection of histological changes with cancer measured in chapter two of this thesis, are not solely helpful for MR measurements. These measurements could also be of interest to pathologists as additional quantifications to the current Gleason grading system; hence improving the current measurements is the subject of ongoing research.

There are a number of ongoing studies related to this thesis, such as the extension of Monte Carlo simulations to study cellular tissue of prostate, optimisation of *b*-value acquisitions, and design of patient experiments for extracting more accurate values of ductal diffusion and T_2 signal fraction.

The most important limitation of this research was that no experiments were performed. The methods and models were produced or validated using either retrospective patient data as in (Gilani et al. 2015) or published literature; however, this helped in better explaining and resolving the ambiguities and contradictions in the previous studies.

References

Abd-Alazeez, Mohamed, Hashim U Ahmed, Manit Arya, Susan C Charman, Eleni Anastasiadis, Alex Freeman, Mark Emberton, and Alex Kirkham. 2014. "The accuracy of multiparametric MRI in men with negative biopsy and elevated PSA level—can it rule out clinically significant prostate cancer?" In *Urologic Oncology: Seminars and Original Investigations*, 45. e17-45. e22. Elsevier.

Allen, Derek C. 2000. *Histopathology reporting* (Springer).

Anast, J. W., G. L. Andriole, T. A. Bismar, Y. Yan, and P. A. Humphrey. 2004. 'Relating biopsy and clinical variables to radical prostatectomy findings: can insignificant and advanced prostate cancer be predicted in a screening population?', *Urology*, 64: 544-50.

Anastasiou, Anastasios, and L. D. Hall. 2004. 'Optimisation of T2 and M0 measurements of bi-exponential systems', *Magn Reson Im*, 22: 67-80.

Anderson, S. W., B. Barry, J. Soto, A. Ozonoff, M. O'Brien, and H. Jara. 2014. 'Characterizing non-gaussian, high b-value diffusion in liver fibrosis: Stretched exponential and diffusional kurtosis modeling', *J Magn Reson Imaging*, 39: 827-34.

Ansari-Rad, M, Y Abdi, and E Arzi. 2012. 'Monte Carlo random walk simulation of electron transport in dye-sensitized nanocrystalline solar cells: influence of morphology and trap distribution', *The Journal of Physical Chemistry C*, 116: 3212-18.

Anwar, S. S., Z. Anwar Khan, R. Shoaib Hamid, F. Haroon, R. Sayani, M. Beg, and Y. J. Khattak. 2014. 'Assessment of apparent diffusion coefficient values as predictor of aggressiveness in peripheral zone prostate cancer: comparison with Gleason score', *ISRN Radiol*, 2014: 263417.

Arlot, S, and A. Celisse. 2010. 'A survey of cross-validation procedures for model selection', *Stat Surveys*, 4: 40-79.

Beilin, L. J., G. J. Knight, A. D. Munro-Faure, and J. Anderson. 1966. 'The sodium, potassium, and water contents of red blood cells of healthy human adults', *J Clin Invest*, 45: 1817-25.

Benga, Gh, PW Kuchel, BE Chapman, GC Cox, I Ghiran, and CH Gallagher. 2000. 'Comparative cell shape and diffusional water permeability of red blood cells from Indian elephant (Elephas maximus) and Man (Homo sapiens)', *Comparative Haematology International*, 10: 1-8.

Bloch, Felix. 1946. 'Nuclear induction', *Physical review*, 70: 460.

Boccon-Gibod, L. M., O. Dumonceau, M. Toublanc, V. Ravery, and L. A. Boccon-Gibod. 2005. 'Micro-focal prostate cancer: a comparison of biopsy and radical prostatectomy specimen features', *Eur Urol*, 48: 895-9.

Boesen, L., E. Chabanova, V. Logager, I. Balslev, and H. S. Thomsen. 2014. 'Apparent diffusion coefficient ratio correlates significantly with prostate cancer gleason score at final pathology', *J Magn Reson Imaging*.

Bouchard, H., and A. Bielajew. 2015. 'Lorentz force correction to the Boltzmann radiation transport equation and its implications for Monte Carlo algorithms', *Phys Med Biol*, 60: 4963-71.

Bourne, R., A. Bongers, N. Charles, C. Power, P. Sved, and G. Watson. 2013. 'Effect of formalin fixation on biexponential modeling of diffusion decay in prostate tissue', *Magn Reson Med*, 70: 1160-6.

Bourne, R., N. Kurniawan, G. Cowin, P. Sved, and G. Watson. 2011. '16 T diffusion microimaging of fixed prostate tissue: preliminary findings', *Magn Reson Med*, 66: 244-7.

Bourne, R. M. 2015. 'The trouble with apparent diffusion coefficient papers', *J Med Radiat Sci*, 62: 89-91.

Bourne, R. M., N. Kurniawan, G. Cowin, T. Stait-Gardner, P. Sved, G. Watson, S. Chowdhury, and W. S. Price. 2012. 'Biexponential diffusion decay in formalin-fixed prostate tissue: preliminary findings', *Magn Reson Med*, 68: 954-9.

Bourne, R. M., N. Kurniawan, G. Cowin, T. Stait-Gardner, P. Sved, G. Watson, and W. S. Price. 2012. 'Microscopic diffusivity compartmentation in formalin-fixed prostate tissue', *Magn Reson Med*, 68: 614-20.

Bourne, Roger M., Eleftheria Panagiotaki, Andre Bongers, Paul Sved, Geoffrey Watson, and Daniel C. Alexander. 2014. 'Information theoretic ranking of four models of diffusion attenuation in fresh and fixed prostate tissue ex vivo', *Magnetic Resonance in Medicine*, 72: 1418-26.

Bratan, Flavie, Emilie Niaf, Christelle Melodelima, Anne Laure Chesnais, Rémi Souchon, Florence Mège-Lechevallier, Marc Colombel, and Olivier Rouvière. 2013. 'Influence of imaging and histological factors on prostate cancer detection and localisation on multiparametric MRI: a prospective study', *European radiology*, 23: 2019-29.

Caivano, R., P. Rabasco, A. Lotumolo, P. Cirillo, F. D'Antuono, A. Zandolino, A. Villonio, L. Macarini, M. Salvatore, and A. Cammarota. 2013. 'Comparison between Gleason score and apparent diffusion coefficient obtained from diffusion-weighted imaging of prostate cancer patients', *Cancer Invest*, 31: 625-9.

Callaghan, Paul T. 1995. 'Pulsed-gradient spin-echo NMR for planar, cylindrical, and spherical pores under conditions of wall relaxation', *Journal of Magnetic Resonance, Series A*, 113: 53-59.

Callaghan, Paul T. 1997. 'A simple matrix formalism for spin echo analysis of restricted diffusion under generalized gradient waveforms', *Journal of Magnetic Resonance*, 129: 74-84.

Chatterjee, A., G. Watson, E. Myint, P. Sved, M. McEntee, and R. Bourne. 2015. 'Changes in Epithelium, Stroma, and Lumen Space Correlate More Strongly with Gleason Pattern and Are Stronger Predictors of Prostate ADC Changes than Cellularity Metrics', *Radiology*, 277: 751-62.

Chung, Audrey G., Christian Scharfenberger, Farzad Khalvati, Alexander Wong, and Masoom A. Haider. 2015. 'Statistical Textural Distinctiveness in Multi-Parametric Prostate MRI for Suspicious Region Detection.' in Mohamed Kamel and Aurélio Campilho

(eds.), *Image Analysis and Recognition: 12th International Conference, ICIAR 2015, Niagara Falls, ON, Canada, July 22-24, 2015, Proceedings* (Springer International Publishing: Cham).

Codd, Sarah L, and Paul T Callaghan. 1999. 'Spin echo analysis of restricted diffusion under generalized gradient waveforms: planar, cylindrical, and spherical pores with wall relaxivity', *Journal of Magnetic Resonance*, 137: 358-72.

Corcoran, N. M., C. M. Hovens, M. K. H. Hong, J. Pedersen, R. G. Casey, S. Connolly, J. Peters, L. Harewood, M. E. Gleave, S. L. Goldenberg, and A. J. Costello. 2012. 'Underestimation of Gleason score at prostate biopsy reflects sampling error in lower volume tumours', *BJU International*, 109: 660-64.

Costa, D. N., Y. Lotan, N. M. Rofsky, C. Roehrborn, A. Liu, B. Hornberger, Y. Xi, F. Francis, and I. Pedrosa. 2016. 'Assessment of Prospectively Assigned Likert Scores for Targeted Magnetic Resonance Imaging-Transrectal Ultrasound Fusion Biopsies in Patients with Suspected Prostate Cancer', *J Urol*, 195: 80-7.

Davis, M. A., and A. K. Dunn. 2015. 'Dynamic light scattering Monte Carlo: a method for simulating time-varying dynamics for ordered motion in heterogeneous media', *Opt Express*, 23: 17145-55.

De Cobelli, F., S. Ravelli, A. Esposito, F. Giganti, A. Gallina, F. Montorsi, and A. Del Maschio. 2015. 'Apparent diffusion coefficient value and ratio as noninvasive potential biomarkers to predict prostate cancer grading: comparison with prostate biopsy and radical prostatectomy specimen', *AJR Am J Roentgenol*, 204: 550-7.

deSouza, N. M., S. F. Riches, N. J. Vanas, V. A. Morgan, S. A. Ashley, C. Fisher, G. S. Payne, and C. Parker. 2008. 'Diffusion-weighted magnetic resonance imaging: a potential non-invasive marker of tumour aggressiveness in localized prostate cancer', *Clin Radiol*, 63: 774-82.

Doo, K. W., D. J. Sung, B. J. Park, M. J. Kim, S. B. Cho, Y. W. Oh, Y. H. Ko, and K. S. Yang. 2012. 'Detectability of low and intermediate or high risk prostate cancer with combined T2-weighted and diffusion-weighted MRI', *Eur Radiol*, 22: 1812-9.

Döpfert, Jörg, Andreas Lemke, Anja Weidner, and Lothar R Schad. 2011. 'Investigation of prostate cancer using diffusion-weighted intravoxel incoherent motion imaging', *Magnetic resonance imaging*, 29: 1053-58.

Doyle, Scott, Michael D Feldman, Natalie Shih, John Tomaszewski, and Anant Madabhushi. 2012. 'Cascaded discrimination of normal, abnormal, and confounder classes in histopathology: Gleason grading of prostate cancer', *BMC bioinformatics*, 13: 282.

Dregely, Isabel, Daniel AJ Margolis, Kyunghyun Sung, Ziwu Zhou, Novena Rangwala, Steven S Raman, and Holden H Wu. 2016. 'Rapid quantitative T2 mapping of the prostate using three-dimensional dual echo steady state MRI at 3T', *Magnetic Resonance in Medicine*.

Dreyer, Jochen A. H., Norbert Riefler, Georg R. Pesch, Mirza Karamehmedović, Udo Fritsching, Wey Yang Teoh, and Lutz Mädler. 2014. 'Simulation of gas diffusion in highly porous

nanostructures by direct simulation Monte Carlo', *Chemical Engineering Science*, 105: 69-76.

Einstein, A. 1905. 'Über die von der molekularkinetischen Theorie der Wärme geforderte Bewegung von in ruhenden Flüssigkeiten suspendierten Teilchen [On the Motion – Required by the Molecular Kinetic Theory of Heat – of Small Particles Suspended in a Stationary Liquid]', *Annalen der physik*, 322: 549-60.

Ellingson, B. M., M. G. Malkin, S. D. Rand, J. M. Connelly, C. Quinsey, P. S. LaViolette, D. P. Bedekar, and K. M. Schmainda. 2010. 'Validation of functional diffusion maps (fDMs) as a biomarker for human glioma cellularity', *J Magn Reson Imaging*, 31: 538-48.

Epstein, J. I., L. Egevad, M. B. Amin, B. Delahunt, J. R. Srigley, P. A. Humphrey, and Committee Grading. 2016. 'The 2014 International Society of Urological Pathology (ISUP) Consensus Conference on Gleason Grading of Prostatic Carcinoma: Definition of Grading Patterns and Proposal for a New Grading System', *Am J Surg Pathol*, 40: 244-52.

Epstein, J. I., M. J. Zelefsky, D. D. Sjoberg, J. B. Nelson, L. Egevad, C. Magi-Galluzzi, A. J. Vickers, A. V. Parwani, V. E. Reuter, S. W. Fine, J. A. Eastham, P. Wiklund, M. Han, C. A. Reddy, J. P. Ciezki, T. Nyberg, and E. A. Klein. 2016. 'A Contemporary Prostate Cancer Grading System: A Validated Alternative to the Gleason Score', *Eur Urol*, 69: 428-35.

Epstein, Jonathan I, William C Allsbrook Jr, Mahul B Amin, Lars L Egevad, and ISUP Grading Committee. 2005. 'The 2005 International Society of Urological Pathology (ISUP) consensus conference on Gleason grading of prostatic carcinoma', *The American journal of surgical pathology*, 29: 1228-42.

Esen, M., M. R. Onur, N. Akpolat, I. Orhan, and E. Kocakoc. 2013. 'Utility of ADC measurement on diffusion-weighted MRI in differentiation of prostate cancer, normal prostate and prostatitis', *Quant Imaging Med Surg*, 3: 210-6.

Fain, S., M. L. Schiebler, D. G. McCormack, and G. Parraga. 2010. 'Imaging of lung function using hyperpolarized helium-3 magnetic resonance imaging: Review of current and emerging translational methods and applications', *J Magn Reson Imaging*, 32: 1398-408.

Ferlay, J., I. Soerjomataram, R. Dikshit, S. Eser, C. Mathers, M. Rebelo, D. M. Parkin, D. Forman, and F. Bray. 2015. 'Cancer incidence and mortality worldwide: sources, methods and major patterns in GLOBOCAN 2012', *Int J Cancer*, 136: E359-86.

Fick, Adolf. 1855. 'Ueber Diffusion', *Annalen der Physik und Chemie*, 170: 59-86.

Fieremans, E., J. H. Jensen, and J. A. Helpern. 2011. 'White matter characterization with diffusional kurtosis imaging', *NeuroImage*, 58: 177-88.

Fieremans, Els, Dmitry S Novikov, Jens H Jensen, and Joseph A Helpern. 2010. 'Monte Carlo study of a two-compartment exchange model of diffusion', *NMR in Biomedicine*, 23: 711-24.

Fine, S. W., and J. I. Epstein. 2008. 'A contemporary study correlating prostate needle biopsy and radical prostatectomy Gleason score', *J Urol*, 179: 1335-8; discussion 38-9.

Finkelstein, Alan. 1987. *Water movement through lipid bilayers, pores, and plasma membranes* (Wiley).

Flamm, Matthew H., Scott L. Diamond, and Talid Sinno. 2009. 'Lattice kinetic Monte Carlo simulations of convective-diffusive systems', *The Journal of chemical physics*, 130: 094904.

Fleysher, Roman, Lazar Fleysher, and Oded Gonen. 2008. 'The optimal MR acquisition strategy for exponential decay constants estimation', *Magnetic resonance imaging*, 26: 433-35.

Gallagher, Richard, Tim Appenzeller, and Dennis Normile. 1999. 'Beyond reductionism', *Science*, 284: 79.

Gibbs, P., G. P. Liney, M. D. Pickles, B. Zelhof, G. Rodrigues, and L. W. Turnbull. 2009. 'Correlation of ADC and T2 measurements with cell density in prostate cancer at 3.0 Tesla', *Invest Radiol*, 44: 572-6.

Gilani, N., P. Malcolm, and G. Johnson. 2016a. 'A model describing diffusion in prostate cancer', *Magn Reson Med*.

Gilani, N., P. Malcolm, and G. Johnson. 2016b. 'A monte carlo study of restricted diffusion: Implications for diffusion MRI of prostate cancer', *Magn Reson Med*: DOI: 10.1002/mrm.26230.

Gilani, N., A. B. Rosenkrantz, P. Malcolm, and G. Johnson. 2015. 'Minimization of errors in biexponential T2 measurements of the prostate', *J Magn Reson Imaging*, 42: 1072-7.

Gilani, Nima, Paul N. Malcolm, and Glyn Johnson. 2016c. 'Parameter Estimation Error Dependency on the Acquisition Protocol in Diffusion Kurtosis Imaging', *Applied Magnetic Resonance*.

Gleason, DF. 1977. 'Histologic grading and clinical staging of prostatic carcinoma', *Urologic pathology: the prostate*: 171-97.

Gleason, Donald F, George T Mellinger, and Veretans Administration Cooperative Urological Research Group. 2002. 'Prediction of prognosis for prostatic adenocarcinoma by combined histological grading and clinical staging', *The Journal of urology*, 167: 953-58.

Gleason, Donald F. 1992. 'The Pathobiology of Prostate Cancer-Part 1Histologic grading of prostate cancer: A perspective', *Human Pathology*, 23: 273-79.

Gorelick, Lena, Olga Veksler, Mena Gaed, Jairo Alejandro Gomez, Madeleine Moussa, Glenn Bauman, Aaron Fenster, and Aaron D Ward. 2013. 'Prostate histopathology: learning tissue component histograms for cancer detection and classification', *Medical Imaging, IEEE Transactions on*, 32: 1804-18.

Grebenkov, Denis S., Hang T. Nguyen, and Jing-Rebecca Li. 2013. 'A fast random walk algorithm for computing diffusion-weighted NMR signals in multi-scale porous media: A feasibility study for a Menger sponge', *Microporous and Mesoporous Materials*, 178: 56-59.

Grebenkov, DS, G Guillot, and B Sapoval. 2007. 'Restricted diffusion in a model acinar labyrinth by NMR: Theoretical and numerical results', *Journal of Magnetic Resonance*, 184: 143-56.

Grey, A. D., M. S. Chana, R. Popert, K. Wolfe, S. H. Liyanage, and P. L. Acher. 2015. 'Diagnostic accuracy of magnetic resonance imaging (MRI) prostate imaging reporting and data system (PI-RADS) scoring in a transperineal prostate biopsy setting', *BJU Int*, 115: 728-35.

Gudbjartsson, H., and S. Patz. 1995. 'The Rician distribution of noisy MRI data', *Magn Reson Med*, 34: 910-4.

Hahn, Erwin L. 1950. 'Spin echoes', *Physical review*, 80: 580.

Haines, TH, and LS Liebovitch. 1995. 'A molecular mechanism for the transport of water across phospholipid bilayers', *Permeability and stability of lipid bilayers. CRC Press, Boca Raton*: 123-36.

Hall, M. G., A. Bongers, P. Sved, G. Watson, and R. M. Bourne. 2015. 'Assessment of non-Gaussian diffusion with singly and doubly stretched biexponential models of diffusion-weighted MRI (DWI) signal attenuation in prostate tissue', *NMR Biomed*, 28: 486-95.

Hall, Matt G., and Daniel C. Alexander. 2009. 'Convergence and parameter choice for Monte-Carlo simulations of diffusion MRI', *Medical Imaging, IEEE Transactions on*, 28: 1354-64.

Hambrock, Thomas, Diederik M Somford, Henkjan J Huisman, Inge M van Oort, J Alfred Witjes, Christina A Hulsbergen-van de Kaa, Thomas Scheenen, and Jelle O Barentsz. 2011. 'Relationship between apparent diffusion coefficients at 3.0-T MR imaging and Gleason grade in peripheral zone prostate cancer', *Radiology*, 259: 453-61.

Harris, K. R., and L. A. Woolf. 1980. 'Pressure and Temperature-Dependence of the Self-Diffusion Coefficient of Water and O-18 Water', *Journal of the Chemical Society-Faraday Transactions I*, 76: 377-85.

Harris, Stewart. 2004. *An introduction to the theory of the Boltzmann equation* (Courier Corporation).

Harvey, CJ, J Pilcher, J Richenberg, U Patel, and F Frauscher. 2014. 'Applications of transrectal ultrasound in prostate cancer', *The British journal of radiology*.

Hayashida, Y., T. Hirai, S. Morishita, M. Kitajima, R. Murakami, Y. Korogi, K. Makino, H. Nakamura, I. Ikushima, M. Yamura, M. Kochi, J. I. Kuratsu, and Y. Yamashita. 2006. 'Diffusion-weighted imaging of metastatic brain tumors: comparison with histologic type and tumor cellularity', *AJNR Am J Neuroradiol*, 27: 1419-25.

Herbst, MARK D, and JH Goldstein. 1989. 'A review of water diffusion measurement by NMR in human red blood cells', *American Journal of Physiology-Cell Physiology*, 256: C1097-C104.

Hosseinzadeh, K., and S. D. Schwarz. 2004. 'Endorectal diffusion-weighted imaging in prostate cancer to differentiate malignant and benign peripheral zone tissue', *J Magn Reson Imaging*, 20: 654-61.

Huang, Sung-Cheng, DaGan Feng, and Michael E Phelps. 1986. 'Model dependency and estimation reliability in measurement of cerebral oxygen utilization rate with oxygen-15 and dynamic positron emission tomography', *J Cereb Blood Flow Metab*, 6: 105-19.

Ibrahiem, E. I., T. Mohsen, A. M. Nabeeh, Y. Osman, I. A. Hekal, and M. Abou El-Ghar. 2012. 'DWI-MRI: single, informative, and

noninvasive technique for prostate cancer diagnosis', *ScientificWorldJournal*, 2012: 973450.

Iima, M., K. Yano, M. Kataoka, M. Umehana, K. Murata, S. Kanao, K. Togashi, and D. Le Bihan. 2015. 'Quantitative non-Gaussian diffusion and intravoxel incoherent motion magnetic resonance imaging: differentiation of malignant and benign breast lesions', *Invest Radiol*, 50: 205-11.

Issa, B. 2002. 'In vivo measurement of the apparent diffusion coefficient in normal and malignant prostatic tissues using echo-planar imaging', *J Magn Reson Imaging*, 16: 196-200.

Jabbari, I., and S. Monadi. 2015. 'Development and validation of MCNPX-based Monte Carlo treatment plan verification system', *J Med Phys*, 40: 80-9.

Jambor, I., M. Pesola, H. Merisaari, P. Taimen, P. J. Bostrom, T. Liimatainen, and H. J. Aronen. 2016. 'Relaxation along fictitious field, diffusion-weighted imaging, and T2 mapping of prostate cancer: Prediction of cancer aggressiveness', *Magn Reson Med*, 75: 2130-40.

Jambor, Ivan, Harri Merisaari, Hannu J. Aronen, Jukka Järvinen, Jani Saunavaara, Tommi Kauko, Ronald Borra, and Marko Pesola. 2014. 'Optimization of b-value distribution for biexponential diffusion-weighted MR imaging of normal prostate', *Journal of Magnetic Resonance Imaging*, 39: 1213-22.

Jensen, J. H., J. A. Helpern, A. Ramani, H. Lu, and K. Kaczynski. 2005. 'Diffusional kurtosis imaging: the quantification of non-gaussian water diffusion by means of magnetic resonance imaging', *Magn Reson Med*, 53: 1432-40.

Jensen, Jens H., and Joseph A. Helpern. 2010. 'MRI Quantification of Non-Gaussian Water Diffusion by Kurtosis Analysis', *NMR in Biomedicine*, 23: 698-710.

Kagebayashi, Y., Y. Nakai, Y. Matsumoto, S. Samma, T. Miyasaka, and H. Nakagawa. 2012. '[Utility of diffusion-weighted magnetic resonance imaging and apparent diffusion coefficient in detection of prostate cancer and prediction of pathologic Gleason score]', *Hinyokika Kiyo*, 58: 405-8.

Kärger, J. 1985. 'NMR self-diffusion studies in heterogeneous systems', *Adv Colloid Interface Sci*, 23: 129-48.

Kärger, J, H Pfeifer, and W. Heink. 1988. 'Principles and applications of self-diffusion measurements by nuclear magnetic resonance', *Adv Magn Reson*, 12: 1-89.

Kärger, Jörg, Douglas M Ruthven, and Doros N Theodorou. 2012. *Diffusion in nanoporous materials* (John Wiley & Sons).

Kim, Eric H, Goutham Vemana, Michael H Johnson, Joel M Vetter, Adam J Rensing, Marshall C Strother, Kathryn J Fowler, and Gerald L Andriole. 2015. "Magnetic resonance imaging–targeted vs. conventional transrectal ultrasound–guided prostate biopsy: Single-institution, matched cohort comparison." In *Urologic Oncology: Seminars and Original Investigations*. Elsevier.

Kim, J. H., K. Trinkaus, A. Ozcan, M. D. Budde, and S. K. Song. 2007. 'Postmortem delay does not change regional diffusion anisotropy

characteristics in mouse spinal cord white matter', *NMR Biomed*, 20: 352-9.

Kim, T., T. Murakami, S. Takahashi, M. Hori, K. Tsuda, and H. Nakamura. 1999. 'Diffusion-weighted single-shot echoplanar MR imaging for liver disease', *AJR Am J Roentgenol*, 173: 393-8.

Kiricuta, I. C., Jr., and V. Simplaceanu. 1975. 'Tissue water content and nuclear magnetic resonance in normal and tumor tissues', *Cancer Res*, 35: 1164-7.

Kjaer, L., C. Thomsen, P. Iversen, and O. Henriksen. 1987. 'In vivo estimation of relaxation processes in benign hyperplasia and carcinoma of the prostate gland by magnetic resonance imaging', *Magn Reson Im*, 5: 23-30.

Koh, D. M., D. J. Collins, and M. R. Orton. 2011. 'Intravoxel incoherent motion in body diffusion-weighted MRI: reality and challenges', *AJR Am J Roentgenol*, 196: 1351-61.

Koh, Dow-Mu, and David J Collins. 2007. 'Diffusion-weighted MRI in the body: applications and challenges in oncology', *American Journal of Roentgenology*, 188: 1622-35.

Kozlowski, P., S. D. Chang, E. C. Jones, K. W. Berean, H. Chen, and S. L. Goldenberg. 2006. 'Combined diffusion-weighted and dynamic contrast-enhanced MRI for prostate cancer diagnosis--correlation with biopsy and histopathology', *J Magn Reson Imaging*, 24: 108-13.

Langer, Deanna L, Theodorus H van der Kwast, Andrew J Evans, Anna Plotkin, John Trachtenberg, Brian C Wilson, and Masoom A Haider. 2010. 'Prostate Tissue Composition and MR Measurements: Investigating the Relationships between ADC, T2, K trans, ve, and Corresponding Histologic Features 1', *Radiology*, 255: 485-94.

Latour, L. L., R. L. Kleinberg, P. P. Mitra, and C. H. Sotak. 1995. 'Pore-Size Distributions and Tortuosity in Heterogeneous Porous-Media', *Journal of Magnetic Resonance Series A*, 112: 83-91.

Le Bihan, Denis, Eric Breton, Denis Lallemand, ML Aubin, J Vignaud, and M Laval-Jeantet. 1988. 'Separation of diffusion and perfusion in intravoxel incoherent motion MR imaging', *Radiology*, 168: 497-505.

Le Bihan, Denis, Eric Breton, Denis Lallemand, Philippe Grenier, Emmanuel Cabanis, and Maurice Laval-Jeantet. 1986. 'MR imaging of intravoxel incoherent motions: application to diffusion and perfusion in neurologic disorders', *Radiology*, 161: 401-07.

Le Bihan, Denis, and Heidi Johansen-Berg. 2012. 'Diffusion MRI at 25: Exploring brain tissue structure and function', *NeuroImage*, 61: 324-41.

Lee, Chu-Yu, Kevin M Bennett, and Josef P Debbins. 2013. 'Sensitivities of statistical distribution model and diffusion kurtosis model in varying microstructural environments: a Monte Carlo study', *Journal of Magnetic Resonance*, 230: 19-26.

Lemberskiy, G., D S . Novikov, H. Rusinek, E. Fieremans, and A. Rosenkrantz. 2015. 'Clinical feasibility of time-dependent diffusion

MRI for improved prostate cancer grading ', *Soc. Mag. Reson. Med.*, 23: 1602.

Li, J. R., D. Calhoun, C. Poupon, and D. Le Bihan. 2014. 'Numerical simulation of diffusion MRI signals using an adaptive time-stepping method', *Phys Med Biol*, 59: 441-54.

Li, L., D. J. Margolis, M. Deng, J. Cai, L. Yuan, Z. Feng, X. Min, Z. Hu, D. Hu, J. Liu, and L. Wang. 2014. 'Correlation of gleason scores with magnetic resonance diffusion tensor imaging in peripheral zone prostate cancer', *J Magn Reson Imaging*.

Liu, D. J., A. Garcia, J. Wang, D. M. Ackerman, C. J. Wang, and J. W. Evans. 2015. 'Kinetic Monte Carlo Simulation of Statistical Mechanical Models and Coarse-Grained Mesoscale Descriptions of Catalytic Reaction-Diffusion Processes: 1D Nanoporous and 2D Surface Systems', *Chem Rev*, 115: 5979-6050.

Lori, Nicolas F., Thomas E. Conturo, and Denis Le Bihan. 2003. 'Definition of displacement probability and diffusion time in q-space magnetic resonance measurements that use finite-duration diffusion-encoding gradients', *Journal of Magnetic Resonance*, 165: 185-95.

Lu, H., J. H. Jensen, A. Ramani, and J. A. Helpern. 2006. 'Three-dimensional characterization of non-Gaussian water diffusion in humans using diffusion kurtosis imaging (DKI). ', *NMR Biomed.*, 19: 236-47.

Lu, Yonggang, Jacobus FA Jansen, Yousef Mazaheri, Hilda E Stambuk, Jason A Koutcher, and Amita Shukla-Dave. 2012. 'Extension of the intravoxel incoherent motion model to non-gaussian diffusion in head and neck cancer', *Journal of Magnetic Resonance Imaging*, 36: 1088-96.

Luczynska, E., S. Heinze-Paluchowska, A. Domalik, A. Cwierz, H. Kasperkiewicz, P. Blecharz, and B. Jereczek-Fossa. 2014. 'The Utility of Diffusion Weighted Imaging (DWI) Using Apparent Diffusion Coefficient (ADC) Values in Discriminating Between Prostate Cancer and Normal Tissue', *Pol J Radiol*, 79: 450-5.

Luo, Zhi-Xiang, Jeffrey Paulsen, M Vembusubramanian, and Yi-Qiao Song. 2015. 'Restricted diffusion effects on nuclear magnetic resonance DT 2 maps', *Geophysics*, 80: E41-E47.

Manenti, G., M. Carlani, S. Mancino, V. Colangelo, M. Di Roma, E. Squillaci, and G. Simonetti. 2007. 'Diffusion tensor magnetic resonance imaging of prostate cancer', *Invest Radiol*, 42: 412-9.

Mascali, G., and V. Romano. 2014. "A comprehensive hydrodynamical model for charge transport in graphene." In *Computational Electronics (IWCE), 2014 International Workshop on*, 1-4.

Mazaheri, Yousef, Hebert Alberto Vargas, Oguz Akin, Debra A Goldman, and Hedvig Hricak. 2012. 'Reducing the influence of b-value selection on diffusion-weighted imaging of the prostate: Evaluation of a revised monoexponential model within a clinical setting', *Journal of Magnetic Resonance Imaging*, 35: 660-68.

McNeal, John E. 1988. 'Normal histology of the prostate', *The American journal of surgical pathology*, 12: 619-33.

McRobbie, Donald W, Elizabeth A Moore, Martin J Graves, and Martin R Prince. 2007. *MRI from Picture to Proton* (Cambridge university press).

Meiboom, S., and D. Gill. 1958. 'Modified Spin-Echo Method for Measuring Nuclear Relaxation Times', *Review of Scientific Instruments*, 29: 688-91.

Merisaari, H., J. Toivonen, M. Pesola, P. Taimen, P. J. Bostrom, T. Pahikkala, H. J. Aronen, and I. Jambor. 2015. 'Diffusion-weighted imaging of prostate cancer: effect of b-value distribution on repeatability and cancer characterization', *Magn Reson Imaging*, 33: 1212-8.

Mertan, Francesca V, Matthew D Greer, Joanna H Shih, Arvin K George, Michael Kongnyuy, Akhil Muthigi, Maria J Merino, Bradford J Wood, Peter A Pinto, and Peter L Choyke. 2016. 'Prospective evaluation of the prostate imaging reporting and data system version 2 for prostate cancer detection', *The Journal of urology*.

Metens, T., D. Miranda, J. Absil, and C. Matos. 2012. 'What is the optimal b value in diffusion-weighted MR imaging to depict prostate cancer at 3T?', *Eur Radiol*, 22: 703-9.

Mills, R. 1973. 'Self-diffusion in normal and heavy water in the range 1-45. deg', *The Journal of Physical Chemistry*, 77: 685-88.

Mitchell, Donald G. 1999. *MRI principles* (WB Saunders Company).

Montironi, Rodolfo, Adhemar Longatto Filho, Alfredo Santinelli, Roberta Mazzucchelli, Roberto Pomante, Paola Colanzi, and Marina Scarpelli. 2000. 'Nuclear changes in the normal-looking columnar epithelium adjacent to and distant from prostatic intraepithelial neoplasia and prostate cancer', *Virchows Archiv*, 437: 625-34.

Mufarrij, P., A. Sankin, G. Godoy, and H. Lepor. 2010. 'Pathologic outcomes of candidates for active surveillance undergoing radical prostatectomy', *Urology*, 76: 689-92.

Mulkern, R. V., H. Gudbjartsson, C. F. Westin, H. P. Zengingonul, W. Gartner, C. R. Guttmann, R. L. Robertson, W. Kyriakos, R. Schwartz, D. Holtzman, F. A. Jolesz, and S. E. Maier. 1999. 'Multi-component apparent diffusion coefficients in human brain', *NMR Biomed*, 12: 51-62.

Mulkern, R. V., S. Vajapeyam, S. J. Haker, and S. E. Maier. 2005. 'Magnetization transfer studies of the fast and slow tissue water diffusion components in the human brain', *NMR Biomed*, 18: 186-94.

Mulkern, Robert V, Agnieszka Szot Barnes, Steven J Haker, Yin P Hung, Frank J Rybicki, Stephan E Maier, and Clare Tempany. 2006. 'Biexponential characterization of prostate tissue water diffusion decay curves over an extended b-factor range', *Magnetic resonance imaging*, 24: 563-68.

Nagarajan, R., D. Margolis, S. Raman, M. K. Sarma, K. Sheng, C. R. King, G. Verma, J. Sayre, R. E. Reiter, and M. A. Thomas. 2012. 'MR spectroscopic imaging and diffusion-weighted imaging of prostate cancer with Gleason scores', *J Magn Reson Imaging*, 36: 697-703.

Nguyen, C., A. R. Sharif-Afshar, Z. Fan, Y. Xie, S. Wilson, X. Bi, L. Payor, R. Saouaf, H. Kim, and D. Li. 2016. '3D high-resolution

diffusion-weighted MRI at 3T: Preliminary application in prostate cancer patients undergoing active surveillance protocol for low-risk prostate cancer', *Magn Reson Med*, 75: 616-26.

Niendorf, T., R. M. Dijkhuizen, D. G. Norris, M. van Lookeren Campagne, and K. Nicolay. 1996. 'Biexponential diffusion attenuation in various states of brain tissue: implications for diffusion-weighted imaging', *Magn Reson Med*, 36: 847-57.

Noguchi, Masanori, Thomas A Stamey, John E McNeal, and Cheryl EM Yemoto. 2000. 'Assessment of morphometric measurements of prostate carcinoma volume', *Cancer*, 89: 1056-64.

Novikov, Dmitry S., Els Fieremans, Jens H. Jensen, and Joseph A. Helpern. 2011. 'Random walks with barriers', *Nat Phys*, 7: 508-14.

Padhani, Anwar R, Guoying Liu, Dow Mu-Koh, Thomas L Chenevert, Harriet C Thoeny, Taro Takahara, Andrew Dzik-Jurasz, Brian D Ross, Marc Van Cauteren, and David Collins. 2009. 'Diffusion-weighted magnetic resonance imaging as a cancer biomarker: consensus and recommendations', *Neoplasia*, 11: 102-25.

Panagiotaki, E., R. W. Chan, N. Dikaios, H. U. Ahmed, J. O'Callaghan, A. Freeman, D. Atkinson, S. Punwani, D. J. Hawkes, and D. C. Alexander. 2015. 'Microstructural characterization of normal and malignant human prostate tissue with vascular, extracellular, and restricted diffusion for cytometry in tumours magnetic resonance imaging', *Invest Radiol*, 50: 218-27.

Pang, Y., B. Turkbey, M. Bernardo, J. Kruecker, S. Kadoury, M. J. Merino, B. J. Wood, P. A. Pinto, and P. L. Choyke. 2013. 'Intravoxel incoherent motion MR imaging for prostate cancer: an evaluation of perfusion fraction and diffusion coefficient derived from different b-value combinations', *Magn Reson Med*, 69: 553-62.

Papanikolaou, N., V. Maniatis, J. Pappas, A. Roussakis, R. Efthimiadou, and J. Andreou. 2002. 'Biexponential T2 relaxation time analysis of the brain: correlation with magnetization transfer ratio', *Invest Radiol*, 37: 363-7.

Pardo, Yolanda, Ferran Guedea, Ferrán Aguiló, Pablo Fernández, Víctor Macías, Alfonso Mariño, Asunción Hervás, Ismael Herruzo, María José Ortiz, and Javier Ponce de León. 2010. 'Quality-of-life impact of primary treatments for localized prostate cancer in patients without hormonal treatment', *Journal of Clinical Oncology*, 28: 4687-96.

Park, S. Y., C. K. Kim, J. J. Park, and B. K. Park. 2016. 'Exponential apparent diffusion coefficient in evaluating prostate cancer at 3 T: preliminary experience', *Br J Radiol*, 89: 20150470.

Parker, C, S Gillessen, A Heidenreich, and A Horwich. 2015. 'Cancer of the prostate: ESMO Clinical Practice Guidelines for diagnosis, treatment and follow-up', *Annals of Oncology*, 26: v69-v77.

Penrose, Roger, and Palle ET Jorgensen. 2006. 'The road to reality: A complete guide to the laws of the universe', *The Mathematical Intelligencer*, 28: 59-61.

Pentang, G., R. S. Lanzman, P. Heusch, A. Muller-Lutz, D. Blondin, G. Antoch, and H. J. Wittsack. 2014. 'Diffusion kurtosis imaging of

the human kidney: a feasibility study', *Magn Reson Imaging*, 32: 413-20.

Pesch, G. R., N. Riefler, U. Fritsching, L. C. Ciacchi, and L. Madler. 2015. 'Gas-solid catalytic reactions with an extended DSMC model', *AIChE Journal*, 61: 2092-103.

Pfeuffer, Josef, Ulrich Flögel, Wolfgang Dreher, and Dieter Leibfritz. 1998. 'Restricted diffusion and exchange of intracellular water: theoretical modelling and diffusion time dependence of 1H NMR measurements on perfused glial cells', *NMR in Biomedicine*, 11: 19-31.

Pickles, M. D., P. Gibbs, M. Sreenivas, and L. W. Turnbull. 2006. 'Diffusion-weighted imaging of normal and malignant prostate tissue at 3.0T', *J Magn Reson Imaging*, 23: 130-4.

Poot, Dirk HJ, Arnold J den Dekker, Eric Achten, Marleen Verhoye, and Jan Sijbers. 2010. 'Optimal experimental design for diffusion kurtosis imaging', *Medical Imaging, IEEE Transactions on*, 29: 819-29.

Price, William S. 2009. *NMR studies of translational motion: principles and applications* (Cambridge University Press).

Purcell, Edward Mills. 1946. 'Spontaneous emission probabilities at radio frequencies', *Physical review*, 69: 681.

Raab, P., E. Hattingen, K. Franz, F. E. Zanella, and H. Lanfermann. 2010. 'Cerebral gliomas: diffusional kurtosis imaging analysis of microstructural differences', *Radiology*, 254: 876-81.

Rasiah, Kris K., Phillip D. Stricker, Anne-Maree Haynes, Warick Delprado, Jennifer J. Turner, David Golovsky, Phillip C. Brenner, Raji Kooner, Gordon F. O'Neill, John J. Grygiel, Robert L. Sutherland, and Susan M. Henshall. 2003. 'Prognostic significance of Gleason pattern in patients with Gleason score 7 prostate carcinoma', *Cancer*, 98: 2560-65.

Reese, Adam C., Janet E. Cowan, Jonathan S. Brajtbord, Catherine R. Harris, Peter R. Carroll, and Matthew R. Cooperberg. 2012. 'The quantitative Gleason score improves prostate cancer risk assessment', *Cancer*, 118: 6046-54.

Regan, David G, and Philip W Kuchel. 2000. 'Mean residence time of molecules diffusing in a cell bounded by a semi-permeable membrane: Monte Carlo simulations and an expression relating membrane transition probability to permeability', *European Biophysics Journal*, 29: 221-27.

Regan, David G, and Philip W Kuchel. 2002. 'Simulations of molecular diffusion in lattices of cells: insights for NMR of red blood cells', *Biophysical journal*, 83: 161-71.

Regan, David G, and Philip W Kuchel. 2003. 'Simulations of NMR-detected diffusion in suspensions of red cells: the effects of variation in membrane permeability and observation time', *European Biophysics Journal*, 32: 671-75.

Reinoso, R. F., B. A. Telfer, and M. Rowland. 1997. 'Tissue water content in rats measured by desiccation', *J Pharmacol Toxicol Methods*, 38: 87-92.

Reinsberg, S. A., G. S. Payne, S. F. Riches, S. Ashley, J. M. Brewster, V. A. Morgan, and N. M. deSouza. 2007. 'Combined use of diffusion-weighted MRI and 1H MR spectroscopy to increase accuracy in prostate cancer detection', *AJR Am J Roentgenol*, 188: 91-8.

Reiter, David A., Ping-Chang Lin, Kenneth W. Fishbein, and Richard G. Spencer. 2009. 'Multicomponent T2 relaxation analysis in cartilage', *Magnetic Resonance in Medicine*, 61: 803-09.

Rice, S. O. 1944. 'Mathematical analysis of random noise', *The Bell System Technical Journal*, 23: 282-332.

Rosenkrantz, A. B., M. J. Triolo, J. Melamed, H. Rusinek, S. S. Taneja, and F. M. Deng. 2015. 'Whole-lesion apparent diffusion coefficient metrics as a marker of percentage Gleason 4 component within Gleason 7 prostate cancer at radical prostatectomy', *J Magn Reson Imaging*, 41: 708-14.

Rosenkrantz, Andrew B, Eric E Sigmund, Glyn Johnson, James S Babb, Thais C Mussi, Jonathan Melamed, Samir S Taneja, Vivian S Lee, and Jens H Jensen. 2012. 'Prostate cancer: feasibility and preliminary experience of a diffusional kurtosis model for detection and assessment of aggressiveness of peripheral zone cancer', *Radiology*, 264: 126-35.

Sabouri, S, S Chang, R Savdie, J Zhang, E Jones, L Goldenberg, and P Kozlowski. 2016. 'Luminal water imaging: a novel MRI method for prostate cancer diagnosis', *Proc. Intl. Soc. Mag. Reson. Med.*, 24: 2489.

Sabouri, S, L Fazli, S Chang, R Savdie, E Jones, L Goldenberg, and P Kozlowski. 2016. 'MR measurements of luminal water in prostate gland', 24: 2487.

Sato, C., S. Naganawa, T. Nakamura, H. Kumada, S. Miura, O. Takizawa, and T. Ishigaki. 2005. 'Differentiation of noncancerous tissue and cancer lesions by apparent diffusion coefficient values in transition and peripheral zones of the prostate', *J Magn Reson Imaging*, 21: 258-62.

Saupe, Nadja, Lawrence M. White, Jeffrey Stainsby, George Tomlinson, and Marshall S. Sussman. 2009. 'Diffusion Tensor Imaging and Fiber Tractography of Skeletal Muscle: Optimization of b Value for Imaging at 1.5 T', *American Journal of Roentgenology*, 192: W282-W90.

Sauter, G., S. Steurer, T. S. Clauditz, T. Krech, C. Wittmer, F. Lutz, M. Lennartz, T. Janssen, N. Hakimi, R. Simon, M. von Petersdorff-Campen, F. Jacobsen, K. von Loga, W. Wilczak, S. Minner, M. C. Tsourlakis, V. Chirico, A. Haese, H. Heinzer, B. Beyer, M. Graefen, U. Michl, G. Salomon, T. Steuber, L. H. Budaus, E. Hekeler, J. Malsy-Mink, S. Kutzera, C. Fraune, C. Gobel, H. Huland, and T. Schlomm. 2016. 'Clinical Utility of Quantitative Gleason Grading in Prostate Biopsies and Prostatectomy Specimens', *Eur Urol*, 69: 592-8.

Scattoni, Vincenzo, Alexandre Zlotta, Rodolfo Montironi, Claude Schulman, Patrizio Rigatti, and Francesco Montorsi. 2007. 'Extended and saturation prostatic biopsy in the diagnosis and

characterisation of prostate cancer: a critical analysis of the literature', *European urology*, 52: 1309-22.

Schlemmer, H. P., J. Merkle, R. Grobholz, T. Jaeger, M. S. Michel, A. Werner, J. Rabe, and G. van Kaick. 2004. 'Can pre-operative contrast-enhanced dynamic MR imaging for prostate cancer predict microvessel density in prostatectomy specimens?', *Eur Radiol*, 14: 309-17.

Schmainda, K. M. 2012. 'Diffusion-weighted MRI as a biomarker for treatment response in glioma', *CNS Oncol*, 1: 169-80.

Schned, Alan R, Karlya J Wheeler, Christine A Hodorowski, John A Heaney, Marc S Ernstoff, Robert J Amdur, and Robert D Harris. 1996. 'Tissue-shrinkage correction factor in the calculation of prostate cancer volume', *The American journal of surgical pathology*, 20: 1501-06.

Schneider, Caroline A, Wayne S Rasband, and Kevin W Eliceiri. 2012. 'NIH Image to ImageJ: 25 years of image analysis', *Nature methods*, 9: 671-75.

Schoots, Ivo G., Monique J. Roobol, Daan Nieboer, Chris H. Bangma, Ewout W. Steyerberg, and M. G. Myriam Hunink. 2015. 'Magnetic Resonance Imaging–targeted Biopsy May Enhance the Diagnostic Accuracy of Significant Prostate Cancer Detection Compared to Standard Transrectal Ultrasound-guided Biopsy: A Systematic Review and Meta-analysis', *European urology*, 68: 438-50.

Schröder, Fritz H, Jonas Hugosson, Monique J Roobol, Teuvo LJ Tammela, Stefano Ciatto, Vera Nelen, Maciej Kwiatkowski, Marcos Lujan, Hans Lilja, and Marco Zappa. 2012. 'Prostate-cancer mortality at 11 years of follow-up', *New England Journal of Medicine*, 366: 981-90.

Sen, P. N. 2004. 'Time-dependent diffusion coefficient as a probe of geometry', *Concepts in Magnetic Resonance Part A*, 23A: 1-21.

Shemesh, N., E. Ozarslan, P. J. Basser, and Y. Cohen. 2010. 'Detecting diffusion-diffraction patterns in size distribution phantoms using double-pulsed field gradient NMR: Theory and experiments', *Journal of Chemical Physics*, 132.

Shen, S, X Zhong, W Hsu, A Bui, H Wu, M Kuo, S Raman, D Margolis, and K Sung. 2016. 'Quantitative MRI-Driven Deep Learning for Detection of Clinical Significant Prostate Cancer', *Proc. Intl. Soc. Mag. Reson. Med.*, 24: 0584.

Shibata, Sanshiro, Nozomu Tominaga, and Masaomi Tanaka. 2014. 'Random walks and effective optical depth in relativistic flow', *The Astrophysical Journal Letters*, 787: L4.

Shier, David, Jackie Butler, and Ricki Lewis. 2006. *Hole's essentials of human anatomy and physiology* (McGraw-Hill New York).

Shinmoto, Hiroshi, Koichi Oshio, Akihiro Tanimoto, Nobuya Higuchi, Shigeo Okuda, Sachio Kuribayashi, and Robert V Mulkern. 2009. 'Biexponential apparent diffusion coefficients in prostate cancer', *Magnetic resonance imaging*, 27: 355-59.

Sigmund, EE, GY Cho, S Kim, M Finn, M Moccaldi, JH Jensen, DK Sodickson, JD Goldberg, S Formenti, and L Moy. 2011. 'Intravoxel incoherent motion imaging of tumor microenvironment in locally

advanced breast cancer', *Magnetic Resonance in Medicine*, 65: 1437-47.

Singh, Herb, Eduardo I Canto, Shahrokh F Shariat, Dov Kadmon, Brian J Miles, Thomas M Wheeler, and Kevin M Slawin. 2004. 'Improved detection of clinically significant, curable prostate cancer with systematic 12-core biopsy', *The Journal of urology*, 171: 1089-92.

Stamatakis, Michail, and Dionisios G. Vlachos. 2012. 'Unraveling the Complexity of Catalytic Reactions via Kinetic Monte Carlo Simulation: Current Status and Frontiers', *ACS Catalysis*, 2: 2648-63.

Stanisz, G. J., E. E. Odrobina, J. Pun, M. Escaravage, S. J. Graham, M. J. Bronskill, and R. M. Henkelman. 2005. 'T1, T2 relaxation and magnetization transfer in tissue at 3T', *Magn Reson Med*, 54: 507-12.

Stanisz, G. J., A. Szafer, G. A. Wright, and R. M. Henkelman. 1997. 'An analytical model of restricted diffusion in bovine optic nerve', *Magnetic Resonance in Medicine*, 37: 103-11.

Steens, S. C., F. Admiraal-Behloul, J. A. Schaap, F. G. Hoogenraad, C. A. Wheeler-Kingshott, S. le Cessie, P. S. Tofts, and M. A. van Buchem. 2004. 'Reproducibility of brain ADC histograms', *Eur Radiol*, 14: 425-30.

Stejskal, Edward O, and John E Tanner. 1965. 'Spin diffusion measurements: spin echoes in the presence of a time-dependent field gradient', *The Journal of chemical physics*, 42: 288-92.

Stenman, Ulf-Håkan, Jari Leinonen, Wan-Ming Zhang, and Patrik Finne. 1999. "Prostate-specific antigen." In *Seminars in cancer biology*, 83-93. Elsevier.

Storås, Tryggve H., Kjell-Inge Gjesdal, Øystein B. Gadmar, Jonn T. Geitung, and Nils-Einar Kløw. 2008. 'Prostate magnetic resonance imaging: Multiexponential T2 decay in prostate tissue', *Journal of Magnetic Resonance Imaging*, 28: 1166-72.

Streeter, Edward H, and Simon F Brewster. 2015. 'NICE guidelines on Prostate Cancer Active Surveillance: is UK practice leading the world?', *BJU International*, 115: 12-13.

Sukstanskii, AL, and DA Yablonskiy. 2008. 'In vivo lung morphometry with hyperpolarized 3 He diffusion MRI: theoretical background', *Journal of Magnetic Resonance*, 190: 200-10.

Sun, K., X. Chen, W. Chai, X. Fei, C. Fu, X. Yan, Y. Zhan, K. Chen, K. Shen, and F. Yan. 2015. 'Breast Cancer: Diffusion Kurtosis MR Imaging-Diagnostic Accuracy and Correlation with Clinical-Pathologic Factors', *Radiology*, 277: 46-55.

Suo, S., X. Chen, L. Wu, X. Zhang, Q. Yao, Y. Fan, H. Wang, and J. Xu. 2014. 'Non-Gaussian water diffusion kurtosis imaging of prostate cancer', *Magn Reson Imaging*, 32: 421-7.

Svolos, P., E. Kousi, E. Kapsalaki, K. Theodorou, I. Fezoulidis, C. Kappas, and I. Tsougos. 2014. 'The role of diffusion and perfusion weighted imaging in the differential diagnosis of cerebral tumors: a review and future perspectives', *Cancer Imaging*, 14: 20.

Tamada, T., T. Sone, Y. Jo, S. Toshimitsu, T. Yamashita, A. Yamamoto, D. Tanimoto, and K. Ito. 2008. 'Apparent diffusion coefficient

values in peripheral and transition zones of the prostate: comparison between normal and malignant prostatic tissues and correlation with histologic grade', *J Magn Reson Imaging*, 28: 720-6.

Tamura, C., H. Shinmoto, S. Soga, T. Okamura, H. Sato, T. Okuaki, Y. Pang, S. Kosuda, and T. Kaji. 2014. 'Diffusion kurtosis imaging study of prostate cancer: preliminary findings', *J Magn Reson Imaging*, 40: 723-9.

Tang, Guangyu, Yong Liu, Wei Li, Jiping Yao, Baoping Li, and Peng Li. 2007. 'Optimization of b value in diffusion-weighted MRI for the differential diagnosis of benign and malignant vertebral fractures', *Skeletal Radiology*, 36: 1035-41.

Tanimoto, A., J. Nakashima, H. Kohno, H. Shinmoto, and S. Kuribayashi. 2007. 'Prostate cancer screening: the clinical value of diffusion-weighted imaging and dynamic MR imaging in combination with T2-weighted imaging', *J Magn Reson Imaging*, 25: 146-52.

Tanner, John E. 1970. 'Use of the stimulated echo in NMR diffusion studies', *The Journal of chemical physics*, 52: 2523-26.

Tewes, Susanne, Katja Hueper, Dagmar Hartung, Florian Imkamp, Thomas RW Herrmann, Juergen Weidemann, Stefan Renckly, Markus A Kuczyk, Frank Wacker, and Inga Peters. 2015. 'Targeted MRI/TRUS fusion-guided biopsy in men with previous prostate biopsies using a novel registration software and multiparametric MRI PI-RADS scores: first results', *World journal of urology*, 33: 1707-14.

Theilmann, Rebecca J., Rebecca Borders, Theodore P. Trouard, Guowei Xia, Eric Outwater, James Ranger-Moore, Robert J. Gillies, and Alison Stopeck. 2004. 'Changes in Water Mobility Measured by Diffusion MRI Predict Response of Metastatic Breast Cancer to Chemotherapy', *Neoplasia*, 6: 831-37.

Thelwall, Peter E, Timothy M Shepherd, Greg J Stanisz, and Stephen J Blackband. 2006. 'Effects of temperature and aldehyde fixation on tissue water diffusion properties, studied in an erythrocyte ghost tissue model', *Magnetic Resonance in Medicine*, 56: 282-89.

Tian, Zhen, Yan Jiang Graves, Xun Jia, and Steve B Jiang. 2014. 'Automatic commissioning of a GPU-based Monte Carlo radiation dose calculation code for photon radiotherapy', *Physics in Medicine and Biology*, 59: 6467.

Tofts, Paul. 2005. *Quantitative MRI of the brain: measuring changes caused by disease* (John Wiley & Sons).

Trampel, R., J. H. Jensen, R. F. Lee, I. Kamenetskiy, G. McGuinness, and G. Johnson. 2006. 'Diffusional kurtosis imaging in the lung using hyperpolarized 3He', *Magn Reson Med*, 56: 733-7.

Tran, T., C. P. Sundaram, C. D. Bahler, J. N. Eble, D. J. Grignon, M. F. Monn, N. B. Simper, and L. Cheng. 2015. 'Correcting the Shrinkage Effects of Formalin Fixation and Tissue Processing for Renal Tumors: toward Standardization of Pathological Reporting of Tumor Size', *J Cancer*, 6: 759-66.

Turkbey, B., V. P. Shah, Y. Pang, M. Bernardo, S. Xu, J. Kruecker, J. Locklin, A. A. Baccala, Jr., A. R. Rastinehad, M. J. Merino, J. H.

Shih, B. J. Wood, P. A. Pinto, and P. L. Choyke. 2011. 'Is apparent diffusion coefficient associated with clinical risk scores for prostate cancers that are visible on 3-T MR images?', *Radiology*, 258: 488-95.

Ueda, Y., S. Takahashi, N. Ohno, K. Kyotani, H. Kawamitu, T. Miyati, N. Aoyama, Y. Ueno, K. Kitajima, F. Kawakami, T. Okuaki, R. Tsukamoto, E. Yanagita, and K. Sugimura. 2016. 'Triexponential function analysis of diffusion-weighted MRI for diagnosing prostate cancer', *J Magn Reson Imaging*, 43: 138-48.

van As, N. J., N. M. de Souza, S. F. Riches, V. A. Morgan, S. A. Sohaib, D. P. Dearnaley, and C. C. Parker. 2009. 'A study of diffusion-weighted magnetic resonance imaging in men with untreated localised prostate cancer on active surveillance', *Eur Urol*, 56: 981-7.

Vargas, H. A., O. Akin, T. Franiel, Y. Mazaheri, J. Zheng, C. Moskowitz, K. Udo, J. Eastham, and H. Hricak. 2011. 'Diffusion-weighted endorectal MR imaging at 3 T for prostate cancer: tumor detection and assessment of aggressiveness', *Radiology*, 259: 775-84.

Verma, S., A. Rajesh, H. Morales, L. Lemen, G. Bills, M. Delworth, K. Gaitonde, J. Ying, R. Samartunga, and M. Lamba. 2011. 'Assessment of aggressiveness of prostate cancer: correlation of apparent diffusion coefficient with histologic grade after radical prostatectomy', *AJR Am J Roentgenol*, 196: 374-81.

Villeirs, G. M., L. Verstraete K, W. J. De Neve, and G. O. De Meerleer. 2005. 'Magnetic resonance imaging anatomy of the prostate and periprostatic area: a guide for radiotherapists', *Radiother Oncol*, 76: 99-106.

Wang, Qing, Hai Li, Xu Yan, Chen-Jiang Wu, Xi-Sheng Liu, Hai-Bin Shi, and Yu-Dong Zhang. 2015. "Histogram analysis of diffusion kurtosis magnetic resonance imaging in differentiation of pathologic Gleason grade of prostate cancer." In *Urologic Oncology: Seminars and Original Investigations*, 337. e15-37. e24. Elsevier.

Weinreb, J. C., J. O. Barentsz, P. L. Choyke, F. Cornud, M. A. Haider, K. J. Macura, D. Margolis, M. D. Schnall, F. Shtern, C. M. Tempany, H. C. Thoeny, and S. Verma. 2016. 'PI-RADS Prostate Imaging - Reporting and Data System: 2015, Version 2', *Eur Urol*, 69: 16-40.

Westin, C. F., S. E. Maier, H. Mamata, A. Nabavi, F. A. Jolesz, and R. Kikinis. 2002. 'Processing and visualization for diffusion tensor MRI', *Medical Image Analysis*, 6: 93-108.

White, Nathan S, and Anders M Dale. 2014. 'Distinct effects of nuclear volume fraction and cell diameter on high b-value diffusion MRI contrast in tumors', *Magnetic Resonance in Medicine*, 72: 1435-43.

Woodfield, Courtney A., Glenn A. Tung, David J. Grand, John A. Pezzullo, Jason T. Machan, and Joseph F. Renzulli. 2010. 'Diffusion-Weighted MRI of Peripheral Zone Prostate Cancer: Comparison of Tumor Apparent Diffusion Coefficient With Gleason Score and Percentage of Tumor on Core Biopsy', *American Journal of Roentgenology*, 194: W316-W22.

Xing, Haoyang, Fang Lin, Qizhu Wu, and Qiyong Gong. 2013. 'Investigation of different boundary treatment methods in Monte-Carlo simulations of diffusion NMR', *Magnetic Resonance in Medicine*, 70: 1167-72.

Xu, Junqian, Peter A Humphrey, Adam S Kibel, Abraham Z Snyder, Vamsidhar R Narra, Joseph JH Ackerman, and Sheng-Kwei Song. 2009. 'Magnetic resonance diffusion characteristics of histologically defined prostate cancer in humans', *Magnetic Resonance in Medicine*, 61: 842-50.

Yoshimitsu, K., K. Kiyoshima, H. Irie, T. Tajima, Y. Asayama, M. Hirakawa, K. Ishigami, S. Naito, and H. Honda. 2008. 'Usefulness of apparent diffusion coefficient map in diagnosing prostate carcinoma: correlation with stepwise histopathology', *J Magn Reson Imaging*, 27: 132-9.

Yuan, J., D. K. Yeung, G. S. Mok, K. S. Bhatia, Y. X. Wang, A. T. Ahuja, and A. D. King. 2014. 'Non-Gaussian analysis of diffusion weighted imaging in head and neck at 3T: a pilot study in patients with nasopharyngeal carcinoma', *PloS one*, 9: e87024.

Yuan, Q., D. N. Costa, J. Senegas, Y. Xi, A. J. Wiethoff, N. M. Rofsky, C. Roehrborn, R. E. Lenkinski, and I. Pedrosa. 2016. 'Quantitative diffusion-weighted imaging and dynamic contrast-enhanced characterization of the index lesion with multiparametric MRI in prostate cancer patients', *J Magn Reson Imaging*: n/a-n/a.

Zhang, Jeff L., Eric E. Sigmund, Henry Rusinek, Hersh Chandarana, Pippa Storey, Qun Chen, and Vivian S. Lee. 2012. 'Optimization of b-value sampling for diffusion-weighted imaging of the kidney', *Magnetic Resonance in Medicine*, 67: 89-97.

Zhang, M., W. Zou, T. Chen, L. Kim, A. Khan, B. Haffty, and N. J. Yue. 2014. 'Parameterization of brachytherapy source phase space file for Monte Carlo-based clinical brachytherapy dose calculation', *Phys Med Biol*, 59: 455-64.

Zhu, Caigang, and Quan Liu. 2013. 'Review of Monte Carlo modeling of light transport in tissues', *Journal of Biomedical Optics*, 18: 050902-02.

Zubkov, Mikhail, Gary R Dennis, Tim Stait-Gardner, Allan M Torres, Scott A Willis, Gang Zheng, and William S Price. 2016. 'Physical characterization using diffusion NMR spectroscopy', *Magnetic Resonance in Chemistry*.

Zynger, Debra, and Anil Parwani. 2014. *Prostate Pathology* (Demos Medical Publishing).